Seismic acquisition analysis and design using multiple reflections

Revelo Obando, B.A.

DOI
10.4233/uuid:e5f2d517-f492-4f85-9725-72e9884549b3

Publication date
2024

Document Version
Final published version

Citation (APA)
Revelo Obando, B. A. (2024). *Seismic acquisition analysis and design using multiple reflections*. [Dissertation (TU Delft), Delft University of Technology]. https://doi.org/10.4233/uuid:e5f2d517-f492-4f85-9725-72e9884549b3

Important note
To cite this publication, please use the final published version (if applicable).
Please check the document version above.

SEISMIC ACQUISITION ANALYSIS AND DESIGN USING MULTIPLE REFLECTIONS

SEISMIC ACQUISITION ANALYSIS AND DESIGN USING MULTIPLE REFLECTIONS

Proefschrift

ter verkrijging van de graad van doctor
aan de Technische Universiteit Delft,
op gezag van de Rector Magnificus Prof.dr.ir. T.H.J.J. van der Hagen,
voorzitter van het College voor Promoties,
in het openbaar te verdedigen op
woensdag 31 januari 2024 om 10:00 uur

door

Billy Alejandro REVELO OBANDO

Master of Science in Applied Earth Sciences,
Technische Universteit Delft, Nederland,
geboren te Pasto, Colombia.

Dit proefschrift is goedgekeurd door de promotoren

Samenstelling promotiecommissie:

Rector Magnificus,	voorzitter
Dr. ir. D.J. Verschuur,	Technische Universiteit Delft, promotor
Prof. dr. ir. C.P.A. Wapenaar,	Technische Universiteit Delft, promotor
Onafhankelijke leden:	
Prof. dr. Y. Wang,	Chinese Academy of Sciences
Dr. ir. X.H. Campman,	Shell Global Solutions B.V.
Prof. dr. ir. W.A. Mulder,	Technische Universiteit Delft
Prof. dr. ir. G.J.T. Leus,	Technische Universiteit Delft
Overig lid:	
Dr. ir. G. Blacquière,	Technische Universiteit Delft

Dr. ir. G. Blacquière heeft in belangrijke mate aan de totstandkoming van het proefschrift bijgedragen.

Keywords: Seismic acquisition, Imaging, Inversion, Optimization.

Printed by: Gildeprint

Front & Back: Photo taken by the author during a seismic acquisition project.

ISBN 978-94-6384-532-8

An electronic version of this dissertation is available at
http://repository.tudelft.nl/.

To my family

CONTENTS

SUMMARY

Seismic survey design deals with determining the acquisition parameters that lead to the best possible imaging and characterization of the subsurface. The design of the survey is constrained by health, safety and environmental considerations and the available budget, seeking for a balance between quality and cost. Because seismic exploration is a widely used geophysical method for revealing underground resources, information about the subsurface is available in many areas. Therefore, it can potentially be used for purposes supplementary to exploration such as the monitoring of producing fields and fluids injection. However, the available budget for these purposes is usually lower than for exploration, and it becomes a priority to maximize the benefits derived from a potentially cheaper acquisition. In this thesis, we propose new methods for the analysis and design of seismic surveys that are based on previous knowledge from existing subsurface models and that aim to maximize image quality with the lowest acquisition efforts.

In the first part of this thesis we propose an acquisition geometry analysis method based on point-spread functions. These are computed over a grid across the subsurface model into consideration and using Full-wavefield Migration. This is an iterative least-squares inversion algorithm that makes use of multiple reflections to find a reflectivity model that explains the input data. First, we analyze the point-spread functions in the image domain and propose two quantitative measurements of resolution. These measurements are extrapolated to the complete subsurface model in order to create a map of the expected resolution after imaging. Second, we compute the wavenumber spectrum of each point-spread function that displays the illumination and detection angles at their spatial locations. Together, the resolution maps and wavenumber spectra can be used to evaluate the quality of the acquisition geometry. Because a point-spread function is the impulse response of the acquisition - preprocessing - imaging system, it is possible to analyze the effects of each one of these steps in survey quality. In our examples, we show that the point-spread functions obtained with Full-wavefield Migration have better resolution and better illumination-detection properties than those obtained with primaries-only migration. This is the result of multiple reflections illuminating areas that are not reached by primary reflections.

In the second part of this thesis we deal with survey design through two algorithms for acquisition geometry optimization. First, we propose an iterative algorithm for optimizing the receiver geometry such that it enables better imaging of the complete model under consideration. We use available seismic data to create a reference image via Full-Wavefield Migration. This image is considered the best case scenario because it is obtained with complete spatial sampling. At each iteration, we compute an objective function that compares the reference image with an image obtained from a decimated receiver geometry. We parameterize the latter through a density function that is related to the number of receivers per unit area and optimize this function through a gradient descent scheme. Through a 2D implementation of the algorithm, we show that it pro-

duces an optimized density function that gives an indication of the areas in which more receivers are necessary to obtain a better image quality. The images computed with the optimized geometry show better quality than the images obtained with a uniform receiver geometry.

In the second algorithm for survey design we focus on improving the imaging of predefined target areas through the design of target-oriented receiver geometries. The algorithm works in a similar fashion as the aforementioned method, although with a different objective function for image quality. This function is multiplied by a mask that gives more weight to the target areas of interest. The results of both 2D and 3D implementations show that the target-oriented geometries deliver a better image quality of the target zone than the images obtained with a uniform geometry. There is also a visible improvement with respect to the image obtained with the optimized geometry, i.e. with a uniform weighting mask. Additionally, we propose a procedure to compute the number of receivers that are necessary to achieve a certain imaging signal-to-noise ratio after imaging. We first compute the optimized receiver density for the subsurface model under consideration. Subsequently, we generate several acquisition geometries with different number of receivers from the same optimized density function. We compute the image corresponding to each acquisition geometry from noisy data and estimate the signal-to-noise ratio (SNR) after imaging. The necessary number of receivers can be chosen based on the target SNR after imaging.

The results presented in this thesis show the advantages that the multiple reflections provide to survey design and imaging through the use of Full-Wavefield Migration. Our analysis method shows that internal multiples may reach areas that primary reflections do not, enabling a better illumination and image resolution. For this reason, the spatial sampling requirements become less strict compared to imaging algorithms that demand uniform and denser spatial sampling. This flexibility enables the design of sparse and irregular acquisition geometries suited for a specific subsurface model, which improve image quality while keeping acquisition costs manageable.

SAMENVATTING

Het ontwerp van seismisch onderzoek richt zich op het bepalen van de acquisitieparameters die leiden tot de meest optimale beeldvorming en karakterisering van de ondergrond. Dit ontwerp wordt beïnvloed door overwegingen met betrekking tot gezondheid, veiligheid, milieu, en het beschikbare budget. Er wordt gestreefd naar een evenwicht tussen kwaliteit en kosten. Aangezien seismisch onderzoek een veelgebruikte geofysische methode is om ondergrondse hulpbronnen te onthullen, is er vaak al informatie beschikbaar over de ondergrond in veel gebieden. Hierdoor kan deze informatie potentieel worden benut voor aanvullende doeleinden, zoals het monitoren van producerende velden en het injecteren van vloeistoffen. Toch is het beschikbare budget voor deze doeleinden doorgaans lager dan voor exploratie. Het wordt daarom van essentieel belang om te streven naar de optimalisatie van de voordelen die kunnen worden behaald door middel van wellicht kostenefficiëntere acquisitie. In dit proefschrift introduceren we nieuwe methoden voor de analyse en het ontwerp van seismische onderzoeken. Deze methoden zijn gebaseerd op de bestaande kennis van ondergrondmodellen en hebben als doel de beeldkwaliteit te maximaliseren met zo min mogelijk acquisitie-inspanningen.

In het eerste gedeelte van dit proefschrift introduceren we een nieuwe methode voor de analyse van acquisitiegeometrie gebaseerd op punt-spreidingsfuncties. Deze functies worden berekend voor een raster over het betreffende ondergrondmodel, door gebruik te maken van Volledige-golfveld Migratie. Dit iteratieve kleinste-kwadraten inversiealgoritme maakt gebruik van meerdere reflecties om een reflectiviteitsmodel te ontwikkelen dat de ingevoerde gegevens verklaart. Allereerst analyseren we de punt- spreidingsfuncties in het beelddomein en introduceren we twee kwantitatieve maatstaven voor resolutie. Deze maatstaven worden vervolgens toegepast op het volledige ondergrondmodel, resulterend in een afbeelding die de verwachte resolutieverdeling na beeldvorming weergeeft. Ten tweede berekenen we het golfgetalspectrum voor elke punt- spreidingsfunctie, wat de belichtings- en detectiehoeken op hun ruimtelijke locaties weergeeft. De combinatie van resolutieverdeling en golfgetalspectra dient als een krachtig instrument om de algehele kwaliteit van de acquisitiegeometrie te beoordelen. Omdat een punt- spreidingsfunctie de impulsrespons van het acquisitie-voorverwerking- beeldvormingssysteem weergeeft, wordt het mogelijk om de effecten van elk van deze stappen op de kwaliteit van het seismische onderzoek grondig te analyseren. In onze voorbeelden benadrukken we dat punt- spreidingsfuncties verkregen via Volledige-golfveld Migratie aanzienlijk verbeterde resolutie en verbeterde belichtings-detectiekenmerken vertonen in vergelijking met die verkregen via migratie van alleen primaire reflecties. Deze verbetering is te danken aan het gebruik van meervoudige reflecties die gebieden verlichten die niet worden bereikt door primaire reflecties.

In het tweede deel van dit proefschrift behandelen we het ontwerp van de survey aan de hand van twee algoritmen om de acquisitiegeometrie te optimaliseren. Allereerst stellen we een iteratief algoritme voor om de ontvangstgeometrie te optimaliseren, met

als doel de beeldvorming van het volledige onderzochte model te verbeteren. Door gebruik te maken van beschikbare seismische gegevens creëren we een referentiebeeld via Volledige Golfveld Migratie, dat wordt beschouwd als het optimale scenario vanwege de volledige ruimtelijke bemonstering. Bij elke iteratie berekenen we een doelfunctie die het referentiebeeld vergelijkt met een beeld verkregen door gebruik te maken van een gedecimeerde ontvangstgeometrie. We parametriseren deze laatste door middel van een dichtheidsfunctie die verbonden is met het aantal ontvangers per oppervlakte-eenheid, en verfijnen deze functie met behulp van een gradiëntdaling benadering. Aan de hand van een 2D-implementatie tonen we aan dat het algoritme in staat is om een geoptimaliseerde dichtheidsfunctie te genereren, die inzichten verschaft in gebieden waar een verhoogde ontvangerdichtheid cruciaal is voor een verbeterde beeldkwaliteit. De beelden die zijn berekend met behulp van deze geoptimaliseerde geometrie vertonen een superieure kwaliteit in vergelijking met die welke verkregen worden door uniforme acquisitiegeometrieën te gebruiken.

In het tweede algoritme voor survey-ontwerp richten we ons op het verbeteren van de beeldvorming van vooraf gedefinieerde doelgebieden door het ontwerpen van doelgerichte ontvangergeometrieën. Dit algoritme volgt een vergelijkbare aanpak als de eerder genoemde methode, maar met een aangepaste doelfunctie voor beeldkwaliteit. Deze functie wordt vermenigvuldigd met een masker dat meer gewicht toekent aan de doelgebieden van bijzonder belang. Zowel de resultaten van de 2D- als de 3D-implementaties tonen aan dat de doelgerichte geometrieën een superieure beeldkwaliteit in de doelzone opleveren in vergelijking met beelden die zijn verkregen via een uniforme geometrie. Bovendien is er een duidelijke verbetering ten opzichte van de beelden die worden verkregen met de geoptimaliseerde geometrie, waarbij een uniform wegingsmasker wordt toegepast. Verder introduceren we een methode om het benodigde aantal ontvangers te bepalen om een specifieke signaal-ruisverhouding (SNR) te bereiken na de beeldvorming. In eerste instantie berekenen we de geoptimaliseerde ontvangerdichtheid voor het betreffende ondergrondmodel. Vervolgens genereren we diverse acquisitiegeometrieën met uiteenlopende aantallen ontvangers, gebaseerd op dezelfde geoptimaliseerde dichtheidsfunctie. We reconstrueren beelden voor elke opnamegeometrie met toegevoegde ruis en schatten de resulterende SNR na de beeldvorming. Het gewenste aantal ontvangers kan dan worden gekozen op basis van de beoogde SNR na beeldvorming.

De resultaten gepresenteerd in dit proefschrift illustreren de voordelen van het gebruik van meervoudige reflecties in het ontwerp van onderzoek en beeldvorming door middel van Full-Wavefield Migration. Onze analysemethode toont aan dat interne meervoudige reflecties gebieden kunnen bereiken die niet toegankelijk zijn via primaire reflecties, wat resulteert in verbeterde belichting en beeldresolutie. Hierdoor zijn de ruimtelijke bemonsteringseisen minder stringent in vergelijking met beeldvormingsalgoritmen die uniforme en dichtere ruimtelijke bemonstering vereisen. Deze flexibiliteit maakt het mogelijk om schaarse en onregelmatige acquisitiegeometrieën te ontwerpen die aangepast zijn aan specifieke ondergrondmodellen, wat de beeldkwaliteit verbetert terwijl de acquisitiekosten beheersbaar blijven.

1

INTRODUCTION

1.1. BACKGROUND

THE characterization of the subsurface at an exploration scale consists of mapping the spatial distribution and physical properties of the rocks and fluids that constitute the uppermost kilometers of the subsurface. The accurate mapping of these properties and their interpretation is essential to identify the location of rock formations of economical interest.

Reflection seismology is a type of geophysical method that uses the information contained in seismic waves to characterize the subsurface media they propagate through. In *active* surveys the seismic waves are emitted by a specific-purpose seismic source. After propagation and scattering in the subsurface, these waves return towards the Earth's surface and are recorded by seismic receivers during *data acquisition*. Subsequently, the recorded data can be processed to create maps of the Earth's elastic properties and structural images.

Seismic surveys have been widely used as the default method for the exploration of mineral resources and hydrocarbons. The latter are commonly contained within rock formations at thousands of meters of depth. As the only method capable of obtaining high-resolution images at this depth, seismic surveying has become indispensable for the exploration of these resources. Additionally, when the target of interest has been identified, seismic surveys are used for monitoring changes in the reservoir caused by the injection and extraction of fluids, such as CO_2, hydrocarbons, and water in geothermal processes. Survey optimization within this scope is of critical importance to make it suitable for energy transition because the associated budgets are lower than those for traditional exploration. In this scenario, the aim is to maximize the benefits obtained from the data with the lowest acquisition efforts.

1

1.2. SEISMIC DATA ACQUISITION

The set of spatial locations of the seismic sources and receivers and their numbers is known as the acquisition geometry. The procedure of designing an acquisition geometry is called survey design or seismic acquisition design. Seismic surveys are constrained by the available hardware and the computational power required for processing seismic data. The first seismic recording systems were limited to a few tens of recording channels, and the receivers were connected through a cable and laid out uniformly separated along a straight line. The data recorded in this way is used to create 2D images of the subsurface and this method for data collection is commonly known as *2D acquisition*. Since then, modern acquisition systems with a higher channel count emerged and enabled recording data simultaneously for several receiver lines, covering larger surface areas. The corresponding recorded data enabled the creation of 3D images of the subsurface (*3D acquisition*) (Yilmaz and Doherty, 2001). In the last two decades wireless receivers, also known as nodes, have been developed as a powerful tool that allows flexibility in the design of the receiver geometry, thus, eliminating restrictions with respect to their positioning along fixed lines. Modern surveys both with cables and seismic nodes can reach up to hundreds of thousands of active channels.

The use of specialized equipment for data acquisition and the operations required for their deployment can lead to high surveying costs. Therefore, in survey design, it is of paramount importance to find a balance between data quality and cost. Hardware utilized in seismic marine acquisition such as ocean bottom nodes, combined with multiple source vessels, can offer excellent azimuthal coverage and offset distribution compared to traditional streamer acquisition (Regone, 2007). However, the cost of each receiver point is much higher and their positioning must be optimized during the survey design. Acquisition design on land often faces limitations such as the restricted access to some areas due to the lack of permits and environmental constraints. It also needs to take into account the spatial variability of the noise introduced by inhomogeneities in the near-surface (Stork, 2019). In marine acquisition these restrictions are less frequent and the focus often lies in achieving denser spatial sampling that enables a better elimination or surface-related multiples (Lopez and Verschuur, 2015).

The operations related to data acquisition can bring health, safety and environmental (HSE) risks. For mitigating the first two, it is necessary to reduce the exposure time of the seismic crew carrying out these activities. Hence, the acquisition operations should be planned with strict timelines. The environmental risks are associated with possible perturbations of marine life due to the acquisition activities e.g., disturbance of marine mammals due to the seismic waves (Erbe, 2002). To mitigate this, tuned arrays of air guns are used as seismic sources. These are composed of multiple air guns of different volumes located following a specific spatial distribution. This configuration allows to design a far-field source signature that is limited to the frequencies of interest for exploration, i.e., without emitting unnecessary high frequencies that disturb the marine life and with minimal sound exposure levels. Additionally, the presence of marine mammal observers is usually required onboard seismic vessels in order to detect the possible presence of marine mammals in the area (Verfuss et al., 2018).

1.3. ACQUISITION GEOMETRY DESIGN

1.3.1. TRADITIONAL SURVEY DESIGN

The design of a seismic survey consists of choosing the acquisition parameters, such as the number of sources and detectors, their positions and their roll-along, that enable recording the seismic data that lead to the best possible subsurface characterization. This while fulfilling the aforementioned economical and HSE constraints.

Ideally, during data acquisition, the wavefields of interest and the background noise should be recorded unaliased, i.e., satisfying the Nyquist-Shannon criterion (Shannon, 1949). Appropriate sampling of the noise, specially of the low-velocity, low-frequency, coherent, surface-related noise, may be required so that it can be effectively removed during processing. This would require taking at least two samples per smallest wavelength. In practice, this could become prohibitively expensive as a very high number of recording channels would be needed.

In traditional acquisition designs, seismic sources and receivers are laid out along perpendicular straight lines. The space between lines and the stations within them determine the spatial sampling of the acquisition geometry. The spatial sampling is chosen to achieve certain common midpoint properties, namely trace multiplicity (bin fold) and angle coverage (Vermeer, 2012). A high bin fold, e.g., N, guarantees that the coherent reflection events of interest stack accordingly, i.e., increase by a factor N, while the non-coherent, random noise events would suffer from destructive interference, i.e., increase by a factor of only $\sqrt{N}$. This results in a signal to noise ratio (SNR) that is a factor $N/\sqrt{N} = \sqrt{N}$ higher.

The angle coverage of a point in the subsurface is determined by the angles and azimuths of the wavefields illuminating such point and that are scattered back to be detected by the receivers. A well-distributed angle coverage is important for several reasons. First, it is directly related to image resolution (Beylkin, 1985). Second, it is necessary to observe possible changes is the elastic response of the reservoir versus the incidence angle (Amplitude Versus Angle analysis or AVA) (Russell et al., 2011). This has proven to be a powerful tool for reservoir characterization.

1.3.2. BLENDED ACQUISITION

Regarding efficiency at the source side, the acquisition time and spatial coverage of the survey can be improved by activating multiple sources simultaneously at different spatial locations. Consequently, the source wavefields overlap in time and space. This is known as simultaneous source or blended acquisition (Beasley et al., 1998; Berkhout et al., 2008). For processing the resulting blended data, the wavefields must be separated through a process known as deblending before following a conventional processing approach (Hampson et al., 2008; Doulgeris et al., 2010; Wapenaar et al., 2012). The advances in deblending techniques during the last decade have enabled using several sources simultaneously without compromising the quality of the data. Additionally, sources that emit wavefields with different bandwidths can be implemented in the field. This technique is called dispersed source acquisition (DSA)(Caporal et al., 2018). Apart from a better data quality, this could result in a more efficient acquisition as low frequency sources, which require longer sweeps but less dense sampling can be optimally

positioned for achieving better full-waveform inversion results. Alternatively, instead of performing deblending followed by regular data processing, the blended data can be directly processed by the means of specialized workflows (Verschuur and Berkhout, 2011; Nakayama et al., 2019c).

1.3.3. OTHER APPROACHES

The subsurface-independent design of a seismic survey based on its CMP properties can give an indication of the expected data quality in terms of resolution and SNR. However, a complex subsurface with strong inhomogeneities causes strong scattering and ray bending. Consequently, the illumination of the zones of interest may be reduced and the resolution of the corresponding seismic images decreased.

New approaches that differ from the traditional ones in that they take the subsurface into account have been developed. In empirical methods for example, a seismic survey is numerically modeled and the modeled data are imaged. When the image is not satisfactory the acquisition geometry is adjusted manually expecting an improvement in the survey performance. Following another approach, the family of experimental design techniques aims to increase the information content of the acquired data (Maurer et al., 2010). This type of approach can be applied to problems such as full-waveform inversion (Krampe et al., 2021; Winner et al., 2023), enabling the choice of sources and receivers that offer a higher information content and potentially improving the accuracy in the velocity inversion. Other approaches for survey design make use of global optimization, specifically genetic algorithms to find the acquisition parameters that lead to better deblending and data reconstruction (Nakayama et al., 2019c; Nakayama et al., 2019b), or better reflectivity and velocity estimation (Nakayama et al., 2019a).

The family of compressive sensing (CS) (Donoho, 2006) methods use sparse data representations in a transform domain in order to reduce data dimensionality. Applied to seismic exploration, CS provides a framework for data acquisition and processing which is based in irregular sampling (Herrmann, 2010). The sparsely sampled data can subsequently be recovered with transform-based recovery methods or matrix completion algorithms (Kumar et al., 2015). The irregular sampling for a seismic survey can be further improved by optimizing the spectral gap ratio (SGP) of the acquisition mask.

1.3.4. TOWARDS TARGET-ORIENTED SURVEYS

In areas where a target of geophysical interest has been previously identified, it is desired to monitor the changes in the elastic properties of the reservoir. These changes are caused by the extraction and injection of fluids such as hydrocarbons, water and CO_2. It is also generally assumed that no changes take place in the overburden. This type of technology for monitoring is also known as *time-lapse* seismic or *4D-acquisition* (Lumley, 2001).

In 4D acquisition one or more *monitor* surveys are compared against a *baseline* survey. The processing flows for time-lapse seismic aim to extract changes in the reflection amplitudes and arrival times at the *target zone* between the baseline and monitor surveys. Traditionally, these datasets are recorded with replicated acquisition geometries and processed independently with the same strategy, in such way that the amplitude differences between images can be attributed to changes in the in-situ conditions of the

reservoir and not to different data processing flows. However, this type of approach is still prone to time-shift errors due to changes in the velocity model (Trani et al., 2011) and to possible differences in the acquisition geometry. An alternative is the simultaneous processing of these datasets through a joint-inversion process (Ayeni and Biondi, 2010). This approach uses an approximation of the Hessian at the target zone to improve its image quality. Although this joint-inversion partially mitigates the effects of non-replicated acquisition geometries, other methods for time-lapse seismic better enable the extraction of time-lapse information without having replicated geometries. Qu and Verschuur (2020) propose a method with simultaneous joint migration-inversion for time-lapse datasets, using a workflow that takes the variations in the velocity model into account to accurately extract reflectivity differences. The approach proposed by Oghenekohwo et al. (2017) allows to recover the common (unchanged) component and the differences between surveys through a sparsity-promoting recovery of data acquired with randomized subsampling. Zhang et al. (2023) take advantage of this type of reconstruction in a transform domain to design acquisition geometries that favour data recovery. Nakayama et al. (2019a) propose the simultaneous deblending and data reconstruction of data acquired in a compressed manner through a joint inversion procedure that optimizes the reconstruction of time-lapse features.

The aforementioned methods deal with the extraction of time-lapse features and the design of irregular geometries for their optimal reconstruction using approaches in the data-domain. Another family of methods exploits the fact that the spatial location of the target zone is known and proposes model-based methods for survey analysis and design focused on a single target point. The expected resolution and illumination properties at this point can be computed through the focal beam analysis method (Volker et al., 2001; van Veldhuizen et al., 2008). This method computes the resolution function and the amplitude-versus-ray (AVP) function corresponding to a particular acquisition geometry, giving an indication of its quality and deficiencies. An extension is proposed by Kumar et al. (2016a) that includes primaries and internal multiples in the analysis, therefore using the full wavefield. Wu et al. (2022) propose a method to automatically optimize the receiver or source geometry and improve the image resolution and AVP function.

1.4. DATA PROCESSING

Following acquisition, the seismic data is processed to deliver geologically interpretable products. Every processing algorithm has different data sampling requirements. Noise removal algorithms used in preprocessing for example, require dense spatial sampling in order to effectively remove complex near-surface noise in land acquisition. Traditionally, large analog geophone arrays were used to suppress this type of noise, unfortunately at the cost of some loss of signal quality. However, nowadays single-point sensors are preferred over such arrays because the signal is not affected. Moreover, the cost per receiver point is lower and multi-channel noise removal algorithms can be applied (Bakulin et al., 2018). Additionally in marine acquisition, dense spatial sampling may be required for deghosting applications (Vrolijk et al., 2017).

Due to possible HSE or logistical restrictions in the survey area, it may not be possible to deploy seismic sources and receivers in some zones, resulting in acquisition gaps.

The lack of data in these zones may hinder the reconstruction of the (near) subsurface. Therefore, it is important to consider if the subsequent data processing algorithm can effectively handle these acquisition gaps, or if additional data reconstruction algorithms are needed (Hennenfent et al., 2010; Ma, 2013; Kumar et al., 2015). In the second case, the missing reflection events, specially from near offsets, can be reconstructed through methods in a transform domain. If successful, the reconstructed data can be used directly for imaging or inversion algorithms.

The ability of an imaging algorithm to produce accurate results in the presence of acquisition gaps is limited by the numerical artifacts generated during data processing. In Marchenko methods for example (Wapenaar et al., 2021), the associated multidimensional (de)convolution operators require densely sampled data (Peng et al., 2021). However, these effects can be mitigated through an adaptation of the scheme that makes use of point-spread functions (PSFs) to deblur the resulting Green's and focusing functions (van IJsseldijk and Wapenaar, 2020). The family of least-squares reverse time-migration (LSRTM) methods are based on ray-based or finite-differences methods for numerical modeling. The former use the Born approximation and do not take the effects of the internal multiples into account (Jaramillo and Bleistein, 1999), while the latter have strict stability criteria that demand dense spatial sampling (Dai et al., 2012).

Full-wavefield migration (FWM) (Davydenko and Verschuur, 2017) is a least-squares inversion algorithm that overcomes the dense spatial sampling requirement. It is more stable for sparsely sampled data than finite-differences based algorithms because its modeling engine, Full Wavefield Modeling (FWMod), does not have to fulfil the same stability criteria (Berkhout, 2014). Moreover, FWM does not require the elimination of multiple reflections but takes them into account for imaging, possibly illuminating areas that are not reached by primaries.

1.5. OBJECTIVES

In this thesis, we propose new methods for the analysis and design of a seismic survey that take existing information of the subsurface into account. We focus on analyzing and optimizing the acquisition geometry for a particular, existing model, with the objective of maximizing image quality with the lowest possible acquisition efforts.

We build upon the work of Kumar et al. (2016b), taking advantage of the additional illumination provided by multiple reflections, and follow up the work by Wu et al. (2022), measuring and optimizing image quality at the target zone. Therefore, we combine these two objectives by measuring and optimizing image quality, at one or multiple target zones, and using the extended illumination provided by multiple reflections. The latter is possible when using FWM as high-quality imaging engine. The contributions and objectives of this thesis, are summarized in the following list:

- Analyze the outcome of a seismic survey for an existing subsurface model and a particular acquisition geometry, both for the case of using primaries only and for the case of including internal multiple reflections.

- Propose metrics for quantifying the expected resolution of a seismic image and the illumination and detection properties of a particular acquisition geometry.

- Analyze the aforementioned effects at multiple locations for the model into consideration or its entirety.
- Propose a deterministic, physics-based algorithm for acquisition geometry optimization that uses primaries and multiple reflections and enables better imaging of the model into consideration.
- Develop a method for acquisition geometry optimization for monitoring purposes, focused on one or more target zones and using sparse acquisition geometries.

1.6. OUTLINE

We dedicate Chapter 2 to acquisition geometry analysis and chapters 3 and 4 to acquisition geometry optimization. In more detail, this thesis is organized as follows:

In Chapter 2, we present an acquisition geometry analysis method based on point-spread functions. With this method we compute a set of PSFs that represent the impulse responses of the combined acquisition - preprocessing - processing system at multiple locations in the subsurface. We use FWM as imaging engine, using primaries and internal multiples for imaging. The input for this method is an existing subsurface model and the initial acquisition geometry. The deficiencies in resolution and illumination angles of the PSF give an indication of the influence of the acquisition geometry and processing algorithms on the imaging result. Finally, we compare the PSFs obtained with primaries only and using internal multiples. In the latter case, additional illumination is obtained compared to the case with primaries only, hence obtaining better image resolution.

In Chapter 3 we propose an acquisition geometry design algorithm based on FWM. The algorithm uses available subsurface information to model ideal seismic data, i.e., with spatial sampling that satisfies the Nyquist-Shannon criterion. This modeled seismic data are processed to create a reference subsurface reflectivity image that is part of an objective function for image quality. Our goal is to come as close as possible to this ideal reference reflectivity image with a cheaper acquisition geometry, i.e., with less sources and receivers. In this thesis, we limit ourselves to designing the receiver side only, assuming a fixed source distribution. We use a deterministic, gradient descent method for the optimization. The outcome of the algorithm is an optimized receiver density function that indicates the number of receivers per unit area needed for obtaining the optimum image quality. Because the algorithm iteratively updates the image with FWM, primary and internal multiples are included in the optimization process. Hence, their benefits are implicitly taken into account. The results of this Chapter are still in 2D.

In Chapter 4 we introduce a modification of the algorithm proposed in Chapter 3 that allows to design a target-oriented survey for monitoring purposes. The objective function is adjusted to give more weight to the area(s) of interest. Additionally, we analyze the effect of noise on the image quality and its impact on choosing the number of receivers. Finally, we show the results of the 3D implementation of the algorithm.

Chapter 5 discusses the conclusions drawn from this research and includes recommendations for future related works.

BIBLIOGRAPHY

[1] G. Ayeni and B. Biondi. "Target-oriented joint least-squares migration/inversion of time-lapse seismic data sets". *Geophysics* 75 (2010), R61–R73.

[2] A. Bakulin, I. Silvestrov, M. Dmitriev, D. Neklyudov, M. Protasov, K. Gadylshin, V. Tcheverda, and V. Dolgov. "Nonlinear beamforming for enhancing prestack seismic data with a challenging near surface or overburden". *First Break* 36 (2018), pp. 121–126.

[3] C. J. Beasley, R. E. Chambers, and Z. Jiang. "A new look at simultaneous sources". *SEG Technical Program Expanded Abstracts 1998*. 1998.

[4] A. J. Berkhout, G. Blacquière, and E. Verschuur. "From simultaneous shooting to blended acquisition". *SEG Technical Program Expanded Abstracts 2008*. 2008.

[5] A. Berkhout. "Review Paper: An outlook on the future of seismic imaging, Part II: Full-Wavefield Migration". *Geophysical Prospecting* 62 (2014), pp. 931–949.

[6] G. Beylkin. "Imaging of discontinuities in the inverse scattering problem by inversion of a causal generalized Radon transform". *Journal of Mathematical Physics* 26 (1985), pp. 99–108.

[7] M. Caporal, G. Blacquière, and M. Davydenko. "Broadband imaging via direct inversion of blended dispersed source array data: Broadband imaging via direct inversion". *Geophysical Prospecting* 66 (2018), pp. 942–953.

[8] W. Dai, P. Fowler, and G. T. Schuster. "Multi-source least-squares reverse time migration: Multisource LSRTM". *Geophysical Prospecting* 60 (2012), pp. 681–695.

[9] M. Davydenko and D. Verschuur. "Full-wavefield migration: using surface and internal multiples in imaging: Full wavefield migration". *Geophysical Prospecting* 65 (2017), pp. 7–21.

[10] D. Donoho. "Compressed sensing". *IEEE Transactions on Information Theory* 52 (2006), pp. 1289–1306.

[11] P. Doulgeris, A. Mahdad, and G. Blacquière. "Separation of blended data by iterative estimation and subtraction of interference noise". *SEG Technical Program Expanded Abstracts* 29 (2010), pp. 3514–3518.

[12] C. Erbe. "Underwater noise of whale-watching boats and potential effects on killer whales (orcinus orca), based on an acoustic impact model". *Marine Mammal Science* 18 (2002), pp. 394–418.

[13] G. Hampson, J. Stefani, and F. Herkenhoff. "Acquisition using simultaneous sources". *The Leading Edge* 27 (2008), pp. 918–923.

[14] G. Hennenfent, L. Fenelon, and F. J. Herrmann. “Nonequispaced curvelet transform for seismic data reconstruction: A sparsity-promoting approach”. *Geophysics* 75 (2010), WB203–WB210.

[15] F. J. Herrmann. “Randomized sampling and sparsity: Getting more information from fewer samples”. *Geophysics* 75 (2010), WB173–WB187.

[16] H. H. Jaramillo and N. Bleistein. “The link of Kirchhoff migration and demigration to Kirchhoff and Born modeling”. *Geophysics* 64 (1999), pp. 1793–1805.

[17] V. Krampe, P. Edme, and H. Maurer. “Optimized experimental design for seismic full waveform inversion: A computationally efficient method including a flexible implementation of acquisition costs”. *Geophysical Prospecting* 69 (2021), pp. 152–166.

[18] A. Kumar, G. Blacquière, M. W. Pedersen, and A. Goertz. “Full-wavefield marine survey design using all multiples”. *Geophysics* 81 (2016), P1–P12.

[19] A. Kumar, G. Blacquière, and E. Verschuur. “Extending illumination using all multiples: application to 3D acquisition geometry analysis: Extending illumination using multiples”. *Geophysical Prospecting* 64 (2016), pp. 622–641.

[20] R. Kumar, C. Da Silva, O. Akalin, A. Y. Aravkin, H. Mansour, B. Recht, and F. J. Herrmann. “Efficient matrix completion for seismic data reconstruction”. *Geophysics* 80 (2015), pp. V97–V114.

[21] G. A. Lopez and D. J. Verschuur. “Closed-loop surface-related multiple elimination and its application to simultaneous data reconstruction”. *Geophysics* 80 (2015), pp. V189–V199.

[22] D. E. Lumley. “Time-lapse seismic reservoir monitoring”. *Geophysics* 66 (2001), pp. 50–53.

[23] J. Ma. “Three-dimensional irregular seismic data reconstruction via low-rank matrix completion”. *Geophysics* 78 (2013), pp. V181–V192.

[24] H. Maurer, A. Curtis, and D. E. Boerner. “Recent advances in optimized geophysical survey design”. *Geophysics* 75 (2010), 75A177–75A194.

[25] S. Nakayama, G. Blacquière, and T. Ishiyama. “Acquisition design for direct reflectivity and velocity estimation from blended and irregularly sampled data”. *Geophysical Prospecting* 67 (2019), pp. 2127–2146.

[26] S. Nakayama, G. Blacquière, and T. Ishiyama. “Automated survey design for blended acquisition with irregular spatial sampling via the integration of a metaheuristic and deep learning”. *Geophysics* 84 (2019), P47–P60.

[27] S. Nakayama, G. Blacquière, T. Ishiyama, and S. Ishikawa. “Blended-acquisition design of irregular geometries towards faster, cheaper, safer and better seismic surveying”. *Geophysical Prospecting* 67 (2019), pp. 1498–1521.

[28] F. Oghenekohwo, H. Wason, E. Esser, and F. J. Herrmann. “Low-cost time-lapse seismic with distributed compressive sensing — Part 1: Exploiting common information among the vintages”. *Geophysics* 82 (2017), P1–P13.

[29] H. Peng, I. Vasconcelos, Y. Sripanich, and L. Zhang. "An analysis of acquisition-related subsampling effects on Marchenko focusing, redatuming, and primary estimation". *Geophysics* 86 (2021), WC75–WC88.

[30] S. Qu and D. J. Verschuur. "Simultaneous joint migration inversion for high-resolution imaging/inversion of time-lapse seismic datasets". *Geophysical Prospecting* 68 (2020), pp. 1167–1188.

[31] C. J. Regone. "Using 3D finite-difference modeling to design wide-azimuth surveys for improved subsalt imaging". *Geophysics* 72 (2007), SM231–SM239.

[32] B. H. Russell, D. Gray, and D. P. Hampson. "Linearized AVO and poroelasticity". *Geophysics* 76 (2011), pp. C19–C29.

[33] C. Shannon. "Communication in the Presence of Noise". *Proceedings of the IRE* 37 (1949), pp. 10–21.

[34] C. Stork. "Global land seismic acquisition optimization by accounting for varying noise, obstacles, non-uniform placement costs, and signal". *SEG Technical Program Expanded Abstracts 2019*. 2019.

[35] M. Trani, R. Arts, O. Leeuwenburgh, and J. Brouwer. "Estimation of changes in saturation and pressure from 4D seismic AVO and time-shift analysis". *Geophysics* 76 (2011), pp. C1–C17.

[36] J. van IJsseldijk and K. Wapenaar. "Adaptation of the iterative Marchenko scheme for imperfectly sampled data". *Geophysical Journal International* 224 (2020), pp. 326–336.

[37] E. J. van Veldhuizen, G Blacquière, and A. J. Berkhout. "Acquisition geometry analysis in complex 3D media". *Geophysics* 73 (2008), Q43–Q58.

[38] U. K. Verfuss et al. "Comparing methods suitable for monitoring marine mammals in low visibility conditions during seismic surveys". *Marine Pollution Bulletin* 126 (2018), pp. 1–18.

[39] G. J. O. Vermeer. *3D Seismic Survey Design*. 2nd ed. Geophysical References Series. Society of Exploration Geophysicists, 2012.

[40] D. J. Verschuur and A. J. Berkhout. "Seismic migration of blended shot records with surface-related multiple scattering". *Geophysics* 76 (2011), A7–A13.

[41] A. W. F. Volker, G. Blacquière, A. J. Berkhout, and L. Ongkiehong. "Comprehensive assessment of seismic acquisition geometries by focal beams—Part II: Practical aspects and examples". *Geophysics* 66 (2001), pp. 918–931.

[42] J.-W. Vrolijk, E. Verschuur, and G. Lopez. "Integrated receiver deghosting and closed-loop surface-multiple elimination". *Geophysics* 82 (2017), T133–T141.

[43] K. Wapenaar, J. Van Der Neut, and J. Thorbecke. "Deblending by direct inversion". *Geophysics* 77 (2012), A9–A12.

[44] K. Wapenaar et al. "Marchenko redatuming, imaging, and multiple elimination and their mutual relations". *Geophysics* 86 (2021), WC117–WC140.

[45] V. Winner, P. Edme, and H. Maurer. “Model-based optimization of source locations for 3D acoustic seismic full-waveform inversion”. *Geophysical Prospecting* 71 (2023), pp. 3–16.

[46] S. Wu, D. J. Verschuur, and G. Blacquière. “Automated Seismic Acquisition Geometry Design for Optimized Illumination at the Target: A Linearized Approach”. *IEEE Transactions on Geoscience and Remote Sensing* 60 (2022), pp. 1–13.

[47] Ö. Yilmaz and S. M. Doherty. *Seismic data analysis: processing, inversion, and interpretation of seismic data*. 2nd ed. Investigations in Geophysics. Tulsa, OK: Society of Exploration Geophysicists, 2001.

[48] Y. Zhang, Z. Yin, O. López, A. Siahkoohi, M. Louboutin, R. Kumar, and F. J. Herrmann. “Optimized time-lapse acquisition design via spectral gap ratio minimization”. *Geophysics* 88 (2023), A19–A23.

2

ACQUISITION GEOMETRY ANALYSIS WITH POINT-SPREAD FUNCTIONS

Seismic data are traditionally acquired based on spatial sampling requirements, noise properties, and budgetary constraints. However, designing a survey without taking into account the complexity of the subsurface may result in an image without the expected quality. Also, the subsequent preprocessing and processing steps, may exploit or misuse the acquired data. The design should therefore incorporate the complexity of the subsurface and the (pre)processing steps that will be followed. We propose an analysis method that evaluates if the proposed combination of survey design, preprocessing and processing for a specific subsurface model fulfills a pre-defined quality criterion. With our method we estimate a set of point-spread functions that correspond to the chosen combination and we analyse their resolution and illumination-detection properties in the spatial and wavenumber domains, respectively. The estimated point-spread functions include the scattering and propagation effects generated by the subsurface, including internal multiples. We show that in some cases, the use of internal multiples in imaging can improve amplitude and resolution compared to the use of primaries only. The proposed analysis method is also used to evaluate the effect of blending noise when blended acquisition is carried out.

This chapter was published as Revelo-Obando and Blacquière (2021) in *Geophysical Prospecting*. Minor modifications have been applied to the text for the sake of consistency in the thesis.

2.1. INTRODUCTION

Seismic surveys are traditionally designed based on properties such as fold and azimuth distribution (Vermeer, 2012). However the illumination and detection properties of the survey design could be severely influenced by a complex subsurface. Today, in many parts of the world, there are subsurface models available from legacy surveys. These can be of great value for designing future surveys as the acquisition parameters can be tuned to the particular subsurface structure to provide optimum imaging results.

After seismic data have been acquired, subsequent preprocessing, processing (imaging and velocity estimation) and interpretation (layer property estimation) are carried out. Traditionally, these steps are carried out sequentially and are considered as more or less independent. However, more and more it is recognized that they are strongly interrelated. For instance, the performance of certain data (pre)processing algorithms may strongly depend on the availability of certain well-sampled gathers, i.e., on the data acquisition, and the interpretation could require a certain minimum quality of the seismic image. For that reason, it does not make sense to design an acquisition geometry without taking into account what data (pre)processing steps will follow and what image quality is required. Although each step of the chain will influence the result in a different way, the final product will be affected by the complete sequence.

In this research therefore, the whole seismic imaging method is considered, i.e., a 'holistic approach' is followed. The focus, however is on data acquisition. It means that, in the ideal situation, the acquisition geometry is designed in such a way that - after data processing in a particular pre-defined way - the results have a certain pre-defined image quality. Here, the best design is the cheapest that leads to the goal. As this method is carried out in the pre-acquisition phase, it is fully carried out on synthetic data.

For benchmarking an imaging system, the imaging response of a collection of point scatterers is analyzed. Ideally, for a point scatterer in the subsurface, the result of the imaging process should be a single, well-focused point. However, in practice, a coarse, irregular spatial sampling, a limited acquisition aperture, a complex subsurface and the limitations of the seismic (pre)processing cause the scattered energy to be imaged in non-perfect way: instead of a point, the resulting image has a distorted shape which resembles a band-limited wavelet. The result is called a point-spread function (PSF), and it is defined as the impulse response of the complete system of seismic acquisition, preprocessing and imaging at the location of the point scatterer. The collection of point scatters can be used to determine this impulse response at many locations.

The PSF, which is also called resolution function, has been studied extensively for prestack migration quality analysis (Berkhout, 1984; Beylkin, 1985). Several factors that influence the PSF, are the acquisition geometry, frequency content, background velocity model and the migration algorithm. Vermeer (1999) studies the effect of frequency content, acquisition aperture and geometry on the resolution for a single scatterer in a homogeneous medium. Beylkin (1985) describes migration as a mapping from the acquisition coordinates space to the spatial frequency domain. The range of angles present will determine the spatial resolution. This domain can be obtained numerically via ray tracing for prestack migration. Ray tracing methods provide a computationally efficient way to model the illumination and detection properties of a survey in a complex subsurface (Lecomte, 2008). However, these properties can be either exploited or undermined

by the chosen imaging algorithm.

In current imaging, the multiples (surface-related multiples as well as internal multiples) are not considered as noise, but instead they are considered as valuable signal. The handling of multiple reflections by the imaging algorithm may contribute to the imaging results, potentially relaxing the spatial sampling requirements. In Marchenko imaging for instance (Wapenaar et al., 2014), the estimated Green's functions include the internal multiple reflections that contribute to reflectivity estimation. Free-surface related multiple reflections can also be taken into account (Singh et al., 2015; Singh et al., 2017). Least-squares and inversion approaches offer the same possibility (Brown and Guitton, 2005; Malcolm et al., 2009; Zhang and Schuster, 2014; Tu and Herrmann, 2015). In particular the multiples may contribute if imaging by primaries is impossible, e.g., in the cases that primaries do not reach the particular area to be imaged with sufficient signal strength but multiples do. Consequently, the image quality depends on the subsurface reflectivity: only if sufficiently strong reflectors are present, the (internal) multiples are likely to contribute to the imaging; if not, their contribution can be ignored. In the first case, the use of an imaging algorithm such as Full-Wavefield Migration (FWM) (Davydenko, 2016) that uses all the multiples, can compensate for illumination in areas where the illumination by primaries only is not sufficient. This approach may reduce the sampling requirements in the acquisition surface, thereby reducing costs. In a similar manner, if a dataset known for having strong multiples is processed with a primary-only migration, the signal corresponding to these multiples will not be processed adequately, resulting in undesired artifacts. In such a case, more data may be required in order to obtain an image with a sufficient signal to noise ratio. Therefore, when designing an acquisition geometry, the processing methodology should be taken into account for an optimum result.

The so-called focal beam analysis (Berkhout et al., 2001) provides a method to analyze the acquisition geometry of a survey based on the illumination and detection properties of the sources and receivers respectively. The complexity of the subsurface can be taken into account (van Veldhuizen et al., 2008) as well as the illumination by all multiples (Kumar, 2015). However the process is only efficient for analyzing a couple of target points in the subsurface. Repeating this process for all subsurface locations makes it too expensive.

Blended, or simultaneous source acquisition (Beasley et al., 1998; Berkhout et al., 2008; Bouska, 2010) allows to use seismic sources whose responses overlap in time and space as well as in temporal and spatial frequency bands. Compared to conventional acquisition a higher efficiency can be achieved. With algorithms such as FWM the blended data can be directly processed, i.e., without deblending, reducing the total number of shots and therefore increasing the computational efficiency. For other, more conventional algorithms it is desired to deblend the records before further processing. In this case the design of the blended acquisition has to be such that it allows for an optimal reconstruction of the unblended wavefields. As different deblending methods may pose different requirements on the spatial sampling of the input data and the allowed maximum blending factor, it is necessary to take these into account when designing the acquisition geometry.

In order to measure the performance of the seismic experiment, it is necessary to

define an analysis method. The result of such an analysis would be a quantitative measure that allows one to judge wether or not the pre-defined quality criteria are met. In this chapter we focus on this analysis method, using the following approach. With the available velocity model we compute a set of PSFs by first modeling a seismic data set for the original reflectivity model and then modeling a second seismic data set for an almost identical model: the only difference is that a grid of point scatterers is added to the original reflectivity. Both datasets are preprocessed and imaged in the same way. The difference between the two final images is the sought set of PSFs. By computing the PSFs in this way, the effect of acquisition, preprocessing and imaging are all taken into account, and specially, if present, the contribution of multiples to the imaging. The PSFs are quantitatively analyzed to assess the quality of the seismic experiment.

2.2. FRAMEWORK OF SURVEY ANALYSIS

We describe 3D seismic data using the matrix notation introduced by Berkhout (1982). For each frequency component, a dataset can be formulated as:

$$\mathbf{P}(z_d; z_s) = \mathbf{D}(z_d)\mathbf{X}(z_d, z_s)\mathbf{S}(z_s), \tag{2.1}$$

where $\mathbf{P}$ is the seismic signal recorded at depth level z_d, generated by the sources at level z_s. Each element contains the amplitude and phase information of one shot record, recorded by one receiver, for the frequency component under consideration. $\mathbf{S}$ and $\mathbf{D}$ are the source and receiver matrix respectively. Together they describe the survey geometry (number of sources and receivers and their locations), as well as the source and receiver properties (directivity, spectral properties, etc.). Matrix $\mathbf{X}$ represents the transfer operator of the medium, and contains propagation and reflection effects. It can be considered to be the ideal-sampled seismic data.

The modeling is carried out with full-wavefield modeling (FWMod) (Berkhout, 2014). In FWMod the modeling is recursive in depth. First the downgoing wavefield is computed, and then the upgoing wavefield. These two steps are called one round trip. The implementation requires multiple round trips, each round trip adding one additional order of multiple reflections:

$$\overrightarrow{P}_i^{+}(z_n) = \sum_{m=0}^{n-1} \mathbf{U}^{+}(z_n, z_m)\left[\overrightarrow{S}^{+}(z_m) + \mathbf{R}^{\cap}(z_m)\overrightarrow{P}_{i-1}^{-}(z_m)\right], \tag{2.2a}$$

$$\overrightarrow{P}_i^{-}(z_n) = \sum_{m=n+1}^{N} \mathbf{U}^{-}(z_n, z_m)\left[\overrightarrow{S}^{-}(z_m) + \mathbf{R}^{\cup}(z_m)\overrightarrow{P}_i^{+}(z_m)\right]. \tag{2.2b}$$

Vector $\overrightarrow{P}_i^{+}(z_n)$ is the downgoing wavefield at depth level z_n for round trip i. Vector $\overrightarrow{P}_i^{-}(z_n)$ corresponds to the upgoing wavefield. Matrices $\mathbf{R}^{\cap}(z_m)$ and $\mathbf{R}^{\cup}(z_m)$ are the up-down and down-up angle-dependent reflection operators at depth level z_m. Vector $\overrightarrow{S}^{+}(z_m)$ is the downgoing source wavefield at depth level z_m. Vector $\overrightarrow{S}^{-}(z_m)$ corresponds to the upgoing source wavefield. Operator $\mathbf{U}^{+}(z_n, z_m)$ includes the propagation and transmission effects in the downgoing direction from depth level z_m to depth level z_n, and so does operator $\mathbf{U}^{-}(z_n, z_m)$ for wavefields propagating in the upward direction. They are computed as follows:

$$\mathbf{U}^{+}(z_n, z_m) = \left[\prod_{k=n-1}^{m+1} \mathbf{W}^{+}(z_{k+1}, z_k)\mathbf{T}^{+}(z_k)\right]\mathbf{W}^{+}(z_{m+1}, z_m), \tag{2.3a}$$

$$\mathbf{U}^{-}(z_n, z_m) = \left[\prod_{k=n+1}^{m-1} \mathbf{W}^{-}(z_{k-1}, z_k)\mathbf{T}^{-}(z_k)\right]\mathbf{W}^{-}(z_{m-1}, z_m). \tag{2.3b}$$

Here $\mathbf{W}^{+}(z_{k+1}, z_k)$ is the downward propagation operator from depth level z_k to depth level z_{k+1}; $\mathbf{W}^{-}(z_{k-1}, z_k)$ is the upward propagation operator from depth level z_k to depth level z_{k-1}; $\mathbf{T}^{+}(z_k)$ is the transmission operator of the downgoing wavefield crossing depth level z_k from above; $\mathbf{T}^{-}(z_k)$ is the transmission operator of the upgoing wavefield crossing depth level z_k from below.

The use of this type of modeling allows to specify reflectivity and transmissivity independently from propagation velocity. The outcome of the modeling process after N round trips (corresponding to the order of multiples being modelled) is the seismic signal $\overrightarrow{P}^{-}_{N}$ at the recording surface z_d. The modeling is repeated for multiple sources at the surface z_s, resulting in the data matrix $\mathbf{P}(z_d; z_s)$ in equation 2.1. Note that the number of round trips N is also indicative for the cost ratio between using FWMod and using primaries-only modeling. This scheme is equivalent with a Bremmer series expansion. See Davydenko (2016) for details.

To get a blended data set $\mathbf{P}^{'}(z_d; z_s)$, we multiply the unblended data with blending operator $\mathbf{\Gamma}(z_s)$ (Berkhout et al., 2008):

$$\mathbf{P}^{'}(z_d; z_s) = \mathbf{P}(z_d; z_s)\mathbf{\Gamma}(z_s). \tag{2.4}$$

Matrix $\mathbf{\Gamma}(z_s)$ contains the blending code i.e., time delays or phase shifts for simultaneous sources. Each column of $\mathbf{\Gamma}(z_s)$ represents a blending experiment and each row the specific source to be blended.

To simplify the notation, we assume that the sources and the receivers are located at the same acquisition surface, so that z_d and z_s can be omitted.

2.3. COMPUTING POINT-SPREAD FUNCTIONS

NUMERICAL MODELING

In a numerical experiment, the calculation of a PSF involves the modeling of seismic data with a chosen acquisition geometry and subsurface model. As mentioned in the introduction, to obtain the PSFs corresponding to a complex subsurface, two datasets are modeled. The first, $\mathbf{P}_1$ corresponds to the original reflectivity model, and the second, $\mathbf{P}_2$ corresponds to the second reflectivity model which is the sum of the original reflectivity model and an additional grid of point scatters. The original velocity model is used for modeling both datasets. This is possible because FWMod allows specifying reflectivity independently from propagation velocity. Therefore, we use this as a means to simulate the presence of the point scatterers while taking into account the complexity of the

subsurface. The obtained datasets are:

$$\mathbf{P}_1 = \mathbf{P}, \tag{2.5}$$

$$\mathbf{P}_2 = \mathbf{P} + \Delta\mathbf{P}. \tag{2.6}$$

Here $\mathbf{P}$ is the data related to the original subsurface, and $\mathbf{P} + \Delta\mathbf{P}$ is the data related to the subsurface plus point-scatterers. These scatterers have a low reflectivity. This is to make sure that the multiples in $\mathbf{P}_2$ that contribute to the imaging are mostly present in $\mathbf{P}$, and not in $\Delta\mathbf{P}$. In the case of blended acquisition, these data sets become $\mathbf{P'}_1$ and $\mathbf{P'}_2$.

IMAGING

We choose FWM to illustrate the possible advantages that the use of the full wavefield in imaging could bring to survey design. FWM is an inversion based algorithm that aims to estimate the reflectivity for a given dataset. We assume the velocity model is known. However, it is possible to combine reflectivity estimation with velocity estimation in the so-called Joint Migration-Inversion (JMI) (Staal, 2015). Here we focus on the imaging only, i.e., on the reflectivity estimation. In our examples we simplify the reflectivity to be angle-independent (i.e., the reflection operators become reflection coefficients and, consequently, $\mathbf{R}^{\cap}$ and $\mathbf{R}^{\cup}$ become diagonal matrices).

In FWM, the reflectivity model is iteratively updated by computing the data residual, i.e., the difference between the observed data and the data forward-modeled through FWMod. This data residual is mapped to the model space via adjoint modeling. After proper scaling, the update is applied to the current reflectivity model. A complete mathematical description is offered by Davydenko (2016).

Two images are obtained after processing $\mathbf{P}_1$ and $\mathbf{P}_2$ in exactly the same way. These are $\mathbf{I}_1$ and $\mathbf{I}_2$ respectively:

$$\mathbf{I}_1 = \mathbf{I}, \tag{2.7}$$

$$\mathbf{I}_2 = \mathbf{I} + \delta\mathbf{I} + \Delta\mathbf{I}. \tag{2.8}$$

Here $\mathbf{I}$ is the reflectivity image of the subsurface, i.e., the collection of estimated $\mathbf{R}$'s for all depth levels obtained after preprocessing and processing of dataset $\mathbf{P}_1$. The term $\mathbf{I} + \delta\mathbf{I}$ on the right hand side of equation 2.8 is the reflectivity image of the original subsurface model, that differs from $\mathbf{I}$ by the term $\delta\mathbf{I}$ due to the possible influence of the scattering $\Delta\mathbf{P}$ from equation 2.6 on the imaging. The term $\Delta\mathbf{I}$ is the reflectivity image of the point scatterers, generated by $\Delta\mathbf{P}$. As we chose the reflectivity of the point scatterers to be small compared to the reflectors in the original model, we neglect the possible multiples generated by the scatterers. Therefore, for FWM, the image contribution $\delta\mathbf{I}$ can be neglected as well. By subtracting the two reflectivity images $\mathbf{I}_2$ and $\mathbf{I}_1$, the reflectivity image of the point scatterers, $\Delta\mathbf{I}$, is obtained. The latter is the collection of PSFs mentioned earlier. The theory presented in this and the previous section is valid for 2D and 3D seismic experiments. However, for convenience, we present 2D examples in the remainder of this chapter.

To illustrate the concept of PSFs as discussed in this section, we selected a part of the Marmousi model (Figure 2.1) to model seismic data using FWMod. One data set is modeled using the original reflectivity model (Figure 2.1b). We then added a collection

of 81 point scatterers to the same model, distributed regularly in the subsurface (Figure 2.1c), and modeled a second seismic data set. The original velocity model (Figure 2.1a) was used in both datasets. The spatial sampling of the sources and receivers was ideal in the two data sets and both sets were (pre)processed in exactly the same way. Finally, the two obtained reflectivity images were subtracted, resulting in the set of PSFs shown in Figure 2.2. It is these PSFs that can be further analysed. This analysis is the topic of the next section.

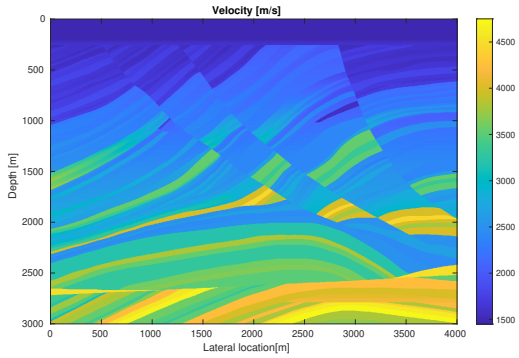

(a) Velocity model.

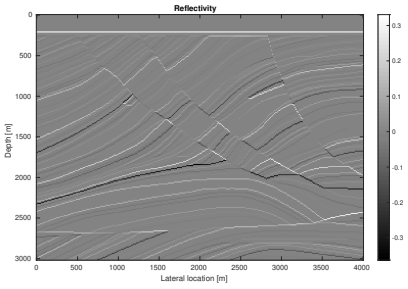

(b) Reflectivity model.

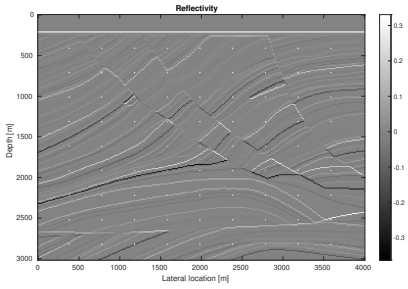

(c) Original reflectivity plus grid of point-scatterers. The latter were amplified 10 times for display.

Figure 2.1: Section of the Marmousi model.

2.4. QUANTITATIVE ANALYSIS

2.4.1. RESOLUTION AND ILLUMINATION-DETECTION

To quantify the quality of the final image, the individual PSFs are analyzed. Each of them can be considered separately in order to obtain the resolution in the image domain and involved angle-distribution in the wavenumber domain at the location of each scatterer. Figure 2.3 shows the results for the ideal (band-limited) image of a point scatterer in the spatial and wavenumber domains. The PSF in the spatial domain shows a well-focused

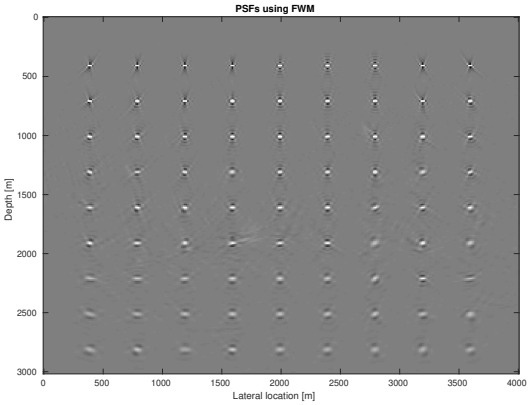

Figure 2.2: Set of PSFs corresponding to the model in Figure 2.1a. The acquisition geometry consists of a uniform spatial sampling of sources and receivers. Note the the PSFs are different, depending on their location in the model.

event whose sharpness is limited by the bandwidth of the seismic data. The wavenumber spectrum on the right shows a full range of illumination and detection angles, see the yellow area. Again, its limited radial extent is the result of the band limitation. It is only possible to obtain this type of image when having sources and receivers all around the scatterer. In practice, acquisition is done with sources and receivers at the surface only. Therefore, even with a hypothetical infinite aperture, it is not possible to obtain the well-focused image on Figure 2.3, as shown next.

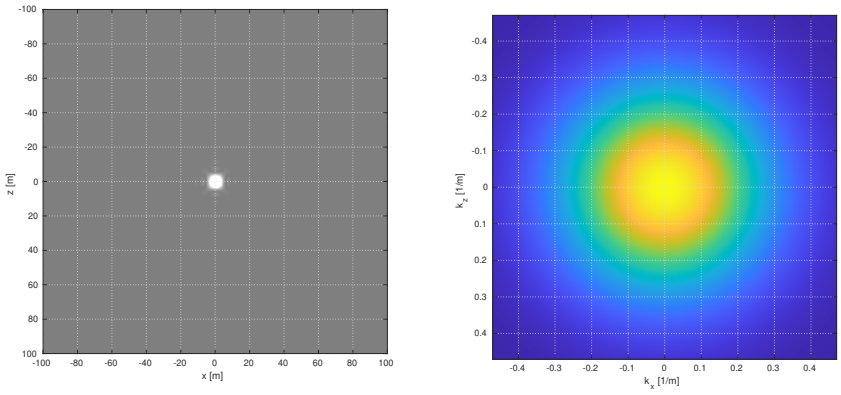

(a) PSF in image domain.

(b) Corresponding wavenumber spectrum

Figure 2.3: (a) Image of a well illuminated point-scatterer. The wavenumber domain transformation (b)contains a complete range of illumination-detection angles. The resolution is only limited by the seismic bandwidth.

Figure 2.4 shows a set of one hundred PSFs. In this example, the acquisition geometry consists of a uniform spatial sampling of sources and receivers and the model velocity is constant. One of the PSFs has been selected for a zoomed view in 2.4b and its corresponding spectrum is shown in in 2.4c. Ideally, the point scatterer should be present at its true position only, being (x, z) = (1813, 2488) m. However the energy is spread in an area tens of meters around that position. In addition, the PSF is no longer circularly symmetric, it has instead a shape whose cross-sections resemble band-limited wavelets.

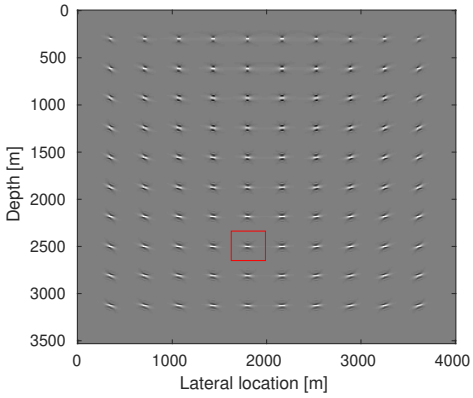

(a) Set of PSFs.

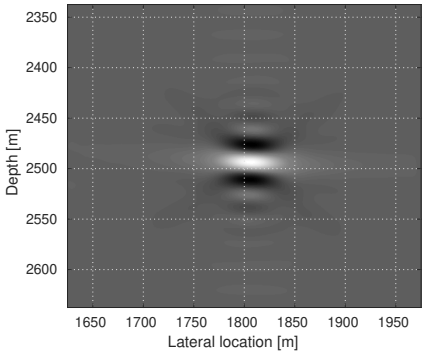

(b) PSF in the red box in (a).

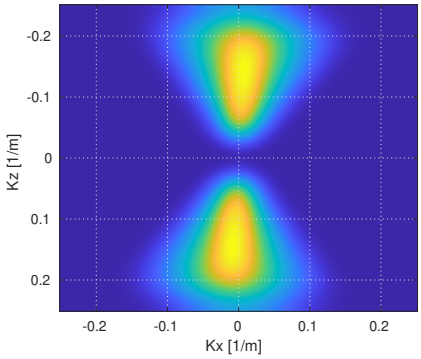

(c) Wavenumber spectrum of (b).

Figure 2.4: Set of PSFs (a), zoomed image of the PSF in the red box (b), its wavenumber spectrum (c). The PSF in (b) is no longer symmetrical as in Figure 2.3. The wavenumber spectrum in (c) shows the illumination and detection deficiencies.

For a Ricker wavelet as source pulse, a Ricker wavelet shape is obtained in the vertical direction. A Gaussian spatial wavelet is obtained in the horizontal direction (Von Seggern, 1991). These cross sections are not strictly vertical or horizontal but have an orientation related to the illumination and detection angles at the position of the point

scatterer. Each PSF may have a different orientation which we call the inclination angle. This inclination is more evident for the PSFs closer to the edges, as the acquisition aperture seen by the corresponding point scatterers is relatively small compared to the aperture seen by point scatterers in the central section. The wavenumber spectrum shows a bowtie shape. Compared to Figure 2.3, the higher angles are missing. Also it can be seen that the very low frequencies are no longer present. The angles and frequencies present in the wavenumber spectrum correspond to the combined effect of angles of illumination by the sources and angles of detection by the receivers and their combined spectral properties.

To compute a quantitative measure of resolution and to identify the inclination angle of the PSF, we analyze the two cross sections that pass across the point of maximum amplitude of the PSF. As mentioned, two axes can be distinguished in a PSF. First, a lower-resolution axis, along which the PSF has a Gaussian shape. Second, usually perpendicular to the first, a higher-resolution axis. For the latter, we compute its envelope by taking the magnitude of the analytical signal. Then, we measure the distance between the points with half of the peak amplitude. The low resolution axis is defined as the cross section with the longest distance between these two points. The high resolution axis has the shortest distance between those two points. These distances are our measures of resolution (see Figure 2.5).

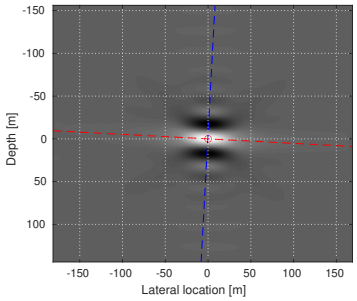

(a) PSF and its cross-sections.

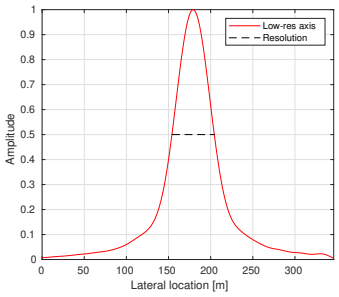

(b) Low-resolution axis.

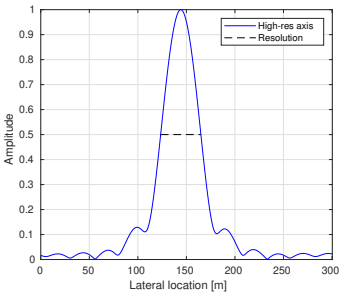

(c) High-resolution axis.

Figure 2.5: (a) Example of a PSF with its low (b) and high (c) resolution axes across the point of maximum amplitude. The amplitudes in (b) and (c) are normalized and treated separately.

The resolution measurements can be computed for all PSFs in the subsurface. Figure 2.6 shows the measure of resolution for the set of PSFs in Figure 2.2. The high and low resolution measures are displayed in Figure 2.6a and 2.6b respectively. The arrows indicate the orientation of the respective axes. Their length corresponds to the respective measures of resolution, i.e., the longer the arrow, the lower the resolution. In addition, this resolution has been computed for the whole subsurface via interpolation between PSFs and color-coded in the background. The measurements of high-resolution (Figure 2.6a) show a tendency of decreasing with depth. The main reason is the increase of seismic velocities with depth. The yellow part at the lower-right section coincides with the higher velocities observed in Figure 2.1a. The measurements of low-resolution (Figure 2.6b) show a similar trend. As the acquisition aperture seen by the point-scatterers decreases with depth, the range of illumination and detection angles decreases, and therefore so does the resolution.

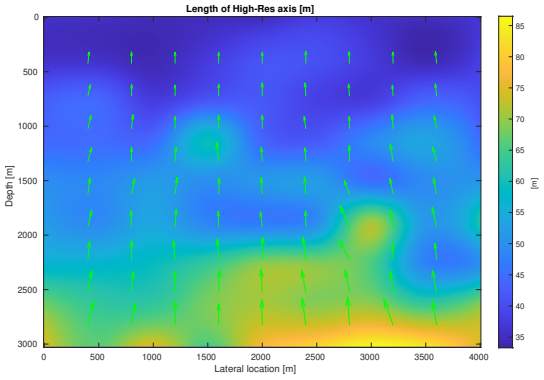

(a) High resolution axis measurement.

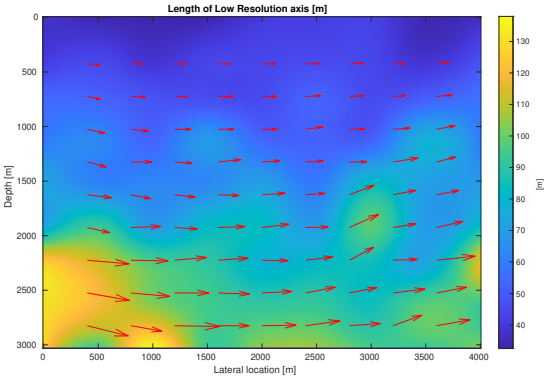

(b) Low resolution axis measurement.

Figure 2.6: (a) The measurements of the high-resolution indicate a decreasing trend with depth. Resolution is specially low in the deeper part of the model. (b) The low resolution measurement indicates a similar trend of decreasing resolution with depth and structurally complex zones.

2.5. EXAMPLES

2.5.1. EFFECT OF IMAGING

In traditional prestack depth migration multiples are considered as noise. Therefore, they need to be eliminated before imaging. In full-wavefield imaging methods, multiples are not eliminated but used to estimate reflectivity. As pointed out in the introduction, multiple reflections may reach areas in the subsurface that primaries do not. In particular internal multiples, generated deeper in the subsurface than surface-related multiples, may provide additional illumination from below. In this section, we use the proposed analysis method to evaluate the effect of using internal multiples for imaging. For synthetic models and different acquisition scenarios, we compute sets of PSFs using FWM as well as primaries-only migration. For the latter, we use a least-squares migration with a correlation-type imaging condition, which only considers the primary wavefield in its modeling engine (FWMod with N=1). Therefore, multiple reflections do not contribute to the reflectivity estimation in that case. Subsequently we measure resolution, analyse illumination-and-detection and evaluate the differences.

First, we consider a setup with two synthetic models of a salt dome embedded in a layered medium (Figure 2.7). The velocity of the deepest layer, i.e., below $z = 1000$ m, is 2000 m/s for model 1 (Figure 2.7a) and 3300 m/s for model 2 (Figure 2.7a). The density is kept constant. The reflectivity of the interface at $z = 1000$ m is 0.05 and 0.34 for models 1 and 2, respectively. A different reflectivity at this interface means that the amplitude of the reflected upgoing wavefield, and hence the strength of the (internal) multiples is different. The amplitude of these internal multiples is proportional to the reflectivity of that interface, i.e., weak internal multiples in the first case and strong internal multiples in the second. These internal multiples may be used for imaging depending on the chosen imaging method. It is of interest to have a good image of the area beneath the flank of the salt, as we assume that a target of economic importance is located there.

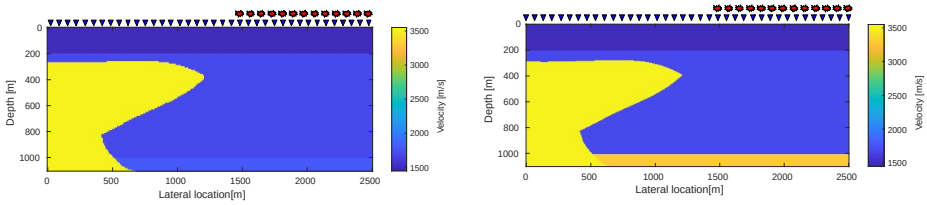

(a) Model 1

(b) Model 2

Figure 2.7: Salt dome models. The reflectivity of the interface at $z = 1000$ is lower for model 1 (a) than for model 2 (b). The latter generates stronger internal multiples. The red stars on the top of both models indicate the position of the sources. The blue triangles indicate the position of the receivers.

We consider an acquisition scenario in which the receivers are placed at the complete acquisition surface, while the sources are located at the right side only, i.e., from $x = 1400$ m to $x = 2500$ m. Seismic data are modeled with FWMod and migrated using primaries-only migration (Figure 2.8). Figure 2.8a corresponds to the reflectivity image of model 1, while Figure 2.8b is the reflectivity image of model 2.

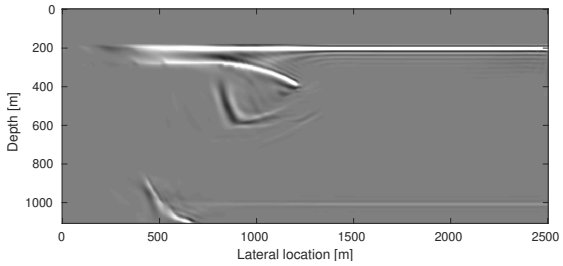

(a) Reflector at $z = 1000$ m with $R = 0.05$

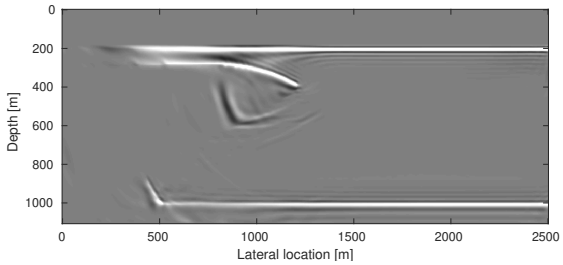

(b) Reflector at $z = 1000$ m with $R = 0.34$

Figure 2.8: Images of models 1 (a) and 2 (b) using primaries-only migration. With this setup of acquisition geometry and imaging it is not possible to image the flank of the salt dome. There is an artifact (false structure) inside the salt dome.

Figure 2.8 shows that with primaries-only migration, the reflector at $z = 1000$ m in models 1 and 2 is clearly imaged. It is much stronger in Figure 2.8b than in Figure 2.8a, as expected. As the sources are only located at the right side, given the geometry of the model, there will not be primary reflections generated by the flank of the salt that are recorded by the receivers. Therefore, it is not possible to obtain an image of this section using primaries-only migration. None of the images contains the flank of the salt dome. Additionally, strong artifacts appear inside the salt dome. The multiple reflections between the top of the salt dome and the water bottom cannot be explained by this type of imaging. Hence, they appear as spurious events beneath the top of the salt.

Figure 2.9 shows the imaging results for both models using FWM. Even for the case of weak internal multiples, in Figure 2.9a a part of the flank of the salt is imaged. The artifacts in Figures 2.8a and 2.8b are no longer present. The flank is better imaged when stronger internal multiples are present (Figure 2.9b). It is important to note that the synthetic data generated for these examples are noise-free. In the presence of noise, it is possible that the weak internal multiples are not strong enough to obtain a signal to noise ratio (SNR) suitable for imaging the target zone. Therefore, stronger internal multiples may be needed, as those used for the imaging in Figure 2.9b. To analyse the difference in resolution and illumination, we calculate a set of PSFs for model 2. Figure 2.10 shows a comparison between the PSFs obtained with primaries-only migration and FWM.

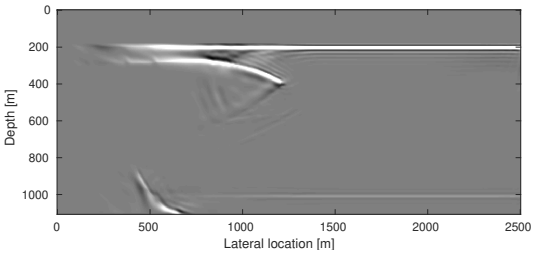

(a) Reflector at $z = 1000$ m with $R = 0.05$

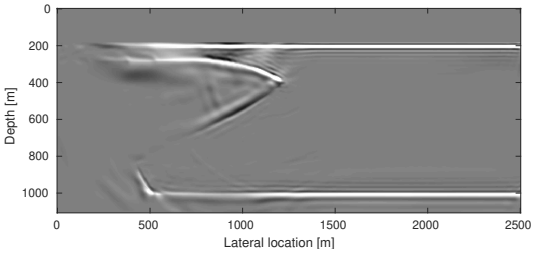

(b) Reflector at $z = 1000$ m with $R = 0.34$

Figure 2.9: Images of models 1 (a) and 2 (b) using FWM. When using the internal multiples the flank of the salt dome is imaged. With stronger internal multiples the image further improves. The artifacts inside the salt dome in Figure 2.8 are no longer present.

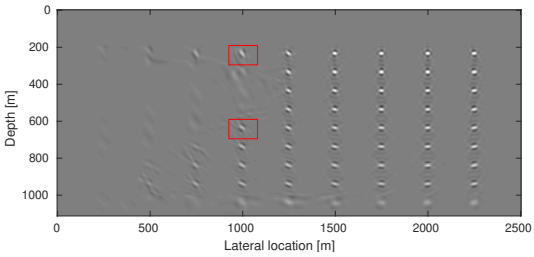

(a) Primaries-only migration.

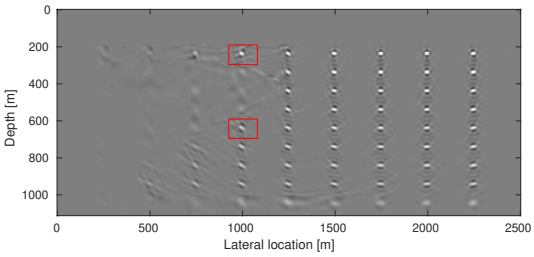

(b) FWM.

Figure 2.10: Set of PSF obtained with primaries-only migration and FWM.

The PSFs in the right hand side for both models are almost identical. The point-scatterers in this part of the model are well-illuminated by the primary wavefield. Therefore, primaries-only migration suffices to obtain a good image. This is not the case for the point scatterers beneath the flank of the salt dome. There, the PSFs from the primaries-only migration (Figure 2.10a) have a lower resolution and amplitude than the PSFs from the FWM (Figure 2.10b). This is because the internal multiples generated between the salt dome and the interface at $z = 1000$ m are used for imaging. Figure 2.11 shows a comparison between the PSFs centered at $(x, z) = (1000, 640)$ m (lower red boxes in Figures 2.10a and 2.10b).

Figure 2.11b shows the PSF obtained through FWM. It has a higher amplitude than the one obtained through primaries-only migration (Figure 2.11a). The energy from the internal multiples is now used for imaging, therefore it contributes to the reflectivity estimation. The red lines in both figures correspond to the low-resolution axes. In order to compare their resolution, they are normalized and plotted in Figure 2.11c. The low-resolution axis corresponding to FWM has a better resolution than the the one corresponding to primaries-only migration. The wavenumber spectrum of the FWM PSF (Figure 2.11e) shows a wider range of illumination and detection angles than the spectrum of the primaries-only PSF (2.11d). The improvement in resolution and amplitude is more evident in the region above the salt dome. Figure 2.12 shows the illumination and detection angles for the PSF at $(x, z) = (1000, 240)$ m (upper red boxes in Figures 2.10a and 2.10b). Here there are strong internal multiples reflected between the top of the salt and the water bottom. As there are no sources at the acquisition surface directly above this region, the additional illumination by the internal multiples helps to improve the image of the zone considerably.

To illustrate the procedure for a more complex subsurface model and a more challenging acquisition scenario, we calculate a set of PSFs for the Marmousi model (Figure 2.1). The acquisition geometry consists of receivers at the complete surface and a gap in the source distribution from $x = 1000$ m to $x = 3000$ m, assuming there is an obstacle in this region. As in the previous examples, our seismic data were modeled without surface-related multiples and we focus on the effects generated by the internal multiples. Figure 2.13 shows a comparison between the PSFs obtained with primaries-only migration and the ones obtained with FWM.

It is visible that for both cases the acquisition gap has a considerable effect. When comparing with the PSFs in Figure 2.4, which correspond to a full source sampling, artifacts appear in both images in the region beneath the source gap, at the center of the model. The primaries-only migration result is more affected as it relies on the primary reflections generated by the wavefield of the adjacent sources. Therefore, the shallower PSFs have a decreased resolution. The difference plot shows that the PSFs in this part have more energy in the FWM case. This difference can be attributed to the internal multiples used for the imaging, as the acquisition geometry is kept constant.

The additional illumination provided by the internal multiples could help to reduce the spatial sampling requirements of the survey. To illustrate this we compare the PSFs obtained from two acquisition geometries, see Figure 2.14. The source interval is 125 m for the first geometry and 500 m for the second. The spatial sampling of the receivers is 12.5 m for both geometries. Figure 2.14a shows the set of PSFs for the first geometry

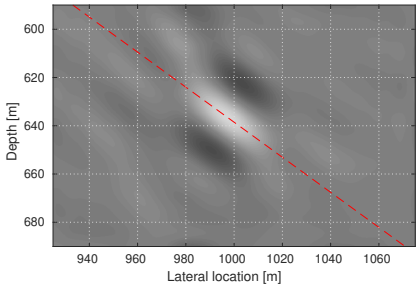

(a) Primaries-only migration.

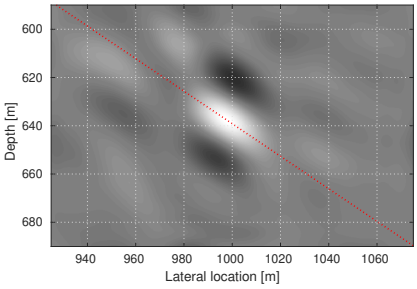

(b) FWM.

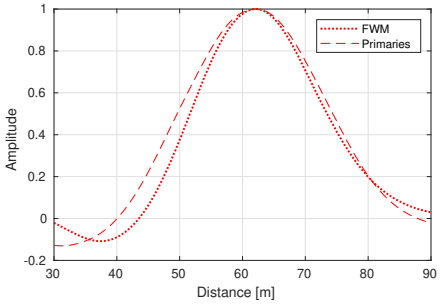

(c) Comparison of low-resolution axes envelopes.

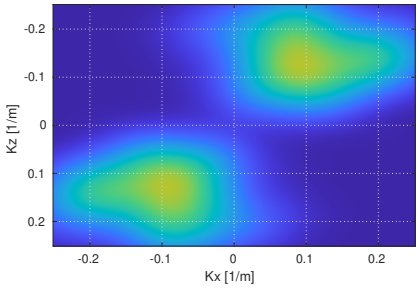

(d) Wavenumber spectrum. Primaries-only migration.

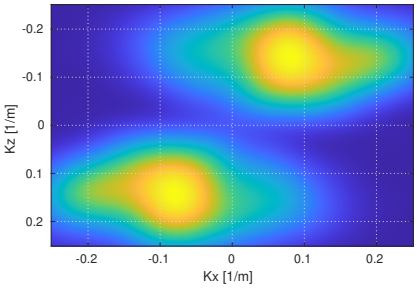

(e) Wavenumber spectrum. FWM.

Figure 2.11: Zoom at the PSF centered at $(x, z) = (1000, 640)$ m for primaries-only migration (a) and FWM (b). The low-resolution axis show a better resolution for the FWM PSF than for primaries-only migration (c). The wavenumber spectrum of primaries-only migration PSF (d) shows a reduced angle coverage compared to the FWM spectrum (e).

and Figure 2.14b for the second. Figure 2.14c shows their difference. The differences are barely noticeable. This means that even with the sparse source distribution, a good result was obtained. Note that in general the 'interpolating effect' of the use of multiples is expected to be largest when surface-multiples are used. However, we didn't use these as our focus is on the contribution of internal multiples.

The examples in Figure 2.14 allowed to analyse the effect of different acquisition geometries while the processing algorithm remained the same. The analysis method shows

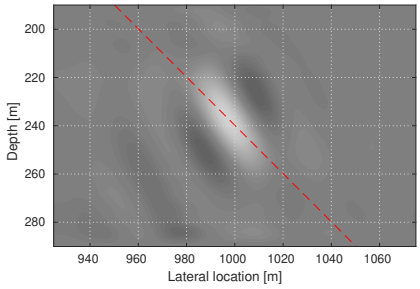

(a) Primaries-only migration.

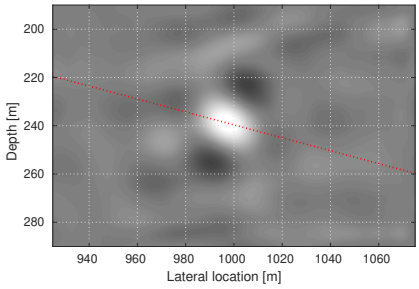

(b) FWM.

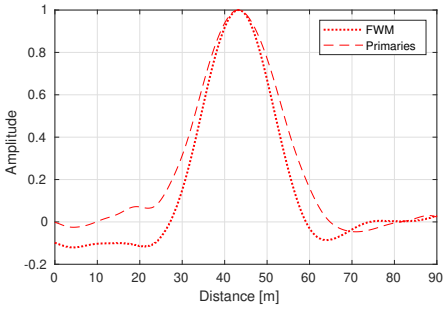

(c) Comparison of low-resolution axes cross sections.

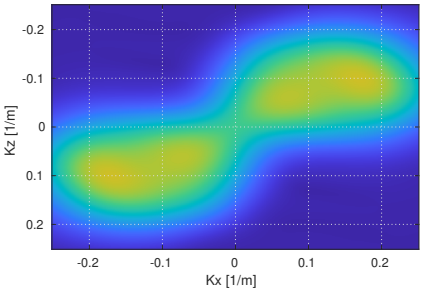

(d) Primaries-only migration.

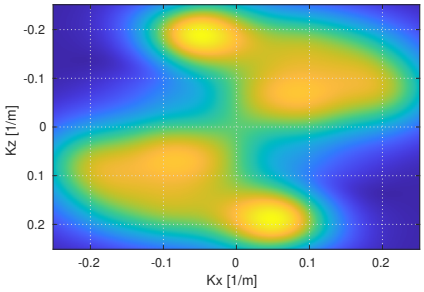

(e) FWM.

Figure 2.12: Illumination analysis for the PSF at $(x, z) = (1000, 240)$ m. The FWM PSF (b) has larger amplitude and is sharper than the primaries-only case (a). The cross-sections in (c) show a better resolution for FWM than for primaries-only migration. The wavenumber spectrum of the FWM case (e) shows angles of illumination and detections that are absent in the primaries-only spectrum (d). The already present angles are further strengthened with FWM.

the joint effect of illumination by the sources and detection by the receivers for all locations in the subsurface. If the separate effects of the sources and the receivers are needed, for instance in survey design, our method could be complemented with the focal beam analysis method for a couple of target locations.

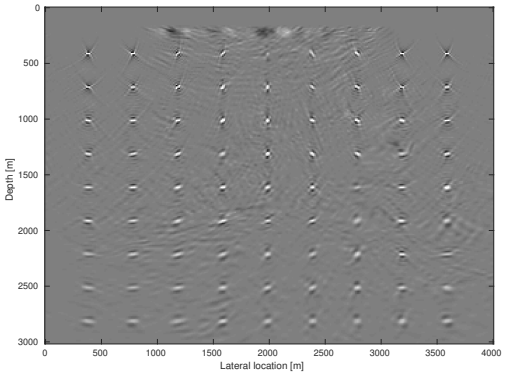

(a) Primaries-only migration

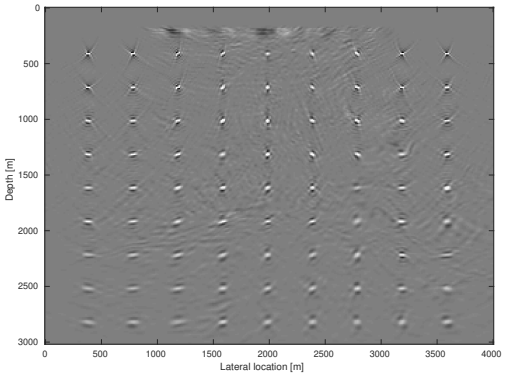

(b) FWM.

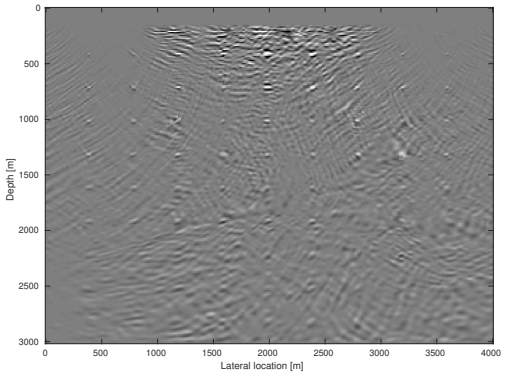

(c) Difference: (b)-(a).

Figure 2.13: Set of PSFs for the model on Figure 2.1. There is a gap in the source distribution from $x = 1000$ m to $x = 3000$ m. Primaries-only migration (a) and FWM (b) PSFs. The difference plot (c) shows that in most of the PSFs, there is additional energy in the FWM image.

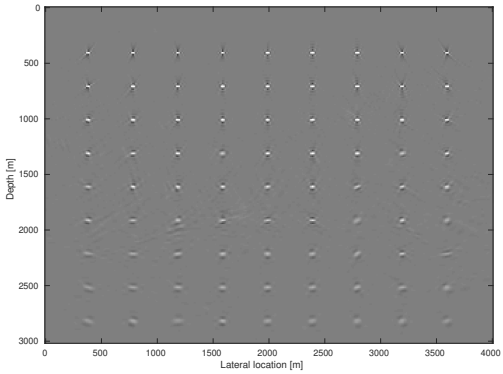

(a) FWM PSFs with sources every 125 m.

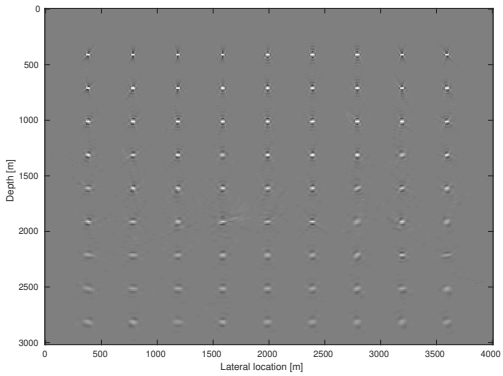

(b) FWM PSFs with sources every 500 m.

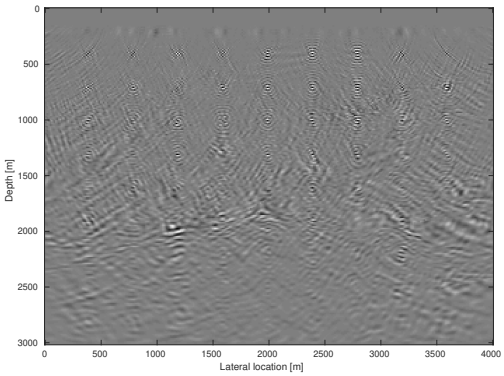

(c) (a)-(b) amplified 20 times. SNR = 12.12 dB.

Figure 2.14: Set of PSFs for the model on Figure 2.1 using different source sampling intervals.

2.5.2. EFFECT OF PREPROCESSING

The preprocessing used to deblend seismic records can leave undesired (blending) noise. In this section we examine the blending noise from the PSFs. Figure 2.15 shows a comparison of the PSFs obtained for the model in Figure 2.1a, for the cases of deblended data (2.15a), pseudo-deblended data (Figure 2.15b) and their differences with respect to the unblended case (Figures 2.15c and 2.15d respectively). The blended datasets corresponds to the sources located in the range from $x = 0$ m to $x = 2000$ m being blended with those in the range from $x = 2000$ m to $x = 4000$ m. Each blended experiment consists of two sources separated by 2000 m and with random time delays ranging from 0 ms to 200 ms between the shots. The deblending algorithm uses an iterative process where coherency filters and thresholding are applied in the common-receiver domain to remove the blending noise (Mahdad et al., 2011). Figure 2.15c shows the effect of the blending noise once observed in the image domain when using FWM. The measured SNR was 7.52 dB. When using pseudo-deblending only (Figure 2.15b), the blending noise in the image domain is considerably larger (Figure 2.15d), leading to an SNR of -11.33 dB.

This result shows the combined effect of the acquisition geometry, the chosen preprocessing algorithm and the chosen imaging algorithm. In this case, carpet shooting and detection were used, so there is no further improvement possible for the acquisition geometry. It means that if the blending noise in the final image is considered to be too large, a better-quality deblending algorithm has to be used. Or, alternatively the blending code (blending factor and time delays) should be chosen such that better deblending results are obtained. Here, we assume that the choice of imaging algorithm would be less relevant and that a lower-quality deblending would always result in a lower-quality final image.

A similar type of analysis could be carried out to assess the performance of denoising algorithms in the preprocessing stage. For instance, two different denoising algorithms could be applied to the same dataset-with-noise to get two denoised datasets. Subsequently, the corresponding sets of PSFs could be computed and the corresponding SNR ratios estimated with respect to the PFSs of the noise-free case. This would provide a quantitative criterion for comparing the performance of the different denoising algorithms after the complete chain of acquisition, preprocessing and imaging.

2.6. CONCLUDING REMARKS

Our proposed analysis method makes use of a-priori knowledge of the subsurface to evaluate how a target point in the subsurface is illuminated and how its seismic response is detected. It takes into account the complete chain of seismic acquisition, preprocessing and imaging. The result is a set of PSFs that are analysed to determine the local resolution and amplitude fidelity in the final image. In our study, we chose to study the effect of the internal multiples. To this end, the subsurface model should contain the major reflectors which control the amplitude of the internal multiples. If strong internal multiples are present, they may help to illuminate exploration targets in areas where illumination by primaries is insufficient. Subsequently, the signal-to-noise ratio can be improved. It was shown that the use of internal multiples can provide additional imaging energy and improve resolution.

To compute PSFs for the case of an imaging algorithm that makes use of multiples,

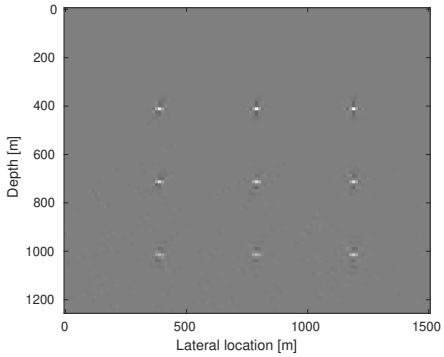

(a) PSFs for deblended data. SNR = 7.52 dB.

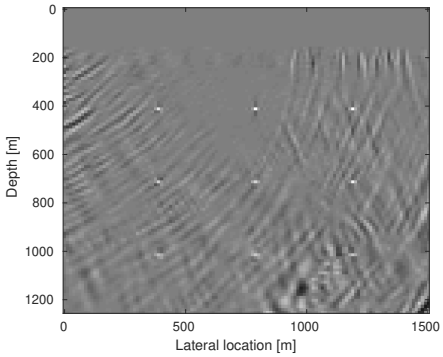

(b) PSFs for pseudo-deblended data. SNR = −11.33 dB.

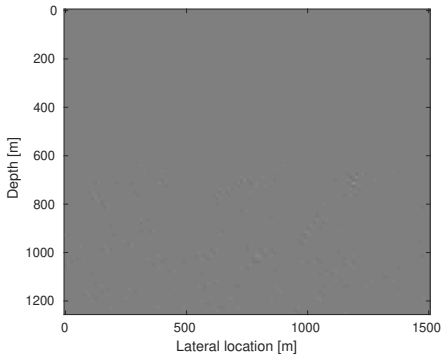

(c) Difference between (a) and the unblended case.

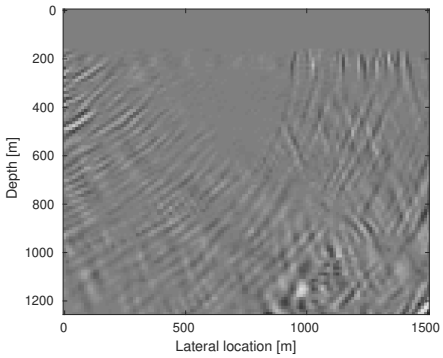

(d) Difference between (b) and the unblended case.

Figure 2.15: PSFs for deblended data, pseudo-deblended data and their differences with respect to the unblended case in Figure 2.2 (upper-left section). The noise that is present in Figures (c) and (d) can be attributed to the imaging response of the blending noise.

the imaging process has to be carried out twice, with and without point scatterers being present. Their difference section contains the PSFs. In this way, illumination by multiples is included while still ending up with PSFs only.

The design of an acquisition geometry is always a compromise, being limited by the acquisition budget and physical constraints. Therefore, it must be evaluated beforehand to check whether or not the proposed seismic experimental set-up of acquisition and (pre)processing meets the pre-defined quality criteria. For example, to achieve the objective, a full-wavefield imaging method may be necessary. On the other hand, if such method is not available, the acquisition geometry has to be modified, probably by adding more sources and/or receivers in order to achieve the required target illumination. The use of blended acquisition could also be evaluated at this stage.

BIBLIOGRAPHY

[1] C. J. Beasley, R. E. Chambers, and Z. Jiang. "A new look at simultaneous sources". *SEG Technical Program Expanded Abstracts 1998*. 1998.

[2] A. J. Berkhout. *Seismic migration, imaging of acoustic energy by wave field extrapolation, A. theoretical aspects*. Elsevier, 1982.

[3] A. J. Berkhout. *Seismic resolution: a quantitative analysis of resolving power of acoustical echo techniques*. London – Amsterdam: Geophysical Press, 1984.

[4] A. J. Berkhout, G. Blacquière, and E. Verschuur. "From simultaneous shooting to blended acquisition". *SEG Technical Program Expanded Abstracts 2008*. 2008.

[5] A. J. Berkhout, L. Ongkiehong, A. W. F. Volker, and G. Blacquière. "Comprehensive assessment of seismic acquisition geometries by focal beams—Part I: Theoretical considerations". *Geophysics* 66 (2001), pp. 911–917.

[6] A. Berkhout. "Review Paper: An outlook on the future of seismic imaging, Part I: forward and reverse modelling". *Geophysical Prospecting* 62 (2014), pp. 911–930.

[7] G. Beylkin. "Imaging of discontinuities in the inverse scattering problem by inversion of a causal generalized Radon transform". *Journal of Mathematical Physics* 26 (1985), pp. 99–108.

[8] J. Bouska. "Distance separated simultaneous sweeping, for fast, clean, vibroseis acquisition". *Geophysical Prospecting* 58 (2010), pp. 123–153.

[9] M. P. Brown and A. Guitton. "Least-squares joint imaging of multiples and primaries". *Geophysics* 70 (2005), S79–S89.

[10] M. Davydenko. "Full wavefield migration: Seismic imaging using multiple scattering effects". PhD Thesis. Delft University of Technology, 2016.

[11] A. Kumar. "3-D seismic acquisition geometry design and analysis". PhD Thesis. Technische Universiteit Delft, 2015.

[12] I. Lecomte. "Resolution and illumination analyses in PSDM: A ray-based approach". *The Leading Edge* 27 (2008), pp. 650–663.

[13] A. Mahdad, P. Doulgeris, and G. Blacquiere. "Separation of blended data by iterative estimation and subtraction of blending interference noise". *Geophysics* 76 (2011), Q9–Q17.

[14] A. E. Malcolm, B. Ursin, and M. V. de Hoop. "Seismic imaging and illumination with internal multiples". *Geophysical Journal International* 176 (2009), pp. 847–864.

[15] B. Revelo-Obando and G. Blacquière. "Acquisition geometry analysis with point-spread functions". *Geophysical Prospecting* 69 (2021), pp. 1606–1624.

[16] S. Singh, R. Snieder, J. Behura, J. van der Neut, K. Wapenaar, and E. Slob. "Marchenko imaging: Imaging with primaries, internal multiples, and free-surface multiples". *Geophysics* 80 (2015), S165–S174.

[17] S. Singh, R. Snieder, J. van der Neut, J. Thorbecke, E. Slob, and K. Wapenaar. "Accounting for free-surface multiples in Marchenko imaging". *Geophysics* 82 (2017), R19–R30.

[18] X. Staal. "Combined imaging and velocity estimation by Joint Migration Inversion". PhD thesis. Technische Universiteit Delft, 2015.

[19] N. Tu and F. J. Herrmann. "Fast imaging with surface-related multiples by sparse inversion". *Geophysical Journal International* 201 (2015), pp. 304–317.

[20] E. J. van Veldhuizen, G Blacquière, and A. J. Berkhout. "Acquisition geometry analysis in complex 3D media". *Geophysics* 73 (2008), Q43–Q58.

[21] G. J. O. Vermeer. *3D Seismic Survey Design*. 2nd ed. Geophysical References Series. Society of Exploration Geophysicists, 2012.

[22] G. J. O. Vermeer. "Factors affecting spatial resolution". *Geophysics* 64 (1999), pp. 942–953.

[23] D. Von Seggern. "Spatial resolution of acoustic imaging with the Born approximation". *Geophysics* 56 (1991), pp. 1185–1202.

[24] K. Wapenaar, J. Thorbecke, J. van der Neut, F. Broggini, E. Slob, and R. Snieder. "Marchenko imaging". *Geophysics* 79 (2014), WA39–WA57.

[25] D. Zhang and G. T. Schuster. "Least-squares reverse time migration of multiples". *Geophysics* 79 (2014), S11–S21.

3

SEISMIC ACQUISITION DESIGN BASED ON FULL-WAVEFIELD MIGRATION

The ultimate goal in survey design is to obtain the acquisition parameters that enable acquiring the most affordable data that fulfill certain image quality requirements. We propose a method that allows optimization of the receiver geometry for a fixed source distribution. The former is parameterized with a receiver density function that determines the number of receivers per unit area. We optimize this receiver density function through an iterative gradient descent scheme that minimizes the difference between the image obtained with the current acquisition geometry and a reference image. The reference image is obtained from prior subsurface information that is assumed to be available. We tested the method with different subsurface models. The results show that the acquisition geometry is optimized according to the complexity of each subsurface model. The receivers are moved towards the areas where more data is needed for obtaining better imaging.

A part of this chapter was published as Revelo-Obando and Blacquière (2023) in *Geophysics*. An extension and several modifications have been applied to the text for the sake of consistency in the thesis.

3.1. INTRODUCTION

The goal of seismic survey design is to find the acquisition parameters that - after a certain data-processing sequence - lead to a certain image quality, while fulfilling economic, time and environmental constraints.

In traditional acquisition geometries, seismic sources and receivers are laid out in (straight) lines. The spacing between stations within a line and the separation between lines is chosen to achieve certain common midpoint (CMP) properties: resolution, offset distribution and trace multiplicity (Vermeer, 2012). Ideally, without the presence of noise, the expected resolution of a seismic image can be computed through the seismic velocities in the subsurface and the bandwidth of seismic data. However, in real-world acquisition, often a higher trace multiplicity is required to obtain an adequate signal-to-noise ratio (SNR).

The source and receiver sampling of an unaliased acquisition geometry would satisfy the Nyquist-Shannon criterion (at least two samples per smallest wavelength, which may be related to a noise signal). However, in practice this is not feasible due to associated acquisition and processing costs. In marine acquisition for example, acquisition with ocean bottom nodes has gained popularity due to the flexibility of the source location with respect to the location of the receivers. This provides denser source sampling, longer offsets and better angle distribution than in the case of streamer acquisition when a single vessel is used (Regone, 2006), for example. It also provides a better coupling with the seafloor and vector fidelity (Alerini et al., 2009). However, this type of receivers has a high cost compared to marine streamer cables. For this reason, their optimal positioning is critical for reducing costs while obtaining a high quality image of the target zone.

In addition to the limitations of a survey design arising due to the presence of noise, a complex subsurface may hinder the illumination-and-detection properties of the survey. For example salt structures or karst topographies, can reduce the illumination of underlying targets of economical interest (Muerdter and Ratcliff, 2001). It means that the expected resolution of the survey design is affected by the complexity of the subsurface: the image of the target zone can be deficient while other zones of less interest get a better image quality.

In areas where seismic exploration has been carried out previously, legacy data as well as corresponding subsurface models are available. These can be used in the design of a future survey to take the particular subsurface properties into consideration, such as the major, multiple-generating reflectors. This has been undertaken through the use of modeling and imaging studies, where an initial geometry is manually updated to achieve better illumination in the target zones (Singh et al., 2016; Theriot et al., 2014). However, in this type of experimental survey design, the theory is not directly linked with the outcome of the experiment (Maurer et al., 2010). New approaches in survey design make use of deep learning to optimize survey design parameters for blended acquisition (Nakayama et al., 2019). Here the computational cost of modeling multiple geometries is avoided by selecting the most suitable with the aid of neural networks.

In some complex subsurface scenarios, multiple reflections could play an important role in the acquisition design depending on whether they are considered as signal or as noise. In the first case, full-wavefield imaging algorithms can make use of multiple reflections for the reflectivity estimation process as the latter can provide illumination

that is supplementary to the illumination by primary reflections. In the second case, the multiples must be eliminated prior to imaging.

Methods such as the focal beam analysis (Berkhout et al., 2001; Volker et al., 2001) can predict the resolution and illumination properties of an acquisition geometry for a single point in a complex subsurface. An extension is proposed by Kumar et al. (2016) to include multiple reflections into the analysis, and Wu et al. (2022) use this method as the base for an optimization algorithm that improves the angle coverage and resolution at one target point in the subsurface.

We developed an iterative algorithm that optimizes the acquisition geometry in a survey area for which some prior knowledge is available and that assumes Full-Wavefield Migration (FWM, Davydenko and Verschuur, 2017) to be used as the processing algorithm. We choose FWM as it makes use of multiple reflections for imaging, potentially increasing the subsurface illumination compared to primaries-only migration algorithms (Davydenko and Verschuur, 2018; Revelo-Obando and Blacquière, 2021). This could relax spatial sampling requirements, which would save costs in sparse acquisition scenarios such as ocean-bottom node acquisition. In this chapter we limit ourselves to computing the locations of a fixed number of receivers. This means that we aim to distribute the available receivers optimally in a spatial sense.

The receiver geometry is parameterized through a receiver density function that determines the number of receivers per unit area. The quality of an acquisition geometry is evaluated through a least-squares target function that compares the image obtained after each iteration with a reference image. If the quality criterion is not satisfied, the receiver density function is updated through a gradient descent scheme and the iterative process continues.

This chapter is divided as follows: first, the framework of survey design and FWM is described. Then the receiver geometry parameterization and the target function are introduced. Subsequently, the optimization algorithm is discussed, including the gradient descent scheme for the receiver density function optimization. Then three examples are presented to demonstrate the performance of the algorithm. The chapter ends with a discussion and conclusions.

3.2. THEORY

3.2.1. FRAMEWORK OF SURVEY DESIGN

We describe 3D seismic data with the matrix notation proposed by Berkhout (1982). For one frequency component, a seismic dataset can be formulated as:

$$\mathbf{P}^{-}(z_d, z_s) = \mathbf{D}(z_d)\mathbf{X}^{-}(z_d, z_s)\mathbf{S}^{+}(z_s), \tag{3.1}$$

where matrix $\mathbf{P}^{-}$ represents the upgoing acoustic pressure wavefields recorded by receivers at depth level z_d, generated by sources at depth level z_s. Each matrix element P^{-}_{jk} is a complex number that contains the amplitude and phase information of the trace recorded by receiver j due to source k for the frequency component under consideration. Matrices $\mathbf{S}^{+}$ and $\mathbf{D}$ are the source and receiver matrix respectively. Together they describe the survey geometry as well as the source and receiver properties (directivity, sensitivity, spectral properties, etc.). Matrix $\mathbf{X}^{-}$ represents the transfer operator of the

subsurface, and contains all propagation and (multiple-)reflection effects. It can be considered to be the ideal seismic data set, i.e., with densely sampled carpet shooting and carpet detection with unit sources and unit detectors, respectively. The + and - superscripts indicate the down- and upgoing wavefield direction, respectively. As mentioned, in this research we assume that $\mathbf{X}^-(z_d, z_s)$ can be modeled, e.g., using a subsurface model based on prior knowledge such as obtained from legacy data.

If sources and detectors are both located at the surface z_0, i.e., $z_s = z_d = z_0$, equation 3.1 becomes:

$$\mathbf{P}^-(z_0, z_0) = \mathbf{D}(z_0)\mathbf{X}^-(z_0, z_0)\mathbf{S}^+(z_0). \tag{3.2}$$

For the case that the sources are ideal and perfectly sampled, $\mathbf{S}^+(z_0)$ equals the identity matrix $\mathbf{I}$ and equation 3.2 becomes:

$$\mathbf{P}^-(z_0, z_0) = \mathbf{D}(z_0)\mathbf{X}^-(z_0, z_0). \tag{3.3}$$

The modeling of $\mathbf{X}^-(z_0, z_0)$ could be performed with any modeling engine, e.g. with finite-difference modeling. Our modeling method is Full-wavefield modeling (FWMod) (Berkhout, 2014b). It is recursive in depth as well as iterative. It is also the modeling engine used in FWM, described in the next section. In this way of modeling, the up- and down-going wavefields $\mathbf{X}_i^-(z_n, z_0)$ and $\mathbf{X}_i^+(z_n, z_0)$ at depth level z_n are computed for all iterations i. Here, n ranges from 0 to N, with z_N being the maximum depth of interest. These iterations are called round trips, and each round trip adds one additional order of multiple reflections. This means that the primary reflections are obtained in the first round trip, the primaries plus the first order multiples in the second, and so on. One round trip consists of a downgoing step ($n = 1, 2, ..., N$) and an upgoing step ($N = N-1, N-2, ..., 0$) which can be formulated as:

$$\mathbf{X}_i^+(z_n, z_0) = \sum_{m=1}^{n-1} \mathbf{U}^+(z_n, z_m)\mathbf{R}^\cap(z_m)\mathbf{X}_{i-1}^-(z_m, z_0) + \mathbf{U}^+(z_n, z_0), \tag{3.4a}$$

$$\mathbf{X}_i^-(z_n, z_0) = \sum_{m=n+1}^{N} \mathbf{U}^-(z_n, z_m)\mathbf{R}^\cup(z_m)\mathbf{X}_i^+(z_m, z_0). \tag{3.4b}$$

This scheme is equivalent to a Bremmer series expansion. See Davydenko (2016) for details. Matrices $\mathbf{R}^\cap(z_m)$ and $\mathbf{R}^\cup(z_m)$ are the up-down and down-up, angle-dependent reflection operators at depth level z_m. Operator $\mathbf{U}^+(z_n, z_m)$ includes the propagation and transmission effects in the downgoing direction from depth level z_m to depth level z_n, and so does operator $\mathbf{U}^-(z_n, z_m)$ for wavefields propagating in the upward direction. They are computed as follows:

$$\mathbf{U}^+(z_n, z_m) = \left[\prod_{k=n-1}^{m+1} \mathbf{W}^+(z_{k+1}, z_k)\mathbf{T}^+(z_k)\right]\mathbf{W}^+(z_{m+1}, z_m), \tag{3.5a}$$

$$\mathbf{U}^-(z_n, z_m) = \left[\prod_{k=n+1}^{m-1} \mathbf{W}^-(z_{k-1}, z_k)\mathbf{T}^-(z_k)\right]\mathbf{W}^-(z_{m-1}, z_m), \tag{3.5b}$$

where $\mathbf{W}^+(z_{k+1}, z_k)$ is the downward wavefield propagation operator from depth level z_k to depth level z_{k+1}; $\mathbf{W}^-(z_{k-1}, z_k)$ is the upward wavefield propagation operator from

depth level z_k to depth level z_{k-1}; $\mathbf{T}^+(z_k)$ is the transmission operator of the downgoing wavefield crossing depth level z_k from above; $\mathbf{T}^-(z_k)$ is the transmission operator of the upgoing wavefield crossing depth level z_k from below. The use of this type of modeling allows to specify reflectivity and transmissivity independently from propagation velocity. The output of this scheme, after L iterations, is the modeled, perfectly sampled data, $\mathbf{X}_L^-(z_0,z_0) = \mathbf{X}^-(z_0,z_0)$, which can be turned into more realistic data via multiplication with $\mathbf{D}(z_0)$, see equation 3.3 (still under the assumption of a perfect source distribution).

In the acoustic case, the transmission operators can be described in terms of the reflectivity:

$$\mathbf{T}^+(z_k) = \mathbf{I} + \mathbf{R}^\cup(z_k), \tag{3.6a}$$
$$\mathbf{T}^-(z_k) = \mathbf{I} + \mathbf{R}^\cap(z_k). \tag{3.6b}$$

This means that the acoustic assumption reduces the number of independent reflection and transmission matrices from four to two. In addition, if reflection and transmission are assumed to be angle-independent, these matrices become diagonal matrices and $\mathbf{R}^\cup = -\mathbf{R}^\cap$, even further reducing the number of parameters.

3.2.2. REFLECTIVITY ESTIMATION WITH FWM

In seismic migration, the objective is to estimate the reflectivity of the subsurface given the seismic data and a propagation velocity model. The reflectivity matrices $\mathbf{R}^\cup$ and $\mathbf{R}^\cap$, estimated by FWM (Berkhout, 2014a; Davydenko and Verschuur, 2017), are obtained through an iterative process where the target function $J_{\Delta,i}$ at iteration i is minimized. Its expression is:

$$J_{\Delta,i}(z_0,z_0) = \sum_\omega \mathrm{Tr}\left(\Delta\mathbf{P}_i(z_0,z_0)\Delta\mathbf{P}_i(z_0,z_0)^H\right), \tag{3.7}$$

where $\Delta\mathbf{P}_i(z_0,z_0)$ represents the data residual at iteration i. It is defined as follows:

$$\Delta\mathbf{P}_i(z_0,z_0) = \mathbf{D}_i(z_0)\Delta\mathbf{X}_i^-(z_0,z_0), \text{with} \tag{3.8a}$$
$$\Delta\mathbf{X}_i^-(z_0,z_0) = \mathbf{X}^-(z_0,z_0) - \mathbf{X}_i^-(z_0,z_0), \tag{3.8b}$$

where, as we shall see later, receiver matrix $\mathbf{D}_i(z_0)$ depends on iteration i. In FWM, the reflectivity operators are updated at each iteration through an iterative gradient descent scheme. Therefore, update directions $\delta\mathbf{R}_i^\cup$ and $\delta\mathbf{R}_i^\cap$ are needed. These are found by moving along the direction of steepest descent, which is the direction along which $J_{\Delta,i}$ is minimized. Therefore, the reflectivity update directions are the derivatives of $J_{\Delta,i}$ with respect to $\mathbf{R}^\cup$ and $\mathbf{R}^\cap$ respectively:

$$\delta\mathbf{R}_i^\cup(z_n) = |f|^2\left[\mathbf{U}_i^-(z_0,z_n)\right]^H\Delta\mathbf{P}_i(z_0,z_0)\left[\mathbf{X}_i^+(z_n,z_0)\right]^H, \tag{3.9a}$$
$$\delta\mathbf{R}_i^\cap(z_n) = |f|^2\left[\mathbf{U}_i^\cup(z_0,z_n)\right]^H\Delta\mathbf{P}_i(z_0,z_0)\left[\mathbf{X}_{i-1}^-(z_n,z_0)\right]^H, \tag{3.9b}$$

for n=1:N, where $f = f(\omega)$ is a weighting factor that partially compensates for the wavelet signature on the data. The full-wavefield propagation operator $\mathbf{U}_i^\cup(z_0,z_n)$ is defined as:

$$\mathbf{U}_i^\cup(z_0,z_n) = \sum_{m=n+1}^{N}\mathbf{U}_i^-(z_0,z_m)\mathbf{R}_i^\cup(z_m)\mathbf{U}_i^+(z_m,z_n). \tag{3.10}$$

For practical reasons, we will now introduce two assumptions that simplify our theory and the subsequent computer implementation. First, rather than considering the reflectivity to be angle dependent, we continue with the angle independent reflection coefficient for which we take the angle-averaged value. For this case, the reflectivity update direction at each depth level is computed according to:

$$\delta\overline{\mathbf{R}}_i^{\cup}(z_n) = \text{diag}\left\{\sum_{\omega}\delta\mathbf{R}_i^{\cup}(z_n)\right\}, \tag{3.11a}$$

$$\delta\overline{\mathbf{R}}_i^{\cap}(z_n) = \text{diag}\left\{\sum_{\omega}\delta\mathbf{R}_i^{\cap}(z_n)\right\}, \tag{3.11b}$$

where diag{$\mathbf{M}$} clears all off-diagonal elements of matrix $\mathbf{M}$ and where the overbar indicates the angle-independent reflectivity approximation. The summation over ω, corresponding to an inverse FFT from frequency to time for $t = 0$ s only, is applied to implement the imaging principle. Second, in the acoustic case the down-up and up-down reflection coefficients can be assumed to be each other's opposite (small-angle approximation) (Wapenaar and Berkhout, 1989). Introducing this assumption means that we may combine the two for the computation of the update direction. The joint reflectivity update direction is optimized for preconditioning as follows:

$$\delta\overline{\mathbf{R}}_i(z_n) = [\mathbf{H}_i(x,z_n)]^{-1}\left[\delta\overline{\mathbf{R}}_i^{\cup}(z_n) - \delta\overline{\mathbf{R}}_i^{\cap}(z_n)\right], \tag{3.12}$$

where the diagonal matrix $\mathbf{H}_i$ is an approximation of the Hessian that acts as a spatially varying scaling of the gradient (Staal, 2015). Its elements are defined as:

$$\begin{aligned} H_{kk}(z_n) = &\sum_{\omega}\|\mathbf{U}^{-}(x,z_0;x_k,z_n)\|^2\left|X_i^{+}(x_k,z_n)\right|^2 \\ &+\sum_{\omega}\left\|\mathbf{U}^{\cup}(x,z_0;x_k,z_n)\right\|^2\left|X_{i-1}^{-}(x_k,z_n)\right|^2, \end{aligned} \tag{3.13}$$

The step length α_i for the reflectivity update is computed as follows:

$$\alpha_i = \frac{\text{Tr}[\Delta\mathbf{P}_i^H\Delta\mathbf{P}_r(\delta\overline{\mathbf{R}}_i) + \Delta\mathbf{P}_r^H(\delta\overline{\mathbf{R}}_i)\Delta\mathbf{P}_i]}{\text{Tr}\left[\Delta\mathbf{P}_r^H(\delta\overline{\mathbf{R}}_i)\Delta\mathbf{P}_r(\delta\overline{\mathbf{R}}_i)\right]}, \tag{3.14}$$

where $\Delta\mathbf{P}_r(\delta\overline{\mathbf{R}}_i)$ is the linearized wavefield perturbation associated to the update direction $\delta\overline{\mathbf{R}}_i$. It is defined as:

$$\begin{aligned} \Delta\mathbf{P}_r(\delta\overline{\mathbf{R}}_i) = \sum_n\Big\{&\mathbf{U}_i^{-}(z_0,z_n)\delta\overline{\mathbf{R}}_i(z_n)\mathbf{X}_i^{+}(z_n,z_0) \\ &+\mathbf{U}_i^{\cup}(z_0,z_n)\delta\overline{\mathbf{R}}_i(z_n)\mathbf{X}_{i-1}^{-}(z_n,z_0)\Big\}. \end{aligned} \tag{3.15}$$

Finally, the reflectivity, for which we assume $\overline{\mathbf{R}}^{\cup}(z_n) = -\overline{\mathbf{R}}^{\cap}(z_n) = \overline{\mathbf{R}}(z_n)$, is updated according to:

$$\overline{\mathbf{R}}_{i+1}(z_n) = \overline{\mathbf{R}}_i(z_n) + \alpha_i\delta\overline{\mathbf{R}}_i(z_n). \tag{3.16}$$

In the remainder of this chapter we will omit the overbar for notational simplicity. Therefore, matrix $\mathbf{R}$ will represent the angle-independent reflectivity approximation.

3.3. METHOD

As mentioned before, we assume that we have fully-sampled, ideal data $\mathbf{X}^-(z_0, z_0)$ available. The aim is to design the optimal receiver matrix $\mathbf{D}$ with the positions of n_d receivers, (located on a predefined grid) within a certain aperture, which gives the practical data $\mathbf{P}^-(z_0, z_0) = \mathbf{D}(z_0)\mathbf{X}^-(z_0, z_0)$. Imaging of $\mathbf{P}^-(z_0, z_0)$ then leads to the optimum reflectivity estimate.

In our iterative algorithm we aim at improving the reflectivity estimate at each iteration by updating the receiver matrix, i.e., the imaging process and the acquisition geometry estimation process go hand in hand. At the end of the process, we have both the optimum reflectivity estimate and the corresponding optimum acquisition geometry.

Assuming ideal point receivers, i.e., with a flat, unit sensitivity, for each frequency component matrix $\mathbf{D}(z_0)$ is a diagonal matrix whose elements are either ones or zeros, indicating the presence or absence of a receiver at a grid position, respectively. Therefore, updating the operator implies adding or removing receivers, i.e. changing ones by zeros and vice versa, while keeping n_d constant. Since it is difficult to formulate this in terms of an update direction and a step length, an intermediate parameterization is required.

3.3.1. PARAMETERIZATION

We parametrize the receiver geometry with a receiver density function $\mathbf{\Phi}$ (Wu et al., 2022). It determines the number of receivers per unit area at each grid point of the acquisition surface. This function is then translated into matrix $\mathbf{D}$ through a transformation g:

$$\mathbf{D}_i = g(\mathbf{\Phi}_i). \tag{3.17}$$

In equation 3.17 we have added the subscript i as in our iterative scheme the receiver density and the receiver matrix will be updated at every iteration. Function $\mathbf{\Phi}_i$ is implemented as a real-valued, diagonal matrix with the same dimensions as matrix $\mathbf{D}_i$. The values of the diagonal elements, between 0 and 1, correspond to the receiver density at the corresponding spatial location. Note that an alternative way of interpreting $\mathbf{\Phi}_i$ is that it contains receivers with a sensitivity anywhere between 0 and 1. In practice - even though such receivers could be produced - this would be inefficient. Therefore, it is desired to only deploy receivers that have maximum sensitivity, which in our case corresponds to a sensitivity of 1. To translate the receiver density in the locations of such receivers, we use a weighted Voronoi Stippling algorithm (Secord, 2002). First, n_d sampling locations are chosen from the receiver density through a simple rejection sampling algorithm. In this algorithm, a random location is chosen and its corresponding receiver density value is compared to a random value taken from a uniform distribution. If the receiver density is higher than the random value, that location is chosen. This procedure is repeated until n_d locations are selected. Therefore, the higher the value of an element of $\mathbf{\Phi}_i$, the higher the possibility of a receiver being put at that location. Next, after choosing the locations, these are redistributed through Lloyd's algorithm (Lloyd, 1982). This algorithm computes the Voronoi diagram of a set of points, in our case the receiver locations, and shifts their locations to the centroids of the computed Voronoi cells. Finally, the locations are translated into the receiver matrix $\mathbf{D}_i$ by placing a '1' at the corresponding

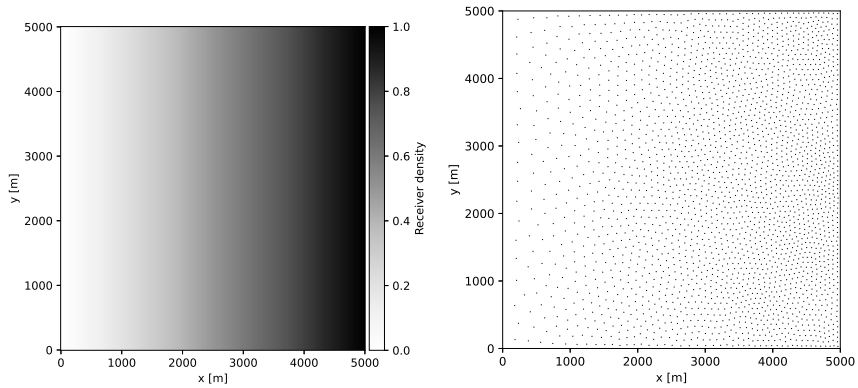

Figure 3.1: (a) Receiver density. Linear increase in the x-direction. (b) Corresponding receiver geometry created through the transformation g for $n_d = 2500$. More receivers are located in the right-hand side where the density is higher.

grid location. This is done by approximating the locations found through the Lloyd's algorithm to the closest grid position. Figure 3.1 shows an example of a linearly increasing receiver density $\mathbf{\Phi}_i$ and the corresponding receiver matrix $\mathbf{D}_i$.

In the remainder of this chapter, we will use $\mathbf{\Phi}_i$ and $\mathbf{D}_i$ interchangeably. The former when a continuous variable is needed, and the latter when a discrete variable is required, e.g., for data sampling. It is important to note that the transformation g is non-deterministic. This means that for a single receiver density matrix $\mathbf{\Phi}_i$, multiple realizations of matrix $\mathbf{D}_i$ can be obtained. However, the Voronoi iterations tend to reduce the differences between these realizations.

3.3.2. TARGET FUNCTION

Starting with an 'empty' initial reflectivity model $\mathbf{R}_i(z_n) = 0$ for $i = 0$, the first step in our algorithm is to estimate a reflectivity update $\mathbf{R}_{i+1}(z_n)$ with one FWM iteration, using an arbitrary initial receiver geometry $\mathbf{D}_i$ for $i = 0$ and with n_d receivers. The receiver positions of such a geometry could, for instance, be equidistant. Subsequently, we evaluate the quality of the obtained image. We propose a least-squares target function J_R defined as follows:

$$J_{R,i} = \sum_n \|\Delta\mathbf{R}_i(z_n)\|_F^2, \tag{3.18a}$$

$$\Delta\mathbf{R}_i(z_n) = \mathbf{R}(z_n) - \mathbf{R}_{i+1}(z_n), \tag{3.18b}$$

where matrix $\mathbf{R}(z_n)$ represents a reference image at z_n and the subscript F denotes the Frobenius norm. In our case it is the best possible migration result obtained with a full receiver sampling, i.e., satisfying the Nyquist criterion. Matrix $\mathbf{R}_{i+1}(z_n)$ is the reflectivity update obtained by FWM at iteration i (see equation 3.16). The residual $\Delta\mathbf{R}_i$ is the difference between the reference image and the estimated one at iteration i. If desired, $\Delta\mathbf{R}_i(z_n)$ could be multiplied with a spatially-varying weighting function to give priority

to certain target zones. A threshold ϵ can be established for $J_{R,i}$ as a quality criterion: if $J_{R,i} < \epsilon$, the quality criterion has been met and the iterative process can stop. If the quality criterion is easily reached, e.g., already within a few iterations, one may consider reducing n_d. This could result in a cheaper acquisition design that still fulfills the desired quality requirements. If the quality criterion has not been met, apparently the receiver geometry needs to be further improved (updated) in the subsequent iteration(s), as will be discussed next. In the case that the quality criterion can not be reached, n_d and/or ϵ could be increased, but we stop when the predefined maximum number of iterations `nit` has been reached.

3.3.3. GRADIENT DESCENT SCHEME

We propose to update the receiver density $\mathbf{\Phi}$ through an iterative gradient descent scheme:

$$\mathbf{\Phi}_{i+1} = \mathbf{\Phi}_i + \beta_i \delta\mathbf{\Phi}_i, \tag{3.19}$$

where $\mathbf{\Phi}_i$ is the current-iteration receiver density, $\delta\mathbf{\Phi}_i$ is the update direction, β_i is the step length, and $\mathbf{\Phi}_{i+1}$ is the updated, next-iteration receiver density. As mentioned, $\mathbf{\Phi}_{i+1}$ is translated into receiver matrix $\mathbf{D}_{i+1}$ through transformation g.

3.3.4. UPDATE DIRECTION AND STEP LENGTH

The update direction for the receiver density is given by the (conjugate) gradient of target function $J_{R,i}$ (equation 3.18a) with respect to receiver density $\mathbf{\Phi}$. Hence, the derivative to be computed is:

$$\frac{\partial J_{R,i}}{\partial \mathbf{\Phi}} = \frac{\partial}{\partial \mathbf{\Phi}} \left[\sum_n \|\Delta\mathbf{R}_i(z_n)\|_F^2 \right]. \tag{3.20}$$

As derived in Appendix 3.A, this derivative can be expressed as:

$$\frac{\partial J_{R,i}}{\partial \mathbf{\Phi}} = -2\alpha_i \sum_n \sum_\omega |f|^2 \left[\mathbf{H}_i(x, z_n)\right]^{-1} \Delta\mathbf{P}_r(\Delta\mathbf{R}_i(z_n))[\Delta\mathbf{X}_i^-(z_0, z_0)]^H. \tag{3.21}$$

This equation contains the correlation between the data residual $\Delta\mathbf{X}_i^-$ and the seismic data $\Delta\mathbf{P}_r$ modeled from the residual image $\Delta\mathbf{R}_i$. Therefore, it can be interpreted as a mapping from the model update to the data space, at the sampling locations where more data is needed.

The update direction is given by the negative conjugate of equation 3.21:

$$\delta\mathbf{\Phi}_i = -\frac{\partial J_{R,i}^*}{\partial \mathbf{\Phi}}, \tag{3.22}$$

and the step length is given by (see Appendix 3.B):

$$\beta_i = \frac{(\delta\Phi_i)^H \delta\Phi_i}{\text{diag}\left\{-2\alpha_i \sum_n \sum_\omega |f|^2 \left[\mathbf{H}_i(x, z_n)\right]^{-1} \Delta\mathbf{P}_r(\mathbf{R}_\phi(z_n))[\Delta\mathbf{X}_i^-(z_0, z_0)]^H\right\}^H \delta\Phi_i}, \tag{3.23}$$

where $\mathbf{R}_\phi(z_n)$ is an image associated with the receiver density update direction and $\Delta\mathbf{P}_r(\mathbf{R}_\phi(z_n))$ is the corresponding wavefield perturbation, similar as with equation 3.15.

3.3.5. ALGORITHM

The iterative process to optimize the receiver geometry is summarized in Algorithm 1.

Algorithm 1 Acquisition geometry optimization algorithm

Require: $\mathbf{X}^-(z_0, z_0), \mathbf{R}, \mathbf{D}_0$

for $0 \leq i \leq$ `nit` **do** ▷ Acquisition geometry with `nit` updates
  Compute wavefields $\mathbf{X}_i^+, \mathbf{X}_i^-$
  $\Delta\mathbf{P}_i = \mathbf{D}_i \Delta\mathbf{X}_i^-$ ▷ Apply receiver geometry, compute data residual
  $\mathbf{R}_{i+1} = \mathbf{R}_i + \alpha_i \delta\mathbf{R}_i$ ▷ Update reflectivity
  if $J_{R,i} < \epsilon$ **then** ▷ Evaluate image quality criterion
    Finish
  end if
  $\mathbf{\Phi}_{i+1} = \mathbf{\Phi}_i + \beta_i \delta\mathbf{\Phi}_i$ ▷ Update receiver density
  $\mathbf{D}_{i+1} = g(\mathbf{\Phi}_{i+1})$ ▷ Update receiver geometry
end for
Change number of receivers

We tested our newly developed algorithm for a number of different subsurface models. From these, the reference datasets $\mathbf{X}^-(z_0, z_0)$ were modeled with FWMod, using a Ricker wavelet with a central frequency of 20 Hz and 30 iterations. The corresponding reference reflectivity models ($\mathbf{R}$) were obtained through inversion with FWM using a full receiver sampling (ideal receiver geometry). As mentioned, the source geometry was kept constant for each experiment. In all examples the geometry has a fixed receiver spread.

The first study uses a model that contains three horizontal layers (Figure 3.2). The source geometry consists of 14 sources uniformly distributed every 180 m. As the model is laterally homogeneous, the optimal receiver geometry is expected to be spatially uniform. To test the algorithm, we start the optimization process with the initial geometry shown in Figure 3.3a. It consists on $n_d = 41$ receivers, all being located in the left hand side of the model, i.e., far from the expected optimal geometry. After 30 iterations we obtain the receiver density shown in Figure 3.3c and its corresponding receiver geometry (Figure 3.3d).

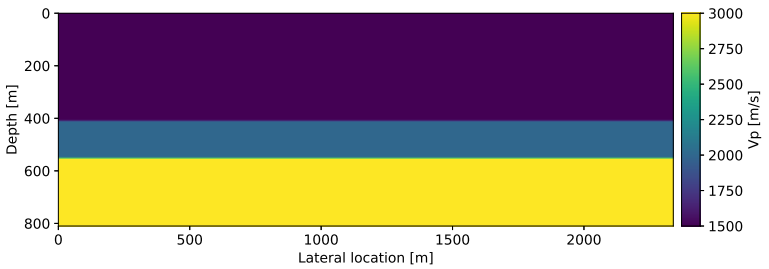

Figure 3.2: P-wave velocity model with three horizontal layers. The velocities of the layers from top to bottom are $Vp = 1500$ m/s, 2200 m/s and 3000 m/s.

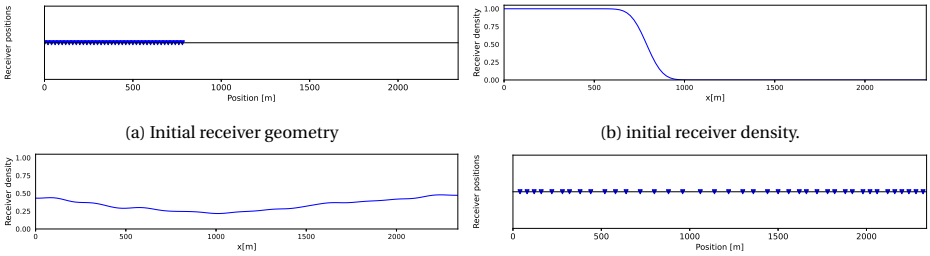

(a) Initial receiver geometry

(b) initial receiver density.

(c) optimized receiver density

(d) optimized receiver geometry.

Figure 3.3: Geometry optimization for the model in Figure 3.2. The receivers are located at the surface $z = 0$ m.

The optimized receiver geometry shown in Figure 3.3d shows that the receivers are placed almost uniformly along the acquisition surface. However, the receiver density is clearly somewhat higher at the edges of the aperture than in the middle. The reason for this will be discussed later. To test the consistency of the algorithm, we repeat the experiment with a different starting geometry. The same number of receivers are now positioned at the center of the model (Figure 3.4a) and the algorithm is run again for 30 iterations. The optimized receiver density and corresponding geometry are shown in Figures 3.4c and 3.4d.

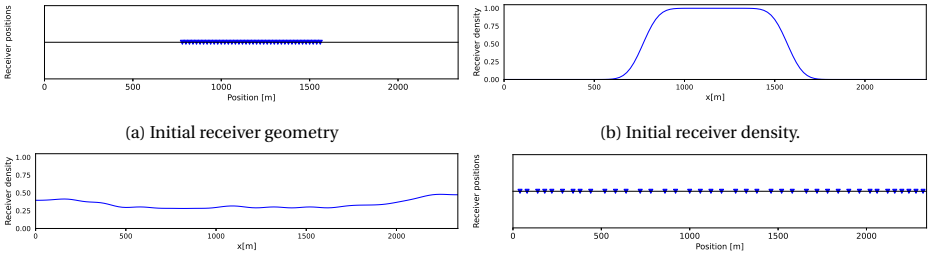

(a) Initial receiver geometry

(b) Initial receiver density.

(c) Optimized receiver density

(d) Optimized receiver geometry.

Figure 3.4: Geometry optimization for the model in Figure 3.2. The receivers are located at the surface $z = 0$ m.

The optimized receiver geometry shown in Figure 3.4d closely resembles the one obtained in the previous experiment (Figure 3.3d) despite the completely different initial geometries. This result confirms the consistency of the algorithm and its robustness to the initial geometry. As in the previous example, the optimized receiver density is slightly higher at the edges than at the center. This means that the corresponding receiver geometries are not completely uniform. We assume that this is an edge effect related to the finite aperture: the shot records near the edges ('half hyperbolas') contain less signal energy than the ones in the middle ('full hyperbolas'). It means that the receiver geometry compensates for this energy difference. Additionally, it can be observed that some undulations are present in the optimized received density (Figures 3.3c and 3.4c). This is the result of the transformation, at each iteration, from receiver density to acquisition geometry.

For the second study case we use the models shown in Figure 3.5. They contain flat layers with a high-velocity perturbation embedded in the first layer. The velocity of the perturbation is 2500 m/s for the first model (Figure 3.5a) and 4000 m/s for the second (Figure 3.5b). The sources are uniformly distributed every 100 m along the surface. The initial receiver geometry consists of $n_d = 41$ receivers located uniformly along the acquisition surface (Figure 3.6a). First, for the model in Figure 3.5a, we run the optimization algorithm for 30 iterations and obtain the receiver density shown in Figure 3.6c and the corresponding receiver geometry (Figure 3.6d).

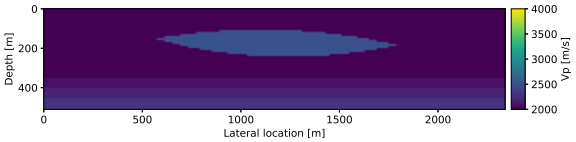

(a) Model A: perturbation with v = 2500 m/s.

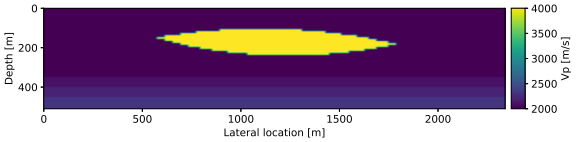

(b) Model B: perturbation with v = 4000 m/s.

Figure 3.5: Horizontally layered P-wave velocity models with high-velocity perturbation embedded in the first layer.

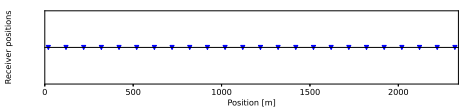

(a) Initial receiver geometry

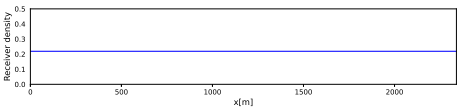

(b) Initial receiver density.

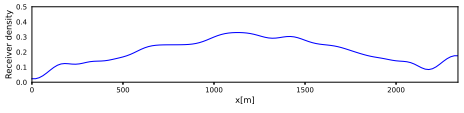

(c) Optimized receiver density

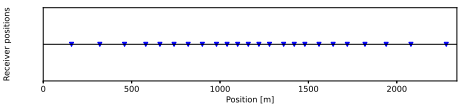

(d) Optimized receiver geometry.

Figure 3.6: Initial and optimized receiver geometries for the model in Figure 3.5a. The receivers are located at the surface $z = 0$ m. The optimized geometry shows that more receivers are needed above the high-velocity perturbation in order to obtain a better image.

The result of the optimization shows that the receiver density (Figure 3.6c) has higher values in the central part, meaning that the receivers have been relocated from the edges towards the center of the model (Figure 3.6d). This must be the result of the high-velocity perturbation, as apparently more data is needed in the center than at the edges to obtain a good image quality, given that the rest of the model is laterally homogeneous. It is interesting to notice that this effect apparently overrules the edge effects that showed up in the previous example. The experiment is now repeated for the model in Figure 3.5b

with the higher velocity of the perturbation. It is expected that now even more receivers are needed in the center part of the model. The comparison of the results is shown in Figure 3.7.

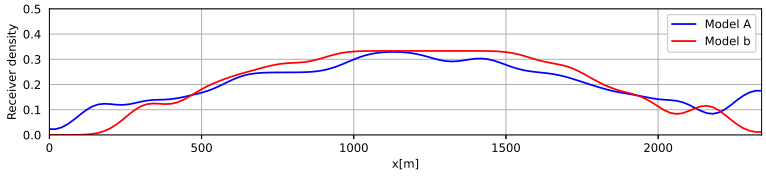

(a) Comparison of optimized receiver densities.

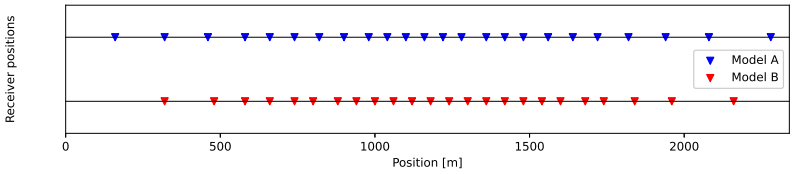

(b) Comparison of optimized geometries.

Figure 3.7: Comparison of optimized geometries for models A (Figure 3.5a) and B (Figure 3.5b). More receivers are located at the center for model B as the velocity perturbation is higher.

From Figure 3.7a, it can be seen that the optimized receiver density for model B is higher at the center than at the edges, with a shape that is indeed more pronounced than the one for model A. Therefore, the corresponding acquisition geometry (Figure 3.7b) for model B has more receivers located at the center than the optimized geometry for model A. From these two results we observe that a more complex subsurface leads to a higher imprint in the optimized acquisition geometry for the best imaging result.

To evaluate the quality of the optimized receiver geometry, we compare the imaging results from two experiments with the model in Figure 3.5b. In the first experiment, FWM is performed with the initial acquisition geometry shown in Figure 3.6a, leading to the image in Figure 3.8a. In the second experiment, FWM is performed with the optimized geometry (Figure 3.6d). The corresponding image is shown in Figure 3.8b. To compare the quality of the images, we plot their amplitude difference with respect to the reference image (Figures 3.8c and 3.8d). Figure 3.8e shows the comparison between the target functions when using the initial (uniform) and optimized geometries.

Figure 3.8c shows a large amplitude difference with respect to the reference model compared to Figure 3.8d. Therefore, it becomes clear that the optimized geometry with more receivers located at the center, allows better imaging of the velocity perturbation. The comparison of the target functions (Figure 3.8e) shows that there is an improvement in the quality of the final image when using the optimized geometry (red curve).

The third model contains a salt dome embedded in a horizontally layered medium (Figure 3.9). We assume a scenario in which, due to the survey constraints, the sources can only be located at the right hand side of the model in the range from $x = 1450$ m to $x = 2450$ m. The sources are uniformly distributed and their spacing is 100 m.

To test the performance of the algorithm, we set up an acquisition geometry with

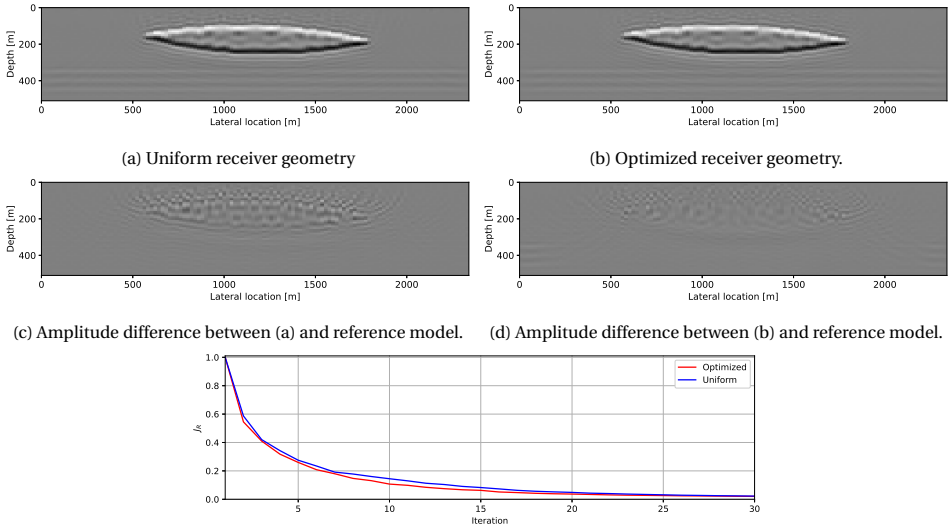

(a) Uniform receiver geometry

(b) Optimized receiver geometry.

(c) Amplitude difference between (a) and reference model.

(d) Amplitude difference between (b) and reference model.

(e) Comparison of target functions.

Figure 3.8: Imaging up to 40 Hz of the model in Figure 3.5b with (a) uniform and (b) optimized geometries.

$n_d = 25$ receivers, all being located at the left-hand side (Figure 3.10a). Our focus is to obtain a good image of the salt overhang, an area that could be of economic interest. Given the source distribution and the geometry of the model, there are no primary reflections related to the salt overhang that can be recorded by the receivers for any acquisition aperture. Therefore, imaging this section with primaries is not feasible. Nonetheless, FWM can make use of internal multiples for this purpose. These internal multiple reflections are generated between the lower horizontal reflector and the salt overhang and reflected towards the right hand side of the model (see red arrows in Figure 3.9). This indicates that the data needed for imaging the salt overhang should be recorded in this area. For this reason, the chosen initial acquisition geometry is far from ideal for this example, but we use it to test the performance of the algorithm. We run 20 iterations of the algorithm and plot the resulting receiver density and corresponding acquisition geometry in Figure 3.10d.

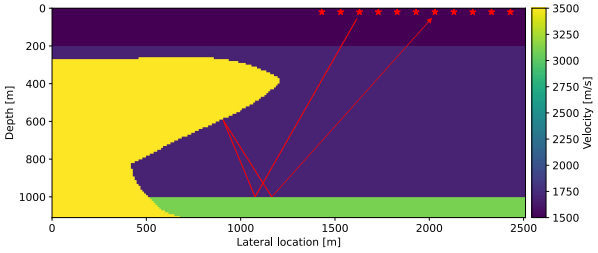

Figure 3.9: Salt dome P-wave velocity model. The lower layer at $z = 1000$ m generates strong internal multiples towards the salt dome overhang. The red stars on the top indicate the position of the sources.

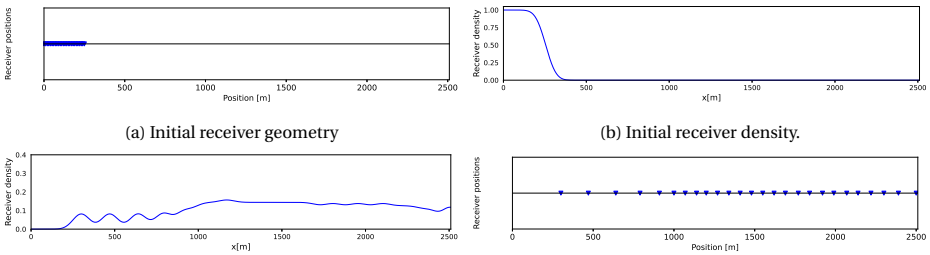

(a) Initial receiver geometry

(b) Initial receiver density.

(c) Optimized receiver density

(d) Optimized receiver geometry.

Figure 3.10: Optimized receiver geometry for the model in Figure 3.9. The receivers are located at the surface $z = 0$ m. After optimization, the receivers are re-located towards the right hand side of the model.

Figure 3.10c shows the optimized receiver density with an increasing tendency from left to right. As mentioned, due to the geometry of the model and the source distribution, the internal multiples generated by the salt overhang are reflected towards the right-hand side of the model (red arrows in Figure 3.9). For this reason, the algorithm tends to increase the receiver density in this part of the model. Therefore, the corresponding acquisition geometry (Figure 3.10d) has more receivers in the right hand side.

To evaluate the quality of the optimized receiver geometry, we again compare the imaging results from two experiments. In the first experiment, FWM is performed with the initial acquisition geometry shown in Figure 3.10a, leading to the image in Figure 3.11a. In the second experiment, FWM is performed with the optimized geometry (Figure 3.10d). The corresponding image is shown in Figure 3.11b.

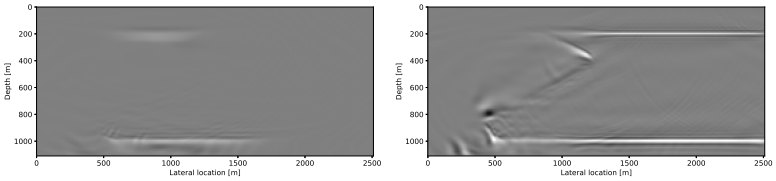

(a) Using the initial geometry in Figure 3.10a.

(b) Using the optimized geometry in Figure 3.10d.

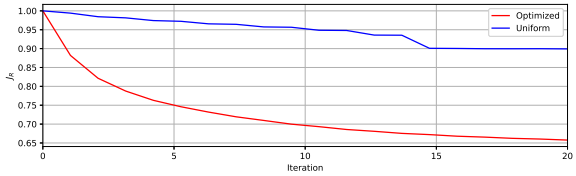

(c) Comparison of target functions.

Figure 3.11: Imaging the model in Figure 3.9.

From the results in Figure 3.11, it can be seen that when the receivers are located at the left-hand side, no part of the salt dome is imaged. Only a few sections of the flat reflectors are visible. This is the result of the absence of multiple reflections in the recorded data, as these waves propagate towards the right-hand side where no receivers are present. This is not the case with the optimized geometry, and the flank of the salt is

indeed imaged. The target function, shown in Figure 3.11c as a function of the iteration number, illustrates this huge difference.

Finally, in a more realistic scenario, we set up a uniform initial receiver geometry. The initial geometry and receiver density as well as the optimized results are shown in Figure 3.12.

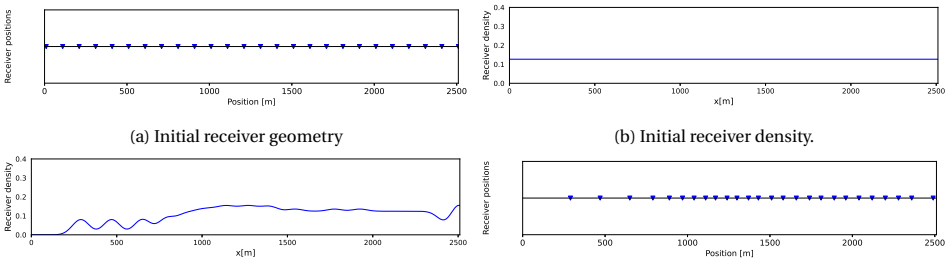

(a) Initial receiver geometry

(b) Initial receiver density.

(c) Optimized receiver density

(d) Optimized receiver geometry.

Figure 3.12: Optimized receiver geometry for the model in Figure 3.9. The receivers are located at the surface $z = 0$ m. After optimization, the receivers are re-located towards the right hand side of the model.

From Figure 3.12 it can be seen that even by having a uniform initial geometry, the optimized result is similar to the one obtained in Figure 3.10. Therefore, the receivers are relocated mostly to the right hand side. We compare again the imaging results obtained with the initial and optimized geometries. The results are shown in Figure 3.13.

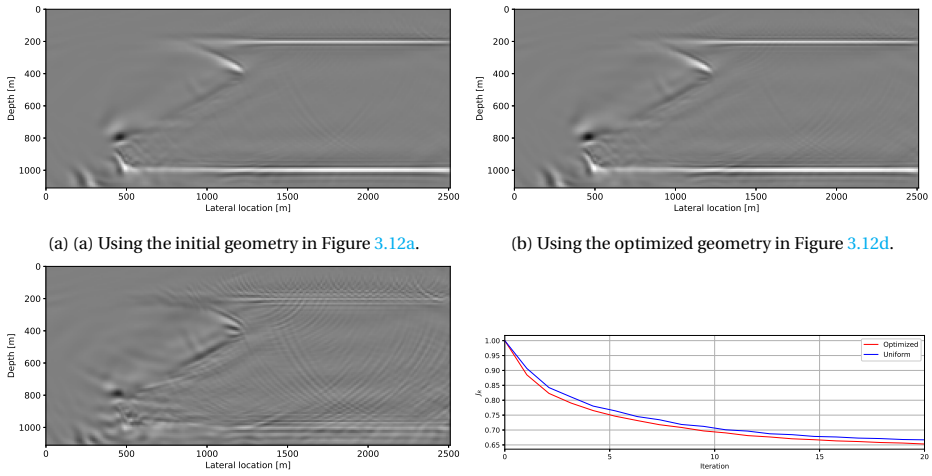

(a) (a) Using the initial geometry in Figure 3.12a.

(b) Using the optimized geometry in Figure 3.12d.

(c) Amplitude difference between (a) and (b)

(d) Comparison of target functions.

Figure 3.13: Imaging the model in Figure 3.9. The target function is lower for the optimized geometry than for the uniform geometry.

Figure 3.13a shows the FWM image obtained when the initial, uniform geometry (Figure 3.12a) is used and Figure 3.13b the image when the optimized geometry (Figure 3.12d) is used. The two results are rather similar, but not identical. Their difference

(Figure 3.13c) shows that there is somewhat more energy present at the flanks of the salt dome in the optimized case. This occurs as more receivers are present in the right-hand side which allows to record more energy from the multiple reflections that illuminate the salt dome from below. This additional illumination is used by FWM to produce the improved image. The normalized target function (J_R), plotted versus iteration number in Figure 3.13d, shows that the target function is indeed minimized more when using the optimized geometry than when using the uniform one.

3.4. DISCUSSION

We have proposed an algorithm that optimizes the acquisition geometry for a particular subsurface model. Such a-priori knowledge on the subsurface could be obtained from legacy surveys. Also in the case of 4D seismics, such knowledge would be available. The results show that an optimized geometry may differ greatly from an initial - e.g., uniform - geometry.

As mentioned, the best seismic image of the subsurface would be obtained from fully sampled data, i.e., data that satisfies the Nyquist-Shannon sampling theorem. However, in practice this is impossible due to the associated high costs and other constraints. Therefore, a survey design methodology has to deal with a reduced number of sources / receivers, which inevitably leads to a reduced image quality. For example, in the case of a geometry with a reduced number of receivers, the particular data carrying the information that allows to image certain part(s) of the subsurface may not be recorded. Our method aims to compensate this deficiency by increasing the receiver density in the zones where more data is needed (while reducing this density in other zones). This phenomenon could be clearly observed in our second example, where the receivers moved towards the center of the aperture to obtain a better image of the velocity perturbation. Here it was also observed that as the velocity of the perturbation became higher, the receiver geometry was adjusted even more.

In this research we focused on the signal of the scattered wavefields in the subsurface. The examples included in this chapter are noise-free. However, in practice, noise is a critical issue to be handled in acquisition design. In the case of noisy data a number of receivers higher than initial proposed, may be required to achieve a certain image quality.

In our iterative scheme, the updates to the receiver density are computed by minimizing the misfit between a reference reflectivity image obtained from a fully sampled geometry and the reflectivity image obtained from the geometry being optimized. Our method could be modified to favour specific zones in the subsurface (target oriented) rather than the full subsurface. This is addressed in chapter 4

In this chapter we chose a parameterization for the receiver geometry that allows to determine the location of individual receivers. In practice these could for instance be the locations of nodal receivers at the water bottom.

Currently our implementation is still in 2D, but extension to 3D is required to make it practical. Similarly, while we focused on the receiver geometry only, also the source geometry could be considered. E.g., during the odd iterations the receiver geometry could be updated while during the even iterations the source geometry could be updated in the same optimization scheme. Because of the symmetry of sources and receivers,

the procedure for optimizing the source density function is identical to the one for the receiver side.

3.5. CONCLUSION

From the results of this research we conclude that a survey design can be adjusted to a particular subsurface when a-priori knowledge of that subsurface is available. This makes it possible to design the acquisition geometry of a (next) seismic survey for optimum imaging.

We recognize the importance of experimental survey design by means of modeling and manual adjustment of the acquisition geometry. However, we believe that a deterministic optimization of the acquisition geometry, such as the one presented in this chapter, could best exploit the content of the available subsurface information. As full-wavefield migration is used as the imaging algorithm, the use of multiples for imaging is taken into account in the survey design.

The examples presented in this chapter show the influence of the subsurface on the acquisition geometry, resulting in optimum, non-uniform receiver density functions. Increasing the subsurface complexity increases the non-uniformity of the receiver distribution.

3.A. APPENDIX A

We repeat equation 3.20 being the derivative of target function $J_{R,i}$ with respect to the receiver density $\mathbf{\Phi}$:

$$\frac{\partial J_{R,i}}{\partial \mathbf{\Phi}} = \frac{\partial}{\partial \mathbf{\Phi}} \left[\sum_n \| \Delta \mathbf{R}_i(z_n) \|_F^2 \right]. \tag{3.A.1}$$

where subscript F denotes the Frobenius norm. We use the definition and rewrite this expression as:

$$\frac{\partial J_{R,i}}{\partial \mathbf{\Phi}} = \frac{\partial}{\partial \mathbf{\Phi}} \left[\sum_n \mathrm{Tr} \left[\Delta \mathbf{R}_i(z_n) \Delta \mathbf{R}_i^H(z_n) \right] \right]. \tag{3.A.2}$$

In order to find the derivative in equation 3.A.2, we seek to express the term $\Delta \mathbf{R}(z_n)$ in terms of the receiver density $\mathbf{\Phi}$. Using equation 3.16, the term $\Delta \mathbf{R}(z_n)$ can be written as:

$$\Delta \mathbf{R}_i(z_n) = \mathbf{R}(z_n) - \mathbf{R}_i(z_n) - \alpha_i \delta \overline{\mathbf{R}}_i(z_n). \tag{3.A.3}$$

From equation 3.18b it follows that $\Delta \mathbf{R}_{i-1}(z_n) = \mathbf{R}(z_n) - \mathbf{R}_i(z_n)$. By substituting this in equation 3.A.3 we obtain:

$$\Delta \mathbf{R}_i(z_n) = \Delta \mathbf{R}_{i-1}(z_n) - \alpha_i \delta \overline{\mathbf{R}}_i(z_n). \tag{3.A.4}$$

Next, we substitute equation 3.12 in equation 3.A.4

$$\Delta \mathbf{R}_i(z_n) = \Delta \mathbf{R}_{i-1}(z_n) - \alpha_i [\mathbf{H}_i(x, z_n)]^{-1} \left[\delta \overline{\mathbf{R}}_i^{\cup}(z_n) - \delta \overline{\mathbf{R}}_i^{\cap}(z_n) \right]. \tag{3.A.5}$$

Subsequently we apply equations 3.9a and 3.9b and assume angle-independent reflectivity, see equations 3.11a and 3.11b:

$$\begin{aligned}\Delta\mathbf{R}_i(z_n) = \Delta\mathbf{R}_{i-1}(z_n) \\ - \alpha_i \left[\mathbf{H}_i(x,z_n)\right]^{-1} \sum_\omega |f|^2 \Big[\left[\mathbf{U}_i^-(z_0;z_n)\right]^H \Delta\mathbf{P}_i(z_0,z_0) \left[\mathbf{X}_i^+(z_n,z_0)\right]^H \\ - \left[\mathbf{U}_i^\cup(z_0,z_n)\right]^H \Delta\mathbf{P}_i(z_0,z_0) \left[\mathbf{X}_{i-1}^-(z_n,z_0)\right]^H \Big]. \end{aligned} \tag{3.A.6}$$

To move along the direction of steepest descent, finite, real-valued updates are needed for the acquisition geometry. Therefore, instead of using the receiver matrix $\mathbf{D}_i(z_0)$, we use the receiver density matrix $\mathbf{\Phi}_i(z_0)$ in equation 3.8a, which then becomes:

$$\Delta\mathbf{P}_i(z_0,z_0) = \mathbf{\Phi}_i(z_0)\Delta\mathbf{X}_i^-(z_0,z_0). \tag{3.A.7}$$

Consequently, we substitute equation 3.A.7 in equation 3.A.6 and obtain:

$$\begin{aligned}\Delta\mathbf{R}_i(z_n) = \Delta\mathbf{R}_{i-1}(z_n) \\ - \alpha_i \left[\mathbf{H}_i(x,z_n)\right]^{-1} \sum_\omega |f|^2 \Big[\left[\mathbf{U}_i^-(z_0,z_n)\right]^H \mathbf{\Phi}_i(z_0)\Delta\mathbf{X}_i^-(z_0,z_0) \left[\mathbf{X}_i^+(z_n,z_0)\right]^H \\ - \left[\mathbf{U}_i^\cup(z_0,z_n)\right]^H \mathbf{\Phi}_i(z_0)\Delta\mathbf{X}_i^-(z_0,z_0) \left[\mathbf{X}_{i-1}^-(z_n,z_0)\right]^H \Big]. \end{aligned} \tag{3.A.8}$$

Therefore, we can write equation 3.A.8 as:

$$\Delta\mathbf{R}_i(z_n) = \mathbf{A}_1\mathbf{Y}\mathbf{B}_1 - \mathbf{A}_2\mathbf{Y}\mathbf{B}_2 + \mathbf{C}, \tag{3.A.9}$$

where:

$$\mathbf{A}_1 = -\alpha_i \left[\mathbf{H}_i(x,z_n)\right]^{-1} \sum_\omega |f|^2 [\mathbf{U}_i^-(z_0,z_n)]^H, \tag{3.A.10a}$$

$$\mathbf{A}_2 = -\alpha_i \left[\mathbf{H}_i(x,z_n)\right]^{-1} \sum_\omega |f|^2 [\mathbf{U}_i^\cup(z_0,z_n)]^H, \tag{3.A.10b}$$

$$\mathbf{B}_1 = \Delta\mathbf{X}_i^-(z_0,z_0)[\mathbf{X}_i^+(z_n,z_0)]^H, \tag{3.A.10c}$$

$$\mathbf{B}_2 = \Delta\mathbf{X}_i^-(z_0,z_0)[\mathbf{X}_{i-1}^-(z_n,z_0)]^H, \tag{3.A.10d}$$

$$\mathbf{C} = \Delta\mathbf{R}_{i-1}(z_n), \tag{3.A.10e}$$

$$\mathbf{Y} = \mathbf{\Phi}(z_0). \tag{3.A.10f}$$

Using this notation, we can write the derivative in equation 3.A.2 as:

$$\frac{\partial J_{R,i}}{\partial \mathbf{\Phi}} = \sum_n \frac{\partial}{\partial \mathbf{Y}} \mathrm{Tr}\left[(\mathbf{A}_1\mathbf{Y}\mathbf{B}_1 - \mathbf{A}_2\mathbf{Y}\mathbf{B}_2 + \mathbf{C})(\mathbf{A}_1\mathbf{Y}\mathbf{B}_1 - \mathbf{A}_2\mathbf{Y}\mathbf{B}_2 + \mathbf{C})^H\right]. \tag{3.A.11}$$

We expand the right-hand side of equation 3.A.11 and obtain:

$$\begin{aligned}\frac{\partial J_{R,i}}{\partial \mathbf{\Phi}} = \sum_n \frac{\partial}{\partial \mathbf{Y}} \mathrm{Tr}\big(&\mathbf{A}_1\mathbf{Y}\mathbf{B}_1\mathbf{B}_1^H\mathbf{Y}^H\mathbf{A}_1^H - \mathbf{A}_1\mathbf{Y}\mathbf{B}_1\mathbf{B}_2^H\mathbf{Y}^H\mathbf{A}_2^H + \mathbf{A}_1\mathbf{Y}\mathbf{B}_1\mathbf{C}^H \\ &-\mathbf{A}_2\mathbf{Y}\mathbf{B}_2\mathbf{B}_1^H\mathbf{Y}^H\mathbf{A}_1^H + \mathbf{A}_2\mathbf{Y}\mathbf{B}_2\mathbf{B}_2^H\mathbf{Y}^H\mathbf{A}_2^H - \mathbf{A}_2\mathbf{Y}\mathbf{B}_2\mathbf{C}^H \\ &+\mathbf{C}\mathbf{B}_1^H\mathbf{Y}^H\mathbf{A}_1^H - \mathbf{C}\mathbf{B}_2^H\mathbf{Y}^H\mathbf{A}_2^H + \mathbf{C}\mathbf{C}^H\big). \end{aligned} \tag{3.A.12}$$

In order to find the derivatives in equation 3.A.12, we make use of the next two identities (Petersen and Pedersen, 2012):

$$\frac{\partial}{\partial \mathbf{Y}}\mathrm{Tr}(\mathbf{AYBY}^H\mathbf{C}) = \mathbf{A}^H\mathbf{C}^H\mathbf{YB}^H + \mathbf{CAYB}. \tag{3.A.13}$$

$$\frac{\partial}{\partial \mathbf{Y}}\mathrm{Tr}(\mathbf{AY}^H\mathbf{B}) = \mathbf{BA}. \tag{3.A.14}$$

By applying equations 3.A.13 and 3.A.14 to equation 3.A.12 we obtain the expression:

$$\begin{aligned}\frac{\partial J_{R,i}}{\partial \mathbf{\Phi}} =& \mathbf{A}_1^H\mathbf{A}_1\mathbf{YB}_1\mathbf{B}_1^H + \mathbf{A}_1^H\mathbf{A}_1\mathbf{YB}_1\mathbf{B}_1^H - \mathbf{A}_1^H\mathbf{A}_2\mathbf{YB}_2\mathbf{B}_1^H - \mathbf{A}_2^H\mathbf{A}_1\mathbf{YB}_1\mathbf{B}_2^H \\ &+\mathbf{A}_1^H\mathbf{CB}_1^H - \mathbf{A}_2^H\mathbf{A}_1\mathbf{YB}_1\mathbf{B}_2^H - \mathbf{A}_1^H\mathbf{A}_2\mathbf{YB}_2\mathbf{B}_1^H + \mathbf{A}_2^H\mathbf{A}_2\mathbf{YB}_2\mathbf{B}_2^H \\ &+\mathbf{A}_2^H\mathbf{A}_2\mathbf{YB}_2\mathbf{B}_2^H - \mathbf{A}_2^H\mathbf{CB}_2^H + \mathbf{A}_1^H\mathbf{CB}_1^H - \mathbf{A}_2^H\mathbf{CB}_2^H,\end{aligned} \tag{3.A.15}$$

which can be further reduced to:

$$\frac{\partial J_{R,i}}{\partial \mathbf{\Phi}} = 2\mathbf{A}_1^H(\mathbf{A}_1\mathbf{YB}_1 - \mathbf{A}_2\mathbf{YB}_2 + \mathbf{C})\mathbf{B}_1^H - 2\mathbf{A}_2^H(\mathbf{A}_1\mathbf{YB}_1 - \mathbf{A}_2\mathbf{YB}_2 + \mathbf{C})\mathbf{B}_2^H. \tag{3.A.16}$$

Finally, by substituting equations 3.A.10a to 3.A.10f in equation 3.A.16 we obtain:

$$\begin{aligned}\frac{\partial J_{R,i}}{\partial \mathbf{\Phi}} = -2\alpha_i \sum_n\sum_\omega |f|^2 [\mathbf{H}_i(x,z_n)]^{-1} \Big\{&\mathbf{U}_i^-(z_0,z_n)\Delta\mathbf{R}_i(z_n)\mathbf{X}_i^+(z_n,z_0) \\ &- \mathbf{U}_i^\cup(z_0,z_n)\Delta\mathbf{R}_i(z_n)\mathbf{X}_{i-1}^-(z_n,z_0)\Big\}[\Delta\mathbf{X}_i^-(z_0,z_0)]^H.\end{aligned} \tag{3.A.17}$$

The term between braces in equation 3.A.17 is a modeled wavefield based on the residual reflectivity image $\Delta\mathbf{R}_i(z_n)$. Therefore, we replace this term with $\Delta\mathbf{P}_r(\Delta\mathbf{R}_i(z_n))$ (See equation 3.15). Consequently, the update direction can be expressed as:

$$\frac{\partial J_{R,i}}{\partial \mathbf{\Phi}} = -2\alpha_i \sum_n\sum_\omega |f|^2 [\mathbf{H}_i(x,z_n)]^{-1} \Delta\mathbf{P}_r(\Delta\mathbf{R}_i(z_n))[\Delta\mathbf{X}_i^-(z_0,z_0)]^H. \tag{3.A.18}$$

Equation 3.A.18 contains the correlation between the data residual $\Delta\mathbf{X}_i^-$ and the wavefield $\Delta\mathbf{P}_r$ modeled from the residual reflectivity image $\Delta\mathbf{R}_i$. Therefore, it can be interpreted as a mapping from the model update to the data space, at the sampling locations where more data is needed. Finally, the update direction is given by:

$$\delta\mathbf{\Phi}_i = -\frac{\partial J_{R,i}^*}{\partial \mathbf{\Phi}}. \tag{3.A.19}$$

3.B. APPENDIX B: DERIVATION OF THE SCALING PARAMETER

In the gradient descent scheme, the optimal scaling parameter is found when the update direction at iteration $i+1$, is orthogonal to the direction at iteration i (Shewchuk, 1994). Therefore, the following condition must hold:

$$[\delta\Phi_{i+1}]^H\delta\Phi_i = 0, \tag{3.B.1}$$

where $\delta\Phi_i$ is a vector obtained from $\delta\Phi_i = \text{diag}\{\delta\mathbf{\Phi}_i\}$. To find the update direction $\delta\mathbf{\Phi}_{i+1}$, we use equation 3.A.18 and assume that the term $\mathbf{\Phi}$, which is implicitly contained, can be linearized.

$$\delta\mathbf{\Phi}_{i+1} = -2\alpha_i \sum_n \sum_\omega |f|^2 \left[\mathbf{H}_i(x,z_n)\right]^{-1} \left[\Delta\mathbf{P}_r(\Delta\mathbf{R}_i(z_n))\right]_{\mathbf{\Phi}} \left[\Delta\mathbf{X}_i^-(z_0,z_0)\right]^H. \tag{3.B.2}$$

The subscript $\mathbf{\Phi}$ in this and subsequent equations, makes reference to the variables computed for finding the optimal scaling parameter. This means, in the direction of $\delta\mathbf{\Phi}_{i+1}$. The wavefield $[\Delta\mathbf{P}_r(\Delta\mathbf{R}_i(z_n))]_{\mathbf{\Phi}}$ is therefore:

$$\begin{aligned}\left[\Delta\mathbf{P}_r(\Delta\mathbf{R}_i(z_n))\right]_{\mathbf{\Phi}} = \mathbf{U}_i^-(z_0,z_n)[\Delta\mathbf{R}_i(z_n)]_{\mathbf{\Phi}}\mathbf{X}_i^+(z_n,z_0) \\ - \mathbf{U}_i^{\cup}(z_0,z_n)[\Delta\mathbf{R}_i(z_n)]_{\mathbf{\Phi}}\mathbf{X}_{i-1}^-(z_n,z_0),\end{aligned} \tag{3.B.3}$$

where $[\Delta\mathbf{R}_i(z_n)]_{\mathbf{\Phi}}$ is:

$$\begin{aligned}&[\Delta\mathbf{R}_i(z_n)]_{\mathbf{\Phi}} = \Delta\mathbf{R}_{i-1}(z_n) \\ &-\alpha_i \left[\mathbf{H}_i(x,z_n)\right]^{-1} \sum_\omega |f|^2 \Big\{ \left[\mathbf{U}_i^-(z_0,z_n)\right]^H \mathbf{\Phi}_{i+1} \Delta\mathbf{X}_i^-(z_0,z_0) \left[\mathbf{X}_i^+(z_n,z_0)\right]^H \\ &\qquad - \left[\mathbf{U}_i^{\cup}(z_0,z_n)\right]^H \mathbf{\Phi}_{i+1} \Delta\mathbf{X}_i^-(z_0,z_0) \left[\mathbf{X}_{i-1}^-(z_n,z_0)\right]^H \Big\}.\end{aligned} \tag{3.B.4}$$

In equation 3.B.4, the receiver density $\mathbf{\Phi}_{i+1}$ is used instead of $\mathbf{\Phi}_i$. Therefore, we may substitute equation 3.19 in equation 3.B.4:

$$\begin{aligned}&[\Delta\mathbf{R}_i(z_n)]_{\mathbf{\Phi}} = \Delta\mathbf{R}_{i-1}(z_n) \\ &-\alpha_i \left[\mathbf{H}_i(x,z_n)\right]^{-1} \sum_\omega |f|^2 \Big\{ \left[\mathbf{U}_i^-(z_0,z_n)\right]^H (\mathbf{\Phi}_i + \beta_i\delta\mathbf{\Phi}_i) \Delta\mathbf{X}_i^-(z_0,z_0) \left[\mathbf{X}_i^+(z_n,z_0)\right]^H \\ &\qquad - \left[\mathbf{U}_i^{\cup}(z_0,z_n)\right]^H (\mathbf{\Phi}_i + \beta_i\delta\mathbf{\Phi}_i) \Delta\mathbf{X}_i^-(z_0,z_0) \left[\mathbf{X}_{i-1}^-(z_n,z_0)\right]^H \Big\}.\end{aligned} \tag{3.B.5}$$

By substituting equation 3.B.5 in equation 3.B.3, and substituting the result in equation 3.B.2 we obtain:

$$\delta\mathbf{\Phi}_{i+1} = \delta\mathbf{\Phi}_i - 2\alpha_i\beta_i \sum_n \sum_\omega |f|^2 \left[\mathbf{H}_i(x,z_n)\right]^{-1} \Delta\mathbf{P}_r(\mathbf{R}_\phi(z_n))[\Delta\mathbf{X}_i^-(z_0,z_0)]^H, \tag{3.B.6}$$

where $\mathbf{R}_\phi(z_n)$ is an image obtained from:

$$\begin{aligned}\mathbf{R}_\phi(z_n) = -\alpha_i \left[\mathbf{H}_i(x,z_n)\right]^{-1} \sum_\omega \Big\{ \left[\mathbf{U}_i^-(z_0,z_n)\right]^H \delta\mathbf{\Phi}_i \Delta\mathbf{X}_i^-(z_0,z_0) \left[\mathbf{X}_i^+(z_n,z_0)\right]^H \\ - \left[\mathbf{U}_i^{\cup}(z_0,z_n)\right]^H \delta\mathbf{\Phi}_i \Delta\mathbf{X}_i^-(z_0,z_0) \left[\mathbf{X}_{i-1}^-(z_n,z_0)\right]^H \Big\}.\end{aligned} \tag{3.B.7}$$

Finally, by substituting equation 3.B.6 in equation 3.B.1, we obtain the optimal scaling parameter:

$$\beta_i = \frac{(\delta\Phi_i)^H \delta\Phi_i}{\text{diag}\left\{-2\alpha_i \sum_n \sum_\omega |f|^2 \left[\mathbf{H}_i(x,z_n)\right]^{-1} \Delta\mathbf{P}_r(\mathbf{R}_\phi(z_n))[\Delta\mathbf{X}_i^-(z_0,z_0)]^H\right\}^H \delta\Phi_i}. \tag{3.B.8}$$

From equation 3.B.8, the denominator can be computed via the following steps:

1. Compute the reflectivity image $\mathbf{R}_\phi(z_n)$
2. From this image, model seismic data $\Delta\mathbf{P}_r(\mathbf{R}_\phi(z_n))$
3. Correlate this data with the data residual $\Delta\mathbf{X}_i^-(z_0, z_0)$.
4. Correlate this result with the current update direction $\delta\Phi_i$.

BIBLIOGRAPHY

[1] M. Alerini, B. Traub, C. Ravaut, and E. Duveneck. "Prestack depth imaging of ocean-bottom node data". *Geophysics* 74 (2009), WCA57–WCA63.

[2] A. J. Berkhout. *Seismic migration, imaging of acoustic energy by wave field extrapolation, A. theoretical aspects*. Elsevier, 1982.

[3] A. J. Berkhout, L. Ongkiehong, A. W. F. Volker, and G. Blacquière. "Comprehensive assessment of seismic acquisition geometries by focal beams—Part I: Theoretical considerations". *Geophysics* 66 (2001), pp. 911–917.

[4] A. Berkhout. "Review Paper: An outlook on the future of seismic imaging, Part I: forward and reverse modelling". *Geophysical Prospecting* 62 (2014), pp. 911–930.

[5] A. Berkhout. "Review Paper: An outlook on the future of seismic imaging, Part II: Full-Wavefield Migration". *Geophysical Prospecting* 62 (2014), pp. 931–949.

[6] M. Davydenko and D. Verschuur. "Full-wavefield migration: using surface and internal multiples in imaging: Full wavefield migration". *Geophysical Prospecting* 65 (2017), pp. 7–21.

[7] M. Davydenko. "Full wavefield migration: Seismic imaging using multiple scattering effects". PhD Thesis. Delft University of Technology, 2016.

[8] M. Davydenko and D. J. Verschuur. "Including and using internal multiples in closed-loop imaging — Field data examples". *Geophysics* 83 (2018), R297–R305.

[9] A. Kumar, G. Blacquière, and E. Verschuur. "Extending illumination using all multiples: application to 3D acquisition geometry analysis: Extending illumination using multiples". *Geophysical Prospecting* 64 (2016), pp. 622–641.

[10] S. Lloyd. "Least squares quantization in PCM". *IEEE Transactions on Information Theory* 28 (1982), pp. 129–137.

[11] H. Maurer, A. Curtis, and D. E. Boerner. "Recent advances in optimized geophysical survey design". *Geophysics* 75 (2010), 75A177–75A194.

[12] D. Muerdter and D. Ratcliff. "Understanding subsalt illumination through ray-trace modeling, Part 1: Simple 2-D salt models". *The Leading Edge* 20 (2001), pp. 578–594.

[13] S. Nakayama, G. Blacquière, and T. Ishiyama. "Automated survey design for blended acquisition with irregular spatial sampling via the integration of a metaheuristic and deep learning". *Geophysics* 84 (2019), P47–P60.

[14] K. B. Petersen and M. S Pedersen. *The Matrix Cookbook*. 2012.

[15] C. J. Regone. "A modeling approach to wide-azimuth design for subsalt imaging". *The Leading Edge* 25 (2006), pp. 1467–1475.

[16] B. Revelo-Obando and G. Blacquière. “Acquisition geometry analysis with point-spread functions”. *Geophysical Prospecting* 69 (2021), pp. 1606–1624.

[17] B. Revelo-Obando and G. Blacquière. “Seismic acquisition design based on full-wavefield migration”. *Geophysics* 88 (2023), P37–P49.

[18] A. Secord. “Weighted Voronoi Stippling”. *Proceedings of the 2nd International Symposium on Non-Photorealistic Animation and Rendering*. 2002.

[19] J. R. Shewchuk. *An Introduction to the Conjugate Gradient Method Without the Agonizing Pain*. Technical Report. USA: Carnegie Mellon University, 1994.

[20] V. Singh, A. Venkataraman, R. Ho, E. Neumann, and B. Laugier. “Ocean-bottom node acquisition optimization”. *SEG Technical Program Expanded Abstracts 2016*. 2016.

[21] X. Staal. “Combined imaging and velocity estimation by Joint Migration Inversion”. PhD thesis. Technische Universiteit Delft, 2015.

[22] C. Theriot, M. McDonald, M. R. Kamarudin, and P. Yu. “Survey design for optimized ocean bottom node acquisition”. *SEG Technical Program Expanded Abstracts 2014*. 2014.

[23] G. J. O. Vermeer. *3D Seismic Survey Design*. 2nd ed. Geophysical References Series. Society of Exploration Geophysicists, 2012.

[24] A. W. F. Volker, G. Blacquière, A. J. Berkhout, and L. Ongkiehong. “Comprehensive assessment of seismic acquisition geometries by focal beams—Part II: Practical aspects and examples”. *Geophysics* 66 (2001), pp. 918–931.

[25] C. P. A. Wapenaar and A. J. Berkhout. *Elastic wave field extrapolation*. OCLC: 693470515. Elsevier, 1989.

[26] S. Wu, D. J. Verschuur, and G. Blacquière. “Automated Seismic Acquisition Geometry Design for Optimized Illumination at the Target: A Linearized Approach”. *IEEE Transactions on Geoscience and Remote Sensing* 60 (2022), pp. 1–13.

4

TARGET-ORIENTED SURVEY DESIGN BASED ON FULL-WAVEFIELD MIGRATION

The ultimate goal in survey design is to find the acquisition parameters that enable acquiring high-quality data suitable for optimal imaging. This, while fulfilling budget and HSE constraints. We propose a target-oriented acquisition design algorithm based on Full-Wavefield Migration. The algorithm optimizes a receiver density function that indicates the number of receivers per unit area required for obtaining the best possible image quality. The method makes use of available seismic data to create a reference model which is included in the proposed objective function. To make the design target-oriented, the objective function is multiplied with a mask that gives more weight to the target areas of interest. The results of the 2D and 3D implementations show an optimized receiver density function with higher values at the zones where more data is needed for improving image quality. The corresponding receiver geometries have more receivers placed at these areas. We validate the results by computing the images of the target zone using uniform and optimized geometries. The use of the latter shows an improvement in the image quality at the target zone. Additionally, we compute the number of receivers required for achieving a certain signal-to-noise ratio after imaging based on the optimized receiver density function.

This chapter has been accepted for publication as Revelo-Obando and Blacquiére (2024) in *Geophysics*.

4.1. INTRODUCTION

Acquisition design for seismic surveys aims to optimize the acquisition parameters that enable adequate sampling of the seismic wavefield and the noise. These parameters have to be adjusted according to the area under consideration, budget, HSE constraints, expected signal properties and the noise level. Two of the acquisition parameters, namely the temporal and the spatial sampling interval, should ideally be chosen in such a way that signal and noise are recorded unaliased, i.e., these intervals satisfy the Nyquist criterion of more than two samples per smallest wavelength. For the temporal sampling interval this is no problem, but for the spatial sampling interval this is often not feasible due to the associated costs. The spatial sampling locations are determined by the positions of the seismic sources and the active receivers during each shot record, known as the active spread. This set of locations is known as the acquisition geometry. Knowing that the ideal geometry is out of reach, it must be designed to achieve the following: adequate spatial sampling of the low-velocity noise, high trace multiplicity to achieve an acceptable signal-to-noise ratio (SNR) in particular at the subsurface target(s) of economical interest; and these while fulfilling the economical constraints.

The spatial sampling requirements must also be selected according to the data processing algorithms that follow the data acquisition. In the pre-processing stage for instance, noise-suppression algorithms are applied to improve the data quality. These algorithms may require a certain minimum spatial sampling to successfully remove the noise. In land acquisition for example, the low velocity noise such as ground roll may require a finer sampling than the signal of interest. For the purpose of imaging and velocity inversion, some algorithms may require a denser spatial sampling than others. Algorithms such as Full-Waveform Inversion (FWI) for velocity estimation and Marchenko imaging, for instance, require densely sampled data (Wapenaar et al., 2014). When this is not possible, extra preprocessing steps such as data interpolation may be needed. Other algorithms such as Full-Wavefield Migration (FWM) (Davydenko and Verschuur, 2017), require a less dense spatial sampling as imaging is possible despite acquisition gaps through the use of multiple reflections.

In a traditional acquisition geometry, sources and receivers are placed along straight lines. One of the most common types of land geometry is the *orthogonal geometry*, in which the source and receiver lines are orthogonal to each other (Vermeer, 2012; Cordsen et al., 2000). The separation between these lines, their lengths, the spatial sampling along the lines and the active spread, determine the common midpoint (CMP) properties of the survey, such as offset distribution and fold (Vermeer, 2012). The fold and the SNR of the data dictate the resulting SNR of the final seismic product. Therefore, in areas in which a high level of non-coherent noise is expected, the acquisition geometry should be adjusted to obtain a suitable SNR.

Ideally, in the noise-free case, the expected resolution of a seismic image could be computed from the acquisition aperture and the seismic bandwidth. However, in complex media, the wavefields illuminating the target zones and reflecting back to the acquisition surface are highly scattered, possibly resulting in a decreased illumination and detection of the target zone (Revelo-Obando and Blacquière, 2021). Therefore, in areas where prior information of the subsurface is available, the survey design can be adjusted to obtain better imaging.

One way to optimize the survey design is through the use of numerical modeling studies, in which a seismic experiment is simulated numerically to obtain the expected seismic image corresponding to a certain acquisition geometry. When the outcome of the experiment is not satisfactory the acquisition geometry is manually adjusted (Singh et al., 2016; Theriot et al., 2014). This type of study does not provide a theoretical relation between the changes in the acquisition geometry and the resulting seismic image. Other types of model-based optimization studies use a seismic model to determine the location of seismic sources and receivers that allows to maximize the information content in FWI (Maurer et al., 2010; Krampe et al., 2021; Winner et al., 2023).

In areas where seismic surveys have been carried out previously, legacy seismic data and corresponding seismic images are available. These can be used to optimize the design of a future survey. When the target area of economical interest has been identified, the acquisition geometry can be optimized to improve the illumination and detection properties at that target area. The Focal Beam Analysis method for instance (Volker et al., 2001; van Veldhuizen et al., 2008) is suitable to analyze the illumination and resolution properties of a specific acquisition geometry at one particular subsurface target point. The method can also include the additional illumination from multiple reflections (Kumar et al., 2016) or be used to automatically compute the acquisition geometry for optimum illumination at the target point (Wu et al., 2022).

In productive subsurface reservoirs, e.g., for carbon capture and storage, hydrocarbon production, geothermal energy harvesting, the elastic properties of the reservoir change due to the injection and/or extraction of fluids or gasses. Therefore, multiple surveys can be acquired at different time instances to monitor the changes in these properties. This type of acquisition is known as time lapse or 4D acquisition. In the first 4D surveys, the acquisition and processing parameters were kept constant so that the changes in processed 3D volumes could be attributed to changes in the reservoir only (assuming that no changes in the overburden take place) (Greaves and Fulp, 1987). However, new techniques have been proposed to estimate the changes in the dynamic properties of the reservoir using data acquired with non-replicated geometries (Oghenekohwo et al., 2017; Nakayama et al., 2019; Qu and Verschuur, 2020). In this case, at later production stages, the survey design can be adjusted specifically to the target zone without replicating the baseline survey.

In this chapter we present an iterative algorithm based on our previous work (Revelo-Obando and Blacquière, 2023) for designing a target-oriented acquisition geometry. In this initial phase of our work, we assume the source geometry to be fixed and aim to optimize the receiver geometry, which we assume to be stationary. We parameterize the latter with a density function that is related to the number of receivers per unit area. This receiver density function is updated at each iteration using a gradient descent scheme. We propose an objective function that measures the difference between the image obtained with the current-iteration acquisition geometry and a reference image obtained with an ideal receiver distribution. To implement a target-oriented acquisition design, the objective function is computed using a spatially-varying mask that puts more weight to the target zone and less weight to areas that are less important. The actual receiver positions are computed from the receiver density function with a Voronoi Stippling algorithm. The receiver density is interpreted as a relative density, meaning that the actual

number of receivers is chosen separately, e.g., depending on the expected noise level, or on the available equipment.

The chapter is organized as follows: first we lay out the framework of survey design and FWM. Subsequently, we define the parameterization and the target-oriented objective function. Next, we explain the iterative process which is the core of the optimization algorithm. Then, we show some study cases to demonstrate the performance of the algorithm. We finalize the chapter with concluding remarks.

4.2. THEORY

4.2.1. FRAMEWORK OF SURVEY DESIGN

We describe 3D seismic data with the matrix notation introduced by Berkhout, 1982. For a stationary acquisition geometry, one frequency component of a seismic data set can be formulated as:

$$\mathbf{P}^-(z_d, z_s) = \mathbf{D}(z_d)\mathbf{X}^-(z_d, z_s)\mathbf{S}(z_s). \tag{4.1}$$

Matrix $\mathbf{P}^-$ is the upgoing acoustic pressure wavefield, recorded at the acquisition level z_d and generated by the sources at level z_s. Matrices $\mathbf{D}(z_d)$ and $\mathbf{S}(z_s)$ are the receiver and source matrices, respectively. They describe the acquisition geometry and contain the properties of the receivers and sources, such as sensitivity, directivity and spectral properties. The superscripts $-$ and $+$ (which will appear later) indicate wavefields in the upgoing and downgoing directions, respectively. Matrix $\mathbf{X}^-$ is the transfer operator of the subsurface, containing the propagation and reflection effects. It can be considered as the ideal data set, i.e., with fully sampled ideal, point sources and receivers. If the sources and receivers are located at the surface z_0, i.e., $z_0 = z_s = z_d$, equation 4.1 becomes:

$$\mathbf{P}^-(z_0, z_0) = \mathbf{D}(z_0)\mathbf{X}^-(z_0, z_0)\mathbf{S}(z_0). \tag{4.2}$$

Assuming ideal, fully-sampled point sources, matrix $\mathbf{S}(z_0)$ becomes the identity matrix $\mathbf{I}$. In this case equation 4.2 becomes:

$$\mathbf{P}^-(z_0, z_0) = \mathbf{D}(z_0)\mathbf{X}^-(z_0, z_0). \tag{4.3}$$

The modeling of the dataset $\mathbf{X}^-(z_0, z_0)$ can be done with any modelling engine, e.g., with finite-difference modeling. We choose Full-Wavefield Modeling (FWMod) (Berkhout, 2014). This is an iterative method that models the downgoing wavefield $\mathbf{X}_i^+(z_n, z_0)$ and the upgoing wavefield $\mathbf{X}_i^-(z_n, z_0)$ recursively in depth for N depth levels. At each iteration i, the downgoing wavefield is computed for $z_n = z_0, z_1, ..., z_N$ and subsequently the upgoing wavefield computed for $z_n = z_N, z_{N-1}, ..., z_0$. Each iteration is called one round trip, as it starts with the downgoing wavefield at the surface z_0 and ends with the upgoing wavefield at the same level. At each round trip one order of multiple reflections is added, starting with the primary reflections when $i = 0$ and adding the L-order multiple reflections for L iterations. It can be formulated as:

$$\mathbf{X}_i^+(z_n, z_0) = \sum_{m=1}^{n-1} \mathbf{U}^+(z_n, z_m)\mathbf{R}^\cap(z_m)\mathbf{X}_{i-1}^-(z_m, z_0) + \mathbf{U}^+(z_n, z_0), \tag{4.4a}$$

$$\mathbf{X}_i^-(z_n, z_0) = \sum_{m=n+1}^{N} \mathbf{U}^-(z_n, z_m)\mathbf{R}^\cup(z_m)\mathbf{X}_i^+(z_m, z_0). \tag{4.4b}$$

This scheme is equivalent to a Bremmer series expansion. See Davydenko (2016) for details. Matrices $\mathbf{R}^{\cap}(z_m)$ and $\mathbf{R}^{\cup}(z_m)$ are the up-down and down-up, angle-dependent reflection operators at depth level z_m, respectively. Matrix $\mathbf{U}^{+}(z_n, z_m)$ includes all propagation and transmission effects of wavefields propagating in the downward direction from depth level z_m to depth level z_n, and so does operator $\mathbf{U}^{-}(z_n, z_m)$ for wavefields propagating in the upward direction. They are computed as follows:

$$\mathbf{U}^{+}(z_n, z_m) = \left[\prod_{k=n-1}^{m+1} \mathbf{W}^{+}(z_{k+1}, z_k)\mathbf{T}^{+}(z_k)\right]\mathbf{W}^{+}(z_{m+1}, z_m), \tag{4.5a}$$

$$\mathbf{U}^{-}(z_n, z_m) = \left[\prod_{k=n+1}^{m-1} \mathbf{W}^{-}(z_{k-1}, z_k)\mathbf{T}^{-}(z_k)\right]\mathbf{W}^{-}(z_{m-1}, z_m), \tag{4.5b}$$

where $\mathbf{W}^{+}(z_{k+1}, z_k)$ is the downward wavefield propagation operator from depth level z_k to depth level z_{k+1}; $\mathbf{W}^{-}(z_{k-1}, z_k)$ is the upward wavefield propagation operator from depth level z_k to depth level z_{k-1}; $\mathbf{T}^{+}(z_k)$ is the transmission operator of the downgoing wavefield crossing depth level z_k from above; $\mathbf{T}^{-}(z_k)$ is the transmission operator of the upgoing wavefield crossing depth level z_k from below.

The use of this type of modeling allows to specify reflectivity and transmissivity independently from propagation velocity. The output of this scheme, after L iterations, is the modeled, perfectly sampled data, $\mathbf{X}_L^{-}(z_0, z_0) = \mathbf{X}^{-}(z_0, z_0)$. The more realistic dataset $\mathbf{P}_i(z_0, z_0)$ can be obtained via multiplication with $\mathbf{D}(z_0)$, see equation 4.3 (still under the assumption of a perfect source distribution). As we discuss the acoustic case, the transmission operators can be described in terms of the reflectivity:

$$\mathbf{T}^{+}(z_k) = \mathbf{I} + \mathbf{R}^{\cup}(z_k), \tag{4.6a}$$

$$\mathbf{T}^{-}(z_k) = \mathbf{I} + \mathbf{R}^{\cap}(z_k). \tag{4.6b}$$

4.2.2. REFLECTIVITY ESTIMATION WITH FWM

FWM is an iterative, least-squares imaging algorithm that estimates a reflectivity model by minimizing the difference between observed and synthetic data modeled through FWMod. During the iterations i the reflectivity is updated using a gradient descent scheme:

$$\mathbf{R}_{i+1}(z_n) = \mathbf{R}_i(z_n) + \alpha_i \delta\overline{\mathbf{R}}_i(z_n), \tag{4.7}$$

where $\delta\overline{\mathbf{R}}_i(z_n)$ is the update direction and α_i the scaling parameter for the gradient descent scheme. The detailed derivation is discussed by Davydenko and Verschuur (2017).

4.3. METHOD

The method we introduce in this chapter is based on our previous work (Revelo-Obando and Blacquière, 2023). Our objective is to design the optimal receiver matrix $\mathbf{D}_i$ that leads to the best possible reflectivity estimate $\mathbf{R}_i$ given a fixed number of receivers n_d, which comes down to determining the optimum locations of these n_d receivers. This is done through an iterative process. At each iteration i, matrix $\mathbf{D}_i$ contains the position of the n_d receivers. The receiver locations are not completely arbitrary, but they are located on a pre-defined grid.

Assuming ideal point receivers, i.e., with a flat, unit sensitivity for each frequency component, matrix $\mathbf{D}_i(z_0)$ is a diagonal matrix whose elements are either one or zero, indicating the presence or absence of a receiver at a grid position, respectively. Therefore, updating the operator implies changing a zero into a one at certain locations while changing a one into a zero at an identical number of other locations. In this way the total number of receivers does not change.

We assume that the fully-sampled, ideal data $\mathbf{X}^{-}(z_0, z_0)$ is available, i.e., modeled based on prior subsurface information. From this data we create a reference image $\mathbf{R}$ through FWM using the velocity model from the same subsurface information. This image is considered the best possible reflectivity estimate (given the imaging method) as full receiver sampling is used. Therefore, at the end of each iteration, we compare the reflectivity estimate $\mathbf{R}_i$ with the reference image $\mathbf{R}$ through a target function that is introduced later. We use a gradient descent scheme for minimizing this target function and updating the acquisition geometry. However, such a scheme requires a continuous real-valued function rather than the binary elements of matrix $\mathbf{D}_i$. Therefore, an intermediate parameterization is required. This is described in the next section.

4.3.1. PARAMETERIZATION

We use a density function $\mathbf{\Phi}_i$ that indicates the relative density of receivers per unit area at the acquisition surface (Wu, 2020). This function is translated into an actual acquisition geometry through a transformation g as follows:

$$\mathbf{D}_i = g(\mathbf{\Phi}_i). \tag{4.8}$$

The transformation process is discussed more extensively in Revelo-Obando and Blacquière, 2023. Figure 4.1 illustrates the this process. As an example, we create a density function that increases linearly from zero to one in the $x-$ direction (Figure 4.1a). In the zone of the lower x coordinates the density values are low. Consequently, less receivers per unit area are placed here (Figure 4.1b). The opposite occurs for the higher x coordinates: the density values are high, resulting in a high number of receivers per unit area.

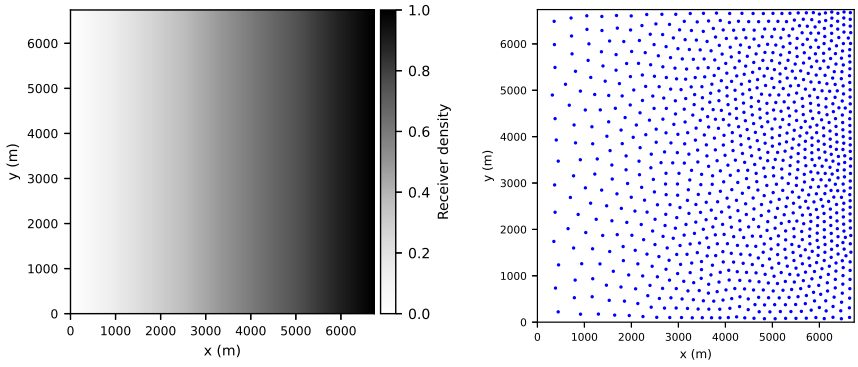

Figure 4.1: (a) Relative receiver density. (b) Receiver geometry created through the transformation f for $n_d = 1000$.

4.3.2. OBJECTIVE FUNCTION

In Chapter 3 we introduced a least-squares objective function to measure the performance of an acquisition geometry. This objective function quantifies the absolute difference between the updated reflectivity image $\mathbf{R}_{i+1}(z_n)$, which is obtained with the current acquisition geometry $\mathbf{D}_i$, and the reference image $\mathbf{R}(z_n)$. The objective function is defined as:

$$J_{R,i} = \sum_n \|\Delta\mathbf{R}_i(z_n)\|_F^2, \tag{4.9a}$$

$$\Delta\mathbf{R}_i(z_n) = \mathbf{R}(z_n) - \mathbf{R}_{i+1}(z_n). \tag{4.9b}$$

The residual $\Delta\mathbf{R}_i$ is the difference between the reference image and the new estimate. The initial reflectivity image $\mathbf{R}_1(z_n)$ is obtained after one FWM iteration using an initial receiver geometry $\mathbf{D}_i$ for $i = 0$ and with n_d receivers. We now introduce a modification of the objective function that gives more weight to one or more target zones. In this way the focus is to obtain an acquisition geometry that enables better imaging of these target zones. For this purpose, we apply a mask $\mathbf{\Psi}(z_n)$ that scales the residual image:

$$J_{T,i} = \sum_n \|\mathbf{\Psi}(z_n)\Delta\mathbf{R}_i(z_n)\|_F^2, \tag{4.10}$$

where $J_{T,i}$ is the new target-oriented objective function. Matrix $\mathbf{\Psi}(z_n)$ is a spatially-varying weighting function whose elements range between 0 and 1. Target zones are given higher values than zones of less importance. In the case that a uniform image quality is desired, matrix $\mathbf{\Psi}$ must be filled with equal numbers.

4.3.3. GRADIENT DESCENT SCHEME

The receiver density function is updated through an iterative gradient descent scheme:

$$\mathbf{\Phi}_{i+1} = \mathbf{\Phi}_i + \beta_i \delta\mathbf{\Phi}_i, \tag{4.11}$$

where $\mathbf{\Phi}_i$ is the current-iteration receiver density, $\delta\mathbf{\Phi}_i$ is the update direction, β_i is the step length, and $\mathbf{\Phi}_{i+1}$ is the updated, next-iteration receiver density.

4.3.4. UPDATE DIRECTION AND STEP LENGTH

The update direction for the receiver density is related to the gradient of the objective function $J_{T,i}$ (equation 4.10) with respect to receiver density $\mathbf{\Phi}$. Therefore, the derivative to be computed is:

$$\frac{\partial J_{T,i}}{\partial \mathbf{\Phi}} = \frac{\partial}{\partial \mathbf{\Phi}} \left[\sum_n \|\mathbf{\Psi}(z_n)\Delta\mathbf{R}_i(z_n)\|_F^2 \right]. \tag{4.12}$$

As demonstrated in Appendix 4.A, this derivative can be expressed as:

$$\frac{\partial J_{T,i}}{\partial \mathbf{\Phi}} = -2\alpha_i \sum_n \sum_\omega \Delta\mathbf{P}_r(\mathbf{\Psi}(z_n)\Delta\mathbf{R}_i(z_n))[\Delta\mathbf{X}_i^-(z_0,z_0)]^H, \tag{4.13}$$

where $\Delta\mathbf{X}_i^-$ is the data residual, i.e., the difference between the modeled and reference data. The term $\Delta\mathbf{P}_r$ is a seismic wavefield modeled from the weighted residual

image $\mathbf{\Psi}(z_n)\Delta\mathbf{R}_i$. Equation 4.13 contains the correlation between this wavefield and the data residual $\Delta\mathbf{X}_i^-$. Therefore, it can be interpreted as a mapping from the model domain, specifically the scaled residual image, to the data domain, indicating the sampling locations where more data is needed to improve imaging of the target zone.

The update direction is given by the negative conjugate of equation 4.13:

$$\delta\mathbf{\Phi}_i = -\frac{\partial J_{T,i}^*}{\partial\mathbf{\Phi}}, \tag{4.14}$$

and the step length (Appendix 4.B) is given by:

$$\beta_i = \frac{(\delta\Phi_i)^H\delta\Phi_i}{\text{diag}\{-2\alpha_i\sum_n\sum_\omega\Delta\mathbf{P}_r(\mathbf{\Psi}(z_n)\mathbf{R}_\phi(z_n))[\Delta\mathbf{X}_i^-(z_0,z_0)]^H\}^H\delta\Phi_i}, \tag{4.15}$$

where $\mathbf{R}_\phi(z_n)$ is an image associated with the receiver density update direction in equation 4.14 and $\Delta\mathbf{P}_r(\mathbf{\Psi}(z_n)\mathbf{R}_\phi(z_n))$ is the corresponding wavefield perturbation.

Before updating the receiver density function, we apply a spatial filter to the update direction in equation 4.14 to smooth the gradient and account for possible unstable behavior caused by sparse 3D acquisition geometries. Subsequently, the receiver density function can be updated by using equation 4.11. The resulting updated density $\mathbf{\Phi}_{i+1}$ is transformed into the new acquisition geometry $\mathbf{D}_{i+1}$ through the transformation g.

4.3.5. ALGORITHM

At each iteration of the algorithm, the current receiver geometry is applied to the fully-sampled dataset, leading to the practical data $\mathbf{P}_i^-(z_0,z_0) = \mathbf{D}_i(z_0)\mathbf{X}_i^-(z_0,z_0)$. With this data, one iteration of FWM is performed, updating the reflectivity estimate from $\mathbf{R}_i(z_n)$ to $\mathbf{R}_{i+1}(z_n)$. Subsequently, the objective function is evaluated. In the case the updated reflectivity does not satisfy a pre-defined quality criterion ϵ, the acquisition geometry is updated. The quality of this geometry is evaluated through a new FWM iteration and repeating the aforementioned steps until the quality criterion is satisfied.

The iterative process to optimize the receiver geometry is summarized in Algorithm 1. In the next section it will be discussed that it may be necessary to change the number of receivers n_d and restart this process.

Algorithm 2 Acquisition geometry optimization algorithm

Require: $\mathbf{X}^-(z_0,z_0), \mathbf{R}, \mathbf{D}_0, \mathbf{\Psi}$

for $0 \le i \le$ `nit` **do** ▷ Acquisition geometry with `nit` updates
  Compute wavefields $\mathbf{X}_i^+, \mathbf{X}_i^-$
  $\Delta\mathbf{P}_i = \mathbf{D}_i\Delta\mathbf{X}_i^-$ ▷ Apply receiver geometry, compute data residual
  $\mathbf{R}_{i+1} = \mathbf{R}_i + \alpha_i\delta\mathbf{R}_i$ ▷ Update reflectivity
  if $J_{T,i} < \epsilon$ **then** ▷ Evaluate image quality criterion
    Finish
  end if
  $\mathbf{\Phi}_{i+1} = \mathbf{\Phi}_i + \beta_i\delta\mathbf{\Phi}_i$ ▷ Update receiver density
  $\mathbf{D}_{i+1} = g(\mathbf{\Phi}_{i+1})$ ▷ Update receiver geometry
end for

4.3.6. MODIFYING THE NUMBER OF RECEIVERS

The output of the optimization algorithm is the optimized receiver density $\mathbf{\Phi}$. This function is related to the number of receivers per unit area. This means that multiple acquisition geometries with different numbers of receivers can be generated. In practice, this number of receivers can be chosen based on constraints such as the available hardware, or a minimum target SNR, that depends on the field noise level.

To determine number of required receivers that are necessary to achieve a certain SNR, we model seismic data $\mathbf{P}^- = \mathbf{D}\mathbf{X}^-$ with n_d receivers and add white noise. Using this data, $\mathbf{\Phi}$ is computed with our algorithm. Next, we generate an acquisition geometry $\mathbf{D}_\kappa$ with κn_d receivers, where κ is a factor that can be both larger or smaller than one, corresponding to more or fewer receivers, and apply it to get seismic data $\mathbf{P}^-_\kappa = \mathbf{D}_\kappa \mathbf{X}^-$. Then, through FWM, we obtain the corresponding image $\mathbf{R}_\kappa(z_n)$ and compute the corresponding SNR. Depending on the outcome, we either increase or decrease κ and repeat the procedure until the SNR criterion is met.

4.4. RESULTS

4.4.1. 2D IMPLEMENTATION

First, we tested our algorithm with a 2D implementation. We used a slice of the SEG salt model (Figure 4.2). We then create synthetic data via FWMod and do imaging via FWM using full receiver sampling to create the reference reflectivity model. The sources are uniformly distributed every 400 m.

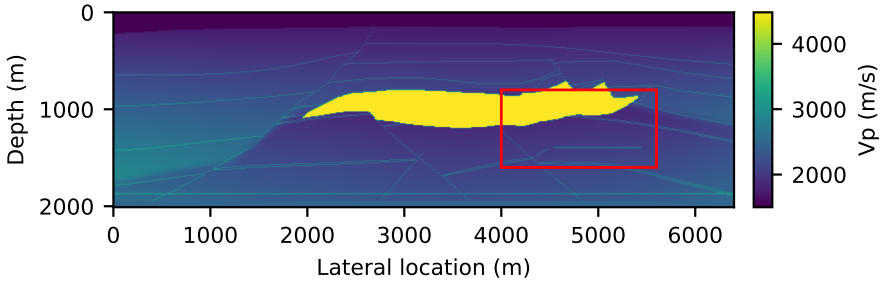

Figure 4.2: 2D section of the SEG Salt model. The red rectangle delimits the target zone.

We aim to optimize a sparse acquisition geometry with $n_d = 20$ receivers. These are initially located uniformly at the acquisition surface $z_0 = 0$ m (Figure 4.3). In the first experiment we use a uniform mask $\mathbf{\Phi}$, i.e., all the elements of the matrix have a value of 1. Therefore, no extra weight is given to any zone and the design is not target-oriented. We call the resulting geometry *optimized design* (Figure 4.4).

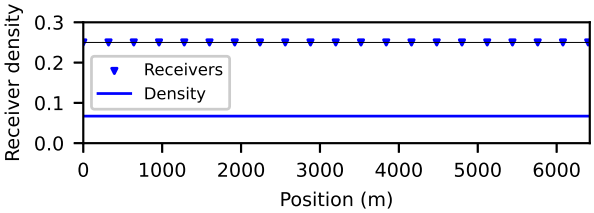

Figure 4.3: Starting geometry for the model in Figure 4.2.

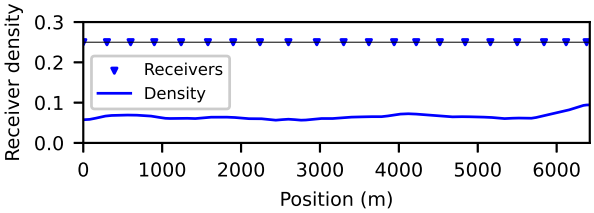

Figure 4.4: Optimized geometry for the model in Figure 4.2.

The results in Figure 4.4 show that the optimized receiver density is rather homogenous. The separation between the receivers in the corresponding receiver geometry is almost constant. Subsequently, we use an acquisition mask $\mathbf{\Phi}$ that gives more weight to the zone contained within the red box in Figure 4.2. We assume that the area under the salt dome in this section is of interest and we aim to obtain a better image of this target zone. We call the resulting geometry *target-oriented design* (Figure 4.5). It shows higher density values in the right hand side of the model, roughly above the target zone, than in the rest of the model. The corresponding receiver geometry has more receivers located at this area than at the left hand side.

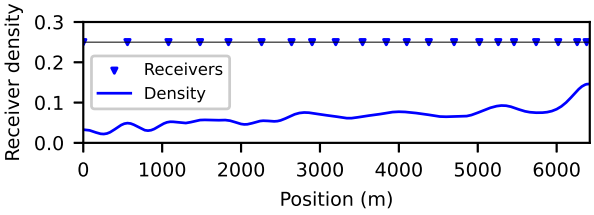

Figure 4.5: Target oriented geometry

To evaluate the effect of the optimized geometries in the image quality, we compare the images obtained with the optimized design (Figure 4.4) and the target-oriented design (Figure 4.5). The results are shown in Figures 4.6b and 4.6c, respectively. The reference image, i.e., obtained with dense spatial sampling is shown in Figure 4.6a. The image obtained with the target-oriented geometry (Figure 4.6c) shows better continuity in the region delineating the salt dome than the imaged obtained from the optimized design (Figure 4.6b). The underlying reflector is also better defined.

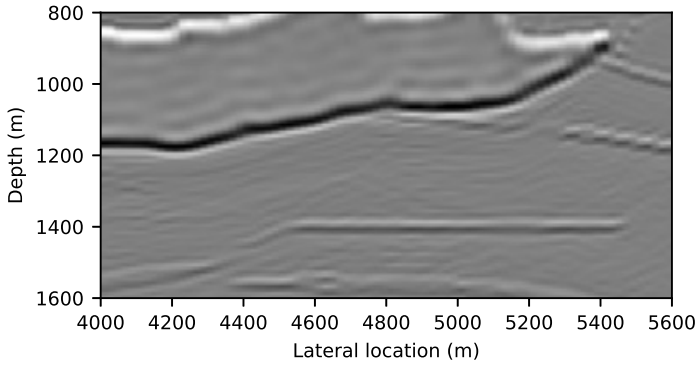

(a) Imaging with dense spatial sampling.

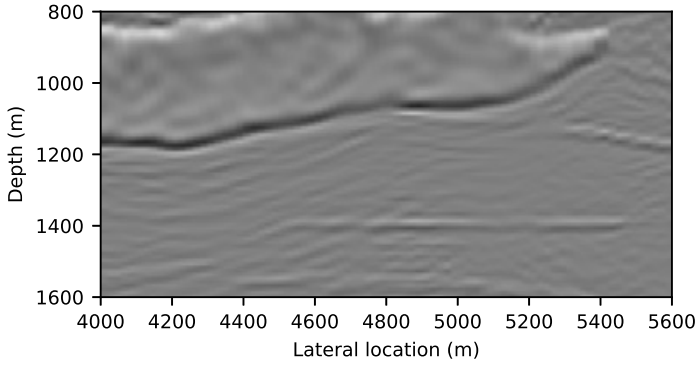

(b) Imaging with the optimized geometry.

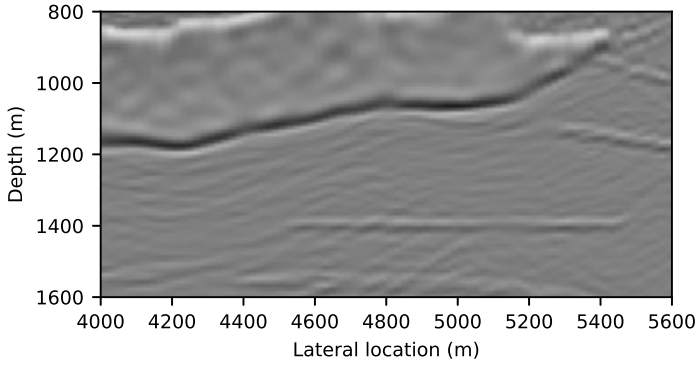

(c) Imaging with the target-oriented geometry.

Figure 4.6: Comparison of images of the target zone. (a) Reference image obtained with dense spatial sampling. (b) Image obtained with the optimized design. (c) Image obtained with the target-oriented design.

4.4.2. COMPUTING THE NUMBER OF RECEIVERS

To illustrate the procedure for computing the number of receivers described in section 4.3.6, we use the model in Figure 4.7. This model contains horizontal layers with a high-velocity perturbation embedded in the first layer.

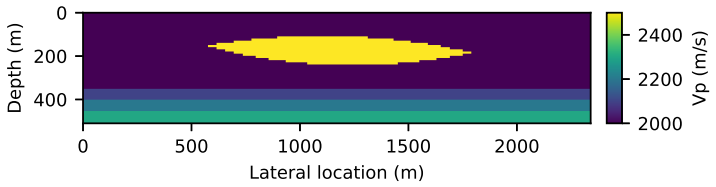

Figure 4.7: Model with high velocity perturbation.

We use our optimization algorithm to compute the optimized receiver density (Figure 4.8). The resulting function is higher in the region above the high velocity perturbation than at the edges, where the model is less complex. This indicates that more receivers are needed in this area in order to improve the image quality.

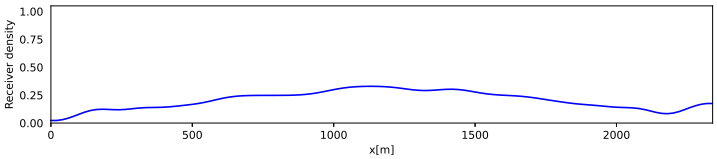

Figure 4.8: Optimized receiver density.

From the optimized receiver density we generate several receiver geometries with different number of receivers n_d. We assume that it is desired to obtain an image with a SNR of 15 dB. We add white noise to the data to simulate acquisition noise. Subsequently, we compute the images associated to the generated receiver geometries. Each one has an associated SNR after imaging. We plot the resulting SNR vs. n_d in Figure 4.9.

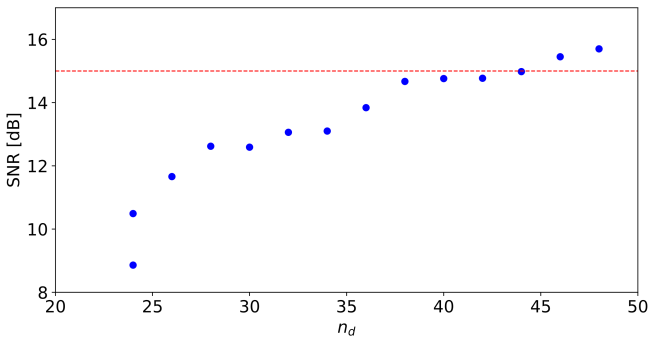

Figure 4.9: Imaging SNR vs. number of receivers. The dashed horizontal line indicates that $n_d = 44$ receivers are necessary to achieve a SNR of 15 dB.

Figure 4.9 shows that there are 2 points for $n_d = 24$ receivers. The point with lower SNR corresponds to a uniform acquisition geometry. The point with higher SNR corresponds to the image obtained when using the optimized receiver geometry. The rest of the points show how the SNR is increasing for a increasing number of receivers. The SNR obtained when doubling the number of receivers from 24 to 48 is approximately 6 dB higher, as expected. The red, horizontal line in Figure 4.9 shows that the desired SNR of 15 dB is obtained when using $n_d = 44$ receivers.

4.4.3. 3D RESULTS

We test the 3D implementation of the algorithm with the model shown in Figure 4.10. It contains a high velocity intrusion that runs along the y direction.

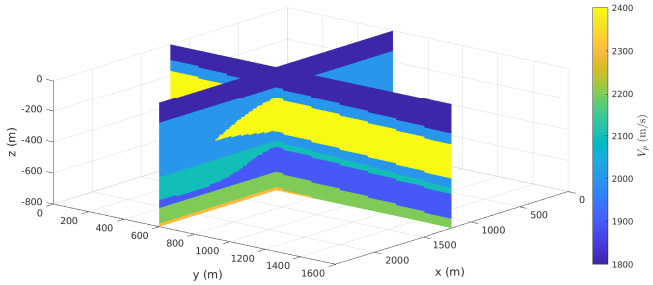

Figure 4.10: 3D model with high velocity perturbation along the $y-$ axis.

The (fixed) source geometry consists of sources located every 200 m in the x and y directions. The initial receiver geometry and density are uniform. These are shown in Figure 4.11.

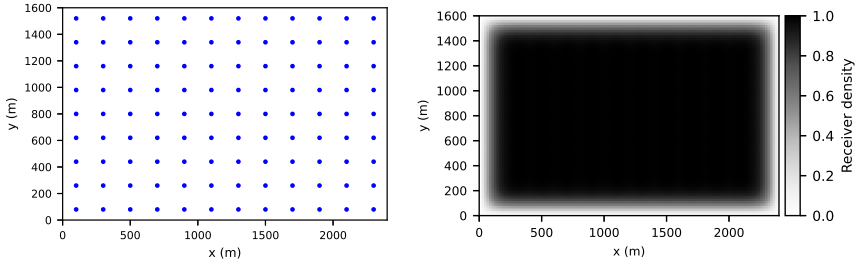

Figure 4.11: (a) Initial uniform receiver geometry and (b) receiver density for the model in Figure 4.10

In a first experiment, we run our algorithm to obtain the optimized geometry. Therefore, no extra weight is given to any area. The results are shown in Figure 4.12.

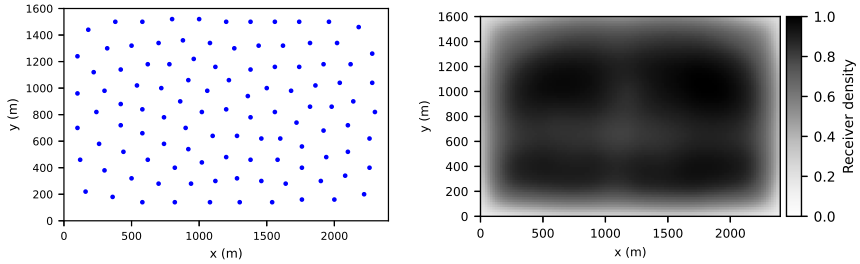

Figure 4.12: (a) Optimized receiver geometry obtained from the (b) optimized receiver density for the model in Figure 4.10.

The optimized receiver density in Figure 4.12b shows that the density is relatively somewhat higher in the zone above the high velocity intrusion that runs along the y direction. It is also higher in the lower y values. This could be due to the presence of the thin (orange) layer at the bottom that only appears for this range of y values. Otherwise, the receiver distribution is rather uniform. Subsequently, we compute the target-oriented geometry using a mask that gives more weight to a zone approximately in the middle of the model: between x ranging from 1000 m to 1500 m, y ranging from 700 m to 900 m and z ranging from 440 m to 600 m. The target-oriented design is shown in Figure 4.13.

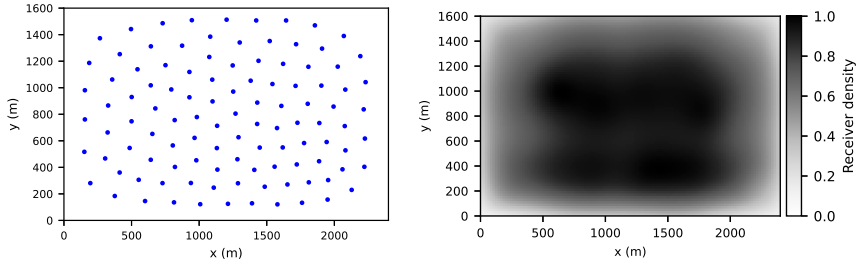

Figure 4.13: (a) Target-oriented receiver geometry obtained from the (b) target-oriented receiver density for the model in Figure 4.10.

The target-oriented receiver density is shown in Figure 4.13b. As expected it is higher in the center, i.e., roughly above the target zone, than the original receiver density in Figure 4.12b. This gives an indication that more receivers are needed in this area in order to obtain a better image quality of this zone.

Finally, we test our 3D implementation with the SEG Salt model (Figure 4.14). We create a reference model by using a densely-sampled receiver geometry, i.e., receivers every 20 m in the x and y directions. We consider a uniform, sparse source geometry with $n_s = 36$ sources. The initial receiver geometry is a uniform grid with receivers every 400 m in the x and y directions, for a total of $n_d = 17 \times 17 = 289$ receivers (Figure 4.15a).

The corresponding receiver density function is uniform (Figure 4.15b).

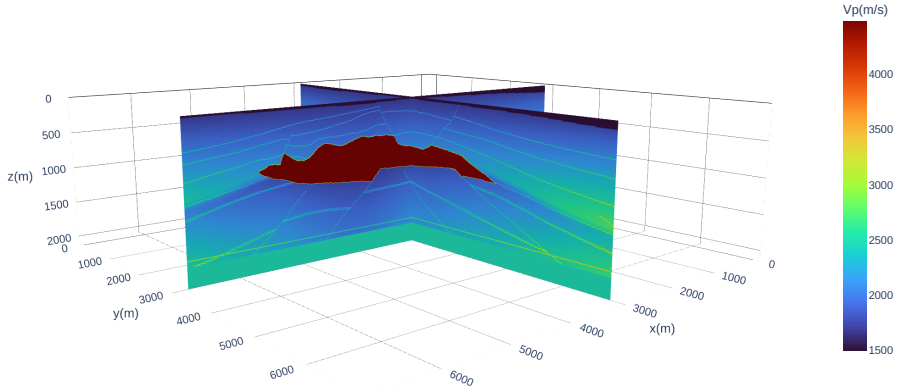

Figure 4.14: SEG Salt model.

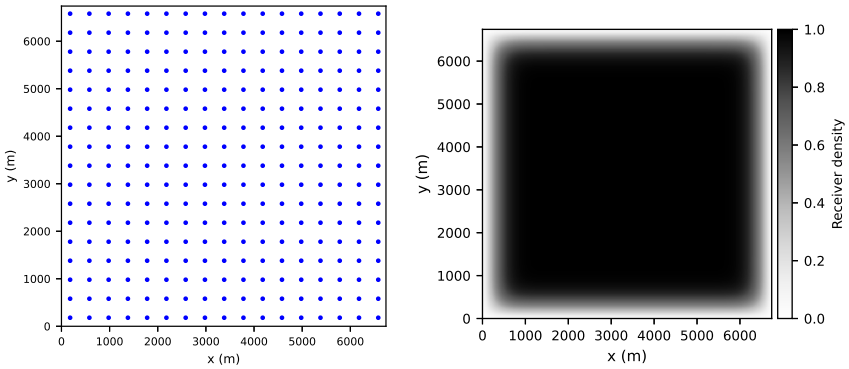

Figure 4.15: (a) Initial uniform receiver geometry and (b) receiver density for the model in Figure 4.14

Using the reference model and the initial geometry shown in Figure 4.15 we compute the optimized acquisition design (Figure 4.16). The optimized receiver density (Figure 4.16b) is higher at the center of the acquisition surface, above the top of the salt dome than at the edges, resulting in an acquisition geometry with more receivers placed at this area (Figure 4.16a). This could be due to the presence of the high velocity salt dome which is located roughly at the center of the model. Subsequently, we compute the target-oriented design, with a mask that gives more weight to the region between x ranging from 2000 m to 3000 m, y ranging from 2000 m to 3000 m and z ranging from 1000 m to 1500 m. This region corresponds to an area of possible interest beneath the salt dome. The resulting target-oriented design is shown in Figure 4.17.

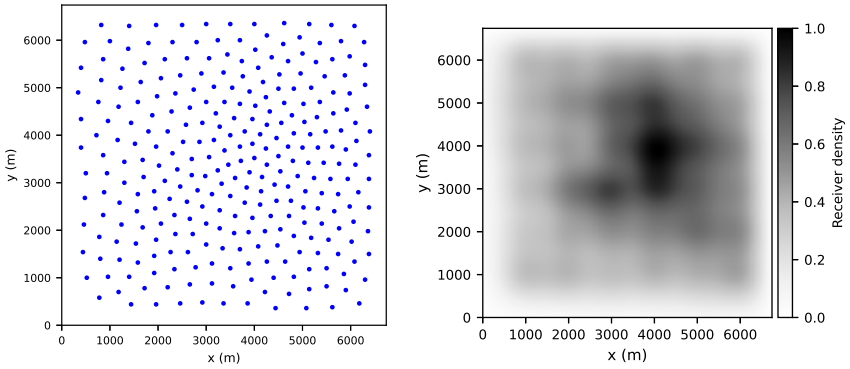

Figure 4.16: (a) Optimized receiver geometry obtained from the (b) optimized receiver density for the model in Figure 4.14.

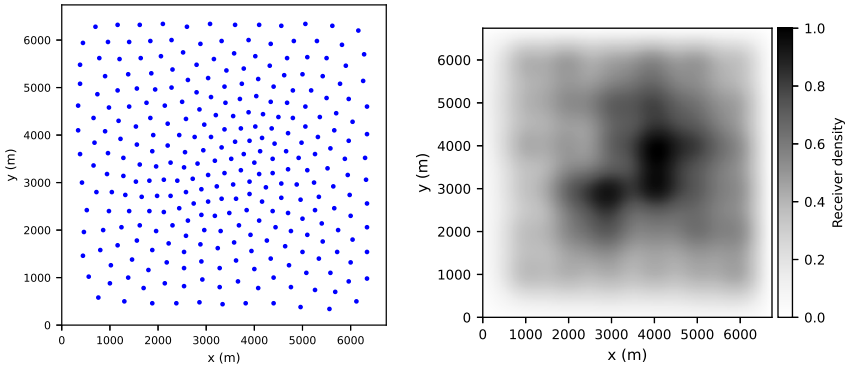

Figure 4.17: (a) Target-oriented receiver geometry obtained from the (b) target-oriented receiver density for the model in Figure 4.14.

The target-oriented geometry in Figure 4.17 clearly shows a higher density close to the area above the designated target zone (x = 2000 m to 3000 m, y = 2000 m to 3000 m) than the optimized geometry in Figure 4.16. To validate these results, we compare the images at the target zone obtained via FWM using the uniform geometry (Figure 4.15a), the optimized geometry (Figure 4.16a) and the target-oriented geometry (Figure 4.17a). The best possible scenario, i.e., the image obtained with full receiver sampling is included as a reference (Figure 4.18a). The results are plotted in Figure 4.18.

The image at the target zone obtained with the target-oriented geometry (Figure 4.18d) shows a better delineation of the salt region than the image obtained with the optimized geometry (Figure 4.18c). As expected, the improvement is larger when comparing the former with the image obtained with the uniform geometry (Figure 4.18b).

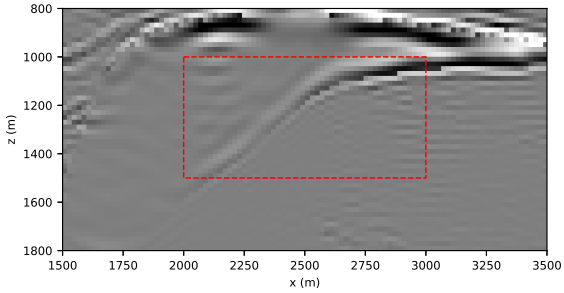

(a) Imaging using dense spatial sampling.

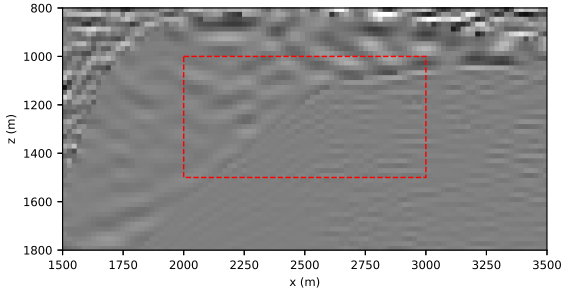

(b) Imaging with the uniform geometry in Figure 4.15a.

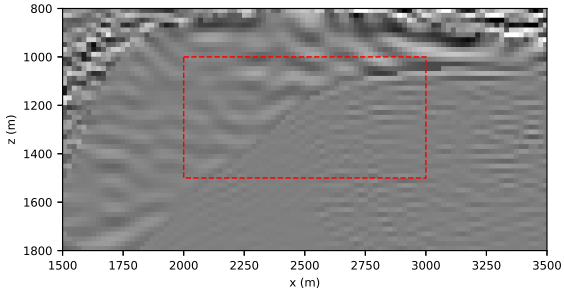

(c) Imaging with the optimized geometry in Figure 4.16a.

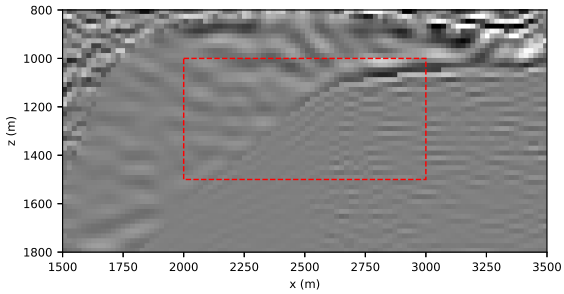

(d) Imaging with the target-oriented geometry in Figure 4.17a.

Figure 4.18: Comparison of images obtained using different acquisition geometries. Slice at $y = 2400$ m. The target zone is enclosed by the red dashed line.

The target-oriented geometry offers an improvement of 1.74 dB in the image quality with respect to the uniform geometry, while the optimized design offers an improvement of 1.15 dB with respect to the uniform geometry. This upgrade in the image quality shows that an uplift is possible even when using an sparse geometry: we used $n_d = 289$ receivers in the target-oriented design while the reference image was obtained with about 400 times more receivers.

4.5. CONCLUDING REMARKS

We proposed a new algorithm that enables the design of target-oriented acquisition geometries. Our 3D algorithm makes use of multiple reflections for imaging via FWM and enables the design of sparse acquisition geometries that improve the image quality at the target zone. The imaging results obtained when using the target-oriented design show that the image quality at the target zone is better than when using a uniform geometry. Additionally, we illustrate how the number of receivers required to obtain a certain SNR after imaging, can be computed from the optimized receiver density. In practice, based on the expected noise level during acquisition, the available hardware and financial constraints, an optimized receiver geometry that allows a target SNR could be computed. In this chapter we assumed a constant source geometry. Nevertheless, the optimization of the source geometry also plays a role in acquisition design and could be taken into account in an extension of our design algorithm. In our examples we only considered the case of white noise. However, in reality the situation is much more complex so other types of noise could be modelled in a future work to better resemble the conditions in the field.

4.A. APPENDIX A

We repeat equation 4.12 being the derivative of target function $J_{T,i}$ with respect to the receiver density $\mathbf{\Phi}$:

$$\frac{\partial J_{T,i}}{\partial \mathbf{\Phi}} = \frac{\partial}{\partial \mathbf{\Phi}} \left[\sum_n \| \mathbf{\Psi}(z_n) \Delta \mathbf{R}_i(z_n) \|_F^2 \right]. \tag{4.A.1}$$

Using the definition of the Frobenius norm we rewrite this expression as:

$$\frac{\partial J_{T,i}}{\partial \mathbf{\Phi}} = \frac{\partial}{\partial \mathbf{\Phi}} \left[\sum_n \mathrm{Tr} \left[\left(\mathbf{\Psi}(z_n) \Delta \mathbf{R}_i(z_n) \right) \left(\mathbf{\Psi}(z_n) \Delta \mathbf{R}_i(z_n) \right)^H \right] \right]. \tag{4.A.2}$$

In order to find the derivative in equation 4.A.2, it is necessary to express $\Delta \mathbf{R}_i(z_n)$ in terms of $\mathbf{\Phi}$. Following equation 3.A.8 in Appendix 3.A we find the expression:

$$\begin{aligned} \Delta \mathbf{R}_i(z_n) = \Delta \mathbf{R}_{i-1}(z_n) - \alpha_i \sum_\omega \Big[& \left[\mathbf{U}_i^-(z_0, z_n) \right]^H \mathbf{\Phi}_i(z_0) \Delta \mathbf{X}_i^-(z_0, z_0) \left[\mathbf{X}_i^+(z_n, z_0) \right]^H \\ & - \left[\mathbf{U}_i^\cup(z_0, z_n) \right]^H \mathbf{\Phi}_i(z_0) \Delta \mathbf{X}_i^-(z_0, z_0) \left[\mathbf{X}_{i-1}^-(z_n, z_0) \right]^H \Big]. \end{aligned} \tag{4.A.3}$$

Therefore, we can write the term $\mathbf{\Psi}(z_n) \Delta \mathbf{R}_i(z_n)$ as:

$$\mathbf{\Psi}(z_n) \Delta \mathbf{R}_i(z_n) = \mathbf{A}_1 \mathbf{Y} \mathbf{B}_1 - \mathbf{A}_2 \mathbf{Y} \mathbf{B}_2 + \mathbf{C}, \tag{4.A.4}$$

where:

$$\mathbf{A}_1 = -\alpha_i \boldsymbol{\Psi}(z_n) \sum_{\omega} [\mathbf{U}_i^-(z_0, z_n)]^H, \tag{4.A.5a}$$

$$\mathbf{A}_2 = -\alpha_i \boldsymbol{\Psi}(z_n) \sum_{\omega} [\mathbf{U}_i^{\cup}(z_0, z_n)]^H, \tag{4.A.5b}$$

$$\mathbf{B}_1 = \Delta\mathbf{X}_i^-(z_0, z_0)[\mathbf{X}_i^+(z_n, z_0)]^H, \tag{4.A.5c}$$

$$\mathbf{B}_2 = \Delta\mathbf{X}_i^-(z_0, z_0)[\mathbf{X}_{i-1}^-(z_n, z_0)]^H, \tag{4.A.5d}$$

$$\mathbf{C} = \boldsymbol{\Psi}(z_n)\Delta\mathbf{R}_{i-1}(z_n), \tag{4.A.5e}$$

$$\mathbf{Y} = \boldsymbol{\Phi}(z_0). \tag{4.A.5f}$$

Using this notation, we can write the derivative in equation 4.A.2 as:

$$\frac{\partial J_{T,i}}{\partial \boldsymbol{\Phi}} = \sum_n \frac{\partial}{\partial \mathbf{Y}} \mathrm{Tr}\left[(\mathbf{A}_1\mathbf{Y}\mathbf{B}_1 - \mathbf{A}_2\mathbf{Y}\mathbf{B}_2 + \mathbf{C})(\mathbf{A}_1\mathbf{Y}\mathbf{B}_1 - \mathbf{A}_2\mathbf{Y}\mathbf{B}_2 + \mathbf{C})^H\right], \tag{4.A.6}$$

which, as demonstrated in Appendix 3.A, is equal to:

$$\frac{\partial J_{T,i}}{\partial \boldsymbol{\Phi}} = 2\mathbf{A}_1^H(\mathbf{A}_1\mathbf{Y}\mathbf{B}_1 - \mathbf{A}_2\mathbf{Y}\mathbf{B}_2 + \mathbf{C})\mathbf{B}_1^H - 2\mathbf{A}_2^H(\mathbf{A}_1\mathbf{Y}\mathbf{B}_1 - \mathbf{A}_2\mathbf{Y}\mathbf{B}_2 + \mathbf{C})\mathbf{B}_2^H. \tag{4.A.7}$$

Finally, by substituting equations 4.A.5a to 4.A.5f in equation 4.A.7 we obtain:

$$\begin{aligned}\frac{\partial J_{T,i}}{\partial \boldsymbol{\Phi}} = -2\alpha_i \sum_n \sum_{\omega} \Big[&\mathbf{U}_i^-(z_0, z_n)\boldsymbol{\Psi}(z_n)\Delta\mathbf{R}_i(z_n)\mathbf{X}_i^+(z_n, z_0) \\ &- \mathbf{U}_i^{\cup}(z_0, z_n)\boldsymbol{\Psi}(z_n)\Delta\mathbf{R}_i(z_n)\mathbf{X}_{i-1}^-(z_n, z_0)\Big][\Delta\mathbf{X}_i^-(z_0, z_0)]^H.\end{aligned} \tag{4.A.8}$$

The term between braces in equation 4.A.8 is a modeled wavefield based on the weighted residual reflectivity image $\boldsymbol{\Psi}(z_n)\Delta\mathbf{R}_i(z_n)$. We define it as:

$$\begin{aligned}\Delta\mathbf{P}_r(\boldsymbol{\Psi}(z_n)\Delta\mathbf{R}_i(z_n)) = &\mathbf{U}_i^-(z_0, z_n)\boldsymbol{\Psi}(z_n)\Delta\mathbf{R}_i(z_n)\mathbf{X}_i^+(z_n, z_0) \\ &- \mathbf{U}_i^{\cup}(z_0, z_n)\boldsymbol{\Psi}(z_n)\Delta\mathbf{R}_i(z_n)\mathbf{X}_{i-1}^-(z_n, z_0).\end{aligned} \tag{4.A.9}$$

Therefore, we replace equation 4.A.9 in equation 4.A.8 and obtain:

$$\frac{\partial J_{T,i}}{\partial \boldsymbol{\Phi}} = -2\alpha_i \sum_n \sum_{\omega} \Delta\mathbf{P}_r(\boldsymbol{\Psi}(z_n)\Delta\mathbf{R}_i(z_n))[\Delta\mathbf{X}_i^-(z_0, z_0)]^H. \tag{4.A.10}$$

Equation 4.A.10 contains the correlation between the data residual $\Delta\mathbf{X}_i^-$ and the wavefield $\Delta\mathbf{P}_r$ modeled from the residual reflectivity image $\boldsymbol{\Psi}(z_n)\Delta\mathbf{R}_i$. Therefore, it can be interpreted as a mapping from the model update to the data space, at the sampling locations where more data is needed. Finally, the update direction is given by:

$$\delta\boldsymbol{\Phi}_i = -\frac{\partial J_{T,i}^*}{\partial \boldsymbol{\Phi}}. \tag{4.A.11}$$

4.B. APPENDIX B

In the gradient descent scheme, the optimal scaling parameter is found when the update direction at iteration $i+1$, is orthogonal to the direction at iteration i (Shewchuk, 1994). Therefore, the following condition must hold:

$$[\delta\Phi_{i+1}]^H \delta\Phi_i = 0, \tag{4.B.1}$$

where $\delta\Phi_i$ is a vector obtained from $\delta\Phi_i = \text{diag}\{\delta\mathbf{\Phi}_i\}$. To find the update direction $\delta\mathbf{\Phi}_{i+1}$, we use equation 4.A.10 and assume that the term $\mathbf{\Phi}$, which is implicitly contained, can be linearized.

$$\delta\mathbf{\Phi}_{i+1} = -2\alpha_i \sum_n \sum_\omega [\Delta\mathbf{P}_r(\mathbf{\Psi}(z_n)\Delta\mathbf{R}_i(z_n))]_{\mathbf{\Phi}} [\Delta\mathbf{X}_i^-(z_0,z_0)]^H. \tag{4.B.2}$$

The subscript $\mathbf{\Phi}$ in this and subsequent equations, makes reference to the variables computed for finding the optimal scaling parameter. This means, in the direction of $\delta\mathbf{\Phi}_{i+1}$. The wavefield $[\Delta\mathbf{P}_r(\mathbf{\Psi}(z_n)\Delta\mathbf{R}_i(z_n))]_{\mathbf{\Phi}}$ is therefore:

$$\begin{aligned}[\Delta\mathbf{P}_r(\mathbf{\Psi}(z_n)\Delta\mathbf{R}_i(z_n))]_{\mathbf{\Phi}} &= \mathbf{U}_i^-(z_0,z_n)[\mathbf{\Psi}(z_n)\Delta\mathbf{R}_i(z_n)]_{\mathbf{\Phi}}\mathbf{X}_i^+(z_n,z_0) \\ &+ \mathbf{U}_i^\cup(z_0,z_n)[\mathbf{\Psi}(z_n)\Delta\mathbf{R}_i(z_n)]_{\mathbf{\Phi}}\mathbf{X}_{i-1}^-(z_n,z_0),\end{aligned} \tag{4.B.3}$$

where $[\Delta\mathbf{R}_i(z_n)]_{\mathbf{\Phi}}$ is:

$$\begin{aligned}[\Delta\mathbf{R}_i(z_n)]_{\mathbf{\Phi}} &= \mathbf{\Psi}(z_n)\Delta\mathbf{R}_{i-1}(z_n) \\ &-\alpha_i\mathbf{\Psi}(z_n)\sum_\omega\Big\{\left[\mathbf{U}_i^-(z_0,z_n)\right]^H\mathbf{\Phi}_{i+1}\Delta\mathbf{X}_i^-(z_0,z_0)\left[\mathbf{X}_i^+(z_n,z_0)\right]^H \\ &+\left[\mathbf{U}_i^\cup(z_0,z_n)\right]^H\mathbf{\Phi}_{i+1}\Delta\mathbf{X}_i^-(z_0,z_0)\left[\mathbf{X}_{i-1}^-(z_n,z_0)\right]^H\Big\}.\end{aligned} \tag{4.B.4}$$

In equation 4.B.4, the receiver density $\mathbf{\Phi}_{i+1}$ is used instead of $\mathbf{\Phi}_i$. Therefore, we may substitute equation 4.11 in equation 4.B.4:

$$\begin{aligned}[\Delta\mathbf{R}_i(z_n)]_{\mathbf{\Phi}} &= \mathbf{\Psi}(z_n)\Delta\mathbf{R}_{i-1}(z_n) \\ &-\alpha_i\mathbf{\Psi}(z_n)\sum_\omega\Big\{\left[\mathbf{U}_i^-(z_0,z_n)\right]^H(\mathbf{\Phi}_i+\beta_i\delta\mathbf{\Phi}_i)\Delta\mathbf{X}_i^-(z_0,z_0)\left[\mathbf{X}_i^+(z_n,z_0)\right]^H \\ &+\left[\mathbf{U}_i^\cup(z_0,z_n)\right]^H(\mathbf{\Phi}_i+\beta_i\delta\mathbf{\Phi}_i)\Delta\mathbf{X}_i^-(z_0,z_0)\left[\mathbf{X}_{i-1}^-(z_n,z_0)\right]^H\Big\}.\end{aligned} \tag{4.B.5}$$

By substituting equation 4.B.5 in equation 4.B.3, and substituting the result in equation 4.B.2 we obtain:

$$\delta\mathbf{\Phi}_{i+1} = \delta\mathbf{\Phi}_i - 2\alpha_i\beta_i\sum_n\sum_\omega\Delta\mathbf{P}_r(\mathbf{\Psi}(z_n)\mathbf{R}_\phi(z_n))[\Delta\mathbf{X}_i^-(z_0,z_0)]^H, \tag{4.B.6}$$

where $\mathbf{R}_\phi(z_n)$ is an image obtained from:

$$\begin{aligned}\mathbf{R}_\phi(z_n) = -2\alpha_i\sum_\omega\Big\{&\left[\mathbf{U}_i^-(z_0,z_n)\right]^H\delta\mathbf{\Phi}_i\Delta\mathbf{X}_i^-(z_0,z_0)\left[\mathbf{X}_i^+(z_n,z_0)\right]^H. \\ &+\left[\mathbf{U}_i^\cup(z_0,z_n)\right]^H\delta\mathbf{\Phi}_i\Delta\mathbf{X}_i^-(z_0,z_0)\left[\mathbf{X}_{i-1}^-(z_n,z_0)\right]^H\Big\}.\end{aligned} \tag{4.B.7}$$

Finally, by substituting equation 4.B.6 in equation 4.B.1, we obtain the optimal scaling parameter:

$$\beta_i = \frac{(\delta\Phi_i)^H \delta\Phi_i}{\mathrm{diag}\left\{-2\alpha_i \sum_n \sum_\omega \Delta\mathbf{P}_r(\boldsymbol{\Psi}(z_n)\mathbf{R}_\phi(z_n))[\Delta\mathbf{X}_i^-(z_0,z_0)]^H\right\}^H \delta\Phi_i}. \tag{4.B.8}$$

From equation 4.B.8, the denominator can be computed via the following steps:

1. Compute the reflectivity image $\mathbf{R}_\phi(z_n)$
2. From this image, model seismic data $\Delta\mathbf{P}_r(\boldsymbol{\Psi}(z_n)\mathbf{R}_\phi(z_n))$
3. Correlate this data with the data residual $\Delta\mathbf{X}_i^-(z_0,z_0)$.
4. Correlate this result with the current update direction $\delta\Phi_i$.

BIBLIOGRAPHY

[1] A. J. Berkhout. *Seismic migration, imaging of acoustic energy by wave field extrapolation, A. theoretical aspects*. Elsevier, 1982.

[2] A. Berkhout. "Review Paper: An outlook on the future of seismic imaging, Part II: Full-Wavefield Migration". *Geophysical Prospecting* 62 (2014), pp. 931–949.

[3] A. Cordsen, M. Galbraith, and J. Peirce. *Planning Land 3-D Seismic Surveys*. SEG, 2000.

[4] M. Davydenko and D. Verschuur. "Full-wavefield migration: using surface and internal multiples in imaging: Full wavefield migration". *Geophysical Prospecting* 65 (2017), pp. 7–21.

[5] M. Davydenko. "Full wavefield migration: Seismic imaging using multiple scattering effects". PhD Thesis. Delft University of Technology, 2016.

[6] R. J. Greaves and T. J. Fulp. "Three-dimensional seismic monitoring of an enhanced oil recovery process". *Geophysics* 52 (1987), pp. 1175–1187.

[7] V. Krampe, P. Edme, and H. Maurer. "Optimized experimental design for seismic full waveform inversion: A computationally efficient method including a flexible implementation of acquisition costs". *Geophysical Prospecting* 69 (2021), pp. 152–166.

[8] A. Kumar, G. Blacquière, and E. Verschuur. "Extending illumination using all multiples: application to 3D acquisition geometry analysis: Extending illumination using multiples". *Geophysical Prospecting* 64 (2016), pp. 622–641.

[9] H. Maurer, A. Curtis, and D. E. Boerner. "Recent advances in optimized geophysical survey design". *Geophysics* 75 (2010), 75A177–75A194.

[10] S. Nakayama, G. Blacquière, and T. Ishiyama. "Acquisition design for direct reflectivity and velocity estimation from blended and irregularly sampled data". *Geophysical Prospecting* 67 (2019), pp. 2127–2146.

[11] F. Oghenekohwo, H. Wason, E. Esser, and F. J. Herrmann. "Low-cost time-lapse seismic with distributed compressive sensing — Part 1: Exploiting common information among the vintages". *Geophysics* 82 (2017), P1–P13.

[12] S. Qu and D. J. Verschuur. "Simultaneous joint migration inversion for high-resolution imaging/inversion of time-lapse seismic datasets". *Geophysical Prospecting* 68 (2020), pp. 1167–1188.

[13] B. Revelo-Obando and G. Blacquière. "Acquisition geometry analysis with point-spread functions". *Geophysical Prospecting* 69 (2021), pp. 1606–1624.

[14] B. Revelo-Obando and G. Blacquière. "Seismic acquisition design based on full-wavefield migration". *Geophysics* 88 (2023), P37–P49.

[15] J. R. Shewchuk. *An Introduction to the Conjugate Gradient Method Without the Agonizing Pain*. Technical Report. USA: Carnegie Mellon University, 1994.

[16] V. Singh, A. Venkataraman, R. Ho, E. Neumann, and B. Laugier. "Ocean-bottom node acquisition optimization". *SEG Technical Program Expanded Abstracts 2016*. 2016.

[17] C. Theriot, M. McDonald, M. R. Kamarudin, and P. Yu. "Survey design for optimized ocean bottom node acquisition". *SEG Technical Program Expanded Abstracts 2014*. 2014.

[18] E. J. van Veldhuizen, G Blacquière, and A. J. Berkhout. "Acquisition geometry analysis in complex 3D media". *Geophysics* 73 (2008), Q43–Q58.

[19] G. J. O. Vermeer. *3D Seismic Survey Design*. 2nd ed. Geophysical References Series. Society of Exploration Geophysicists, 2012.

[20] A. W. F. Volker, G. Blacquière, A. J. Berkhout, and L. Ongkiehong. "Comprehensive assessment of seismic acquisition geometries by focal beams—Part II: Practical aspects and examples". *Geophysics* 66 (2001), pp. 918–931.

[21] K. Wapenaar, J. Thorbecke, J. van der Neut, F. Broggini, E. Slob, and R. Snieder. "Marchenko imaging". *Geophysics* 79 (2014), WA39–WA57.

[22] V. Winner, P. Edme, and H. Maurer. "Model-based optimization of source locations for 3D acoustic seismic full-waveform inversion". *Geophysical Prospecting* 71 (2023), pp. 3–16.

[23] S Wu. "Optimising marine seismic acquisition: Source encoding in blended acquisition and target-oriented acquisition geometry optimisation". OCLC: 8630792002. PhD thesis. Delft University of Technology, 2020.

[24] S. Wu, D. J. Verschuur, and G. Blacquière. "Automated Seismic Acquisition Geometry Design for Optimized Illumination at the Target: A Linearized Approach". *IEEE Transactions on Geoscience and Remote Sensing* 60 (2022), pp. 1–13.

5

CONCLUSIONS AND RECOMMENDATIONS

5.1. INTRODUCTION

In this thesis we propose new methods for the analysis and design of acquisition geometries. We use available information of the subsurface in order to analyze the response of the combined acquisition - preprocessing - processing system. The results of the analysis show that the use of internal multiples for imaging provides additional illumination in some areas resulting in higher image resolution. When using full-wavefield Migration in the acquisition geometry optimization methods, these benefits are implicitly taken into account.

The proposed methods are suitable for monitoring purposes, because they are designed for existing subsurface models and with the aim to obtain the best possible image quality from a sparse and cheaper acquisition geometry. Many of the current methods used in the industry do not make use of this information or rely on computationally expensive wave simulations that require manual tuning of the acquisition parameters. In this chapter we discuss the main findings of this thesis.

5.2. CONCLUSIONS

In Chapter 2, we propose an analysis method for acquisition geometries based on point-spread functions. The method allows to compute a set of PSFs for a specific subsurface model and a particular sequence of data acquisition - preprocessing - processing. From these PSFs, we compute two metrics of resolution in the image domain and the corresponding illumination in the wavenumber domain. By comparing these metrics with the ideal cases, i.e., dense spatial sampling, noise-free and using the full wavefield for imaging, we showed the possible deficiencies introduced at each stage. In the processing stage, it is shown that for some subsurface models, the use of internal multiples for imaging improves the illumination and resolution in areas where the illumination by primary reflections is insufficient. Therefore, it can be concluded that by analyzing the

outcome of a seismic experiment through the use of PSFs, the acquisition geometry can be adjusted to obtain the desired resolution and illumination properties. This could potentially save costs when reducing the spatial sampling of the survey in areas where it is less needed, or by compensating the acquisition gaps with the possible additional illumination provided by the internal multiples.

In Chapter 3 we propose a novel, deterministic, acquisition geometry design algorithm. It uses perfect seismic data, obtained from available subsurface information via modeling, to create a reference reflectivity image to be used as quality criterion. This image can be seen as the best case scenario as it is obtained via imaging of perfect data. The aim of the algorithm is to optimize the receiver geometry with a reduced number of receivers that leads to the best possible imaging result. We parameterized the receiver geometry through a receiver density function that indicates the number of receivers per unit area to be placed. The density function is optimized through a gradient descent scheme. The results show that in the optimized geometries the receivers are shifted from their initial position to areas where more data is needed to image complex zones. The use of the optimized geometry allows to obtain images with better quality than those obtained from the initial, non-optimized result. This is directly observed from the images and their corresponding objective function plots.

In Chapter 4 we modify the design algorithm from chapter 3 in order to compute a target-oriented design. The objective is to obtain an optimized geometry that enables better imaging of a target zone. We achieve this by applying a mask to the model into consideration, giving a higher weight to the areas of interest than to the rest of the model. In this chapter we use a 3D implementation of our algorithm and complex 3D models. Similarly as in chapter 3, the results show that a better image quality is obtained when using the optimized geometry. Moreover, we show that the image quality of the target zone is further improved when using the target-oriented design. In this chapter we also aim to compute the number of receivers necessary to achieve a certain SNR after imaging. By introducing random noise in the reference data and using the optimized receiver density, we produce several receiver geometries with different numbers of receivers. From each geometry an image and its corresponding SNR are computed. As expected, by increasing the number of receivers the imaging SNR increases following a square-root trend. The necessary number of receivers could be inferred from the target SNR for imaging.

The results of this thesis show that the use of the available information of the subsurface could avoid limitations in the expected quality of a seismic survey. The results of chapter 2 show that this information can be used to predict the expected resolution and illumination of the survey. In chapter 3 it was demonstrated that the quality of the image obtained through the data from the optimized acquisition geometry, is higher than the quality of the image produced using a non-optimized, i.e. uniform geometry. Furthermore, in chapter 4, it was shown that the receiver geometry can be designed to favour the imaging of one or more target zones. Again, the results display an improvement on the image quality when using optimized designs.

5.3. RECOMMENDATIONS

5.3.1. NOISE

In this thesis, we used white noise to predict the number of receivers that is necessary to achieve a certain signal-to-noise ratio after imaging. However, in practice, noise is much more complex and is originated from different sources. In marine acquisition for example, swell noise and Scholte waves at the sea bottom are common sources of noise. In land acquisition, the complex structure of the near-surface generates strong scattering noise that adversely affects the signal quality. In addition wave conversion can occur, where converted waves will also be treated as noise, in case we aim for P-wave imaging. Therefore, the incorporation of these and other realistic types of noise into the acquisition geometry design algorithm remains open for future research.

5.3.2. EFFECT OF THE VELOCITY MODEL

In our experiments we used a smoothed version of the reference velocity model for imaging. In reality, velocity model building poses a complex problem which is directly affected by the choice of the acquisition geometry. Full-waveform inversion for example, requires acquisition with long offsets for the recording of low-frequency, diving waves. This requirement could be addressed in our methods in two ways. First, we could set a constraint in the receiver density function that sets high values at the edges of the acquisition surface. This would guarantee the presence of some receivers in this area, which combined with a suitable source geometry results in long acquisition offsets. The second option is to incorporate FWI as the inversion engine for velocity model building, implicitly taking its constraints into the acquisition design algorithm.

5.3.3. IMPROVING IMAGING AND USING SURFACE-RELATED MULTIPLES

In the examples presented in this thesis we use internal multiples for imaging. However, we do not use the surface-related multiples. Traditionally, the latter are removed before imaging in the marine acquisition case. Given that their amplitude is usually higher than the amplitude of the internal multiples and the fact that FWM has the capability of using them for imaging, it becomes clear that an extension of our work should include the surface-related multiples in the acquisition geometry optimization methods. As shown by Kumar et al. (2016), surface-related multiples could illuminate areas that are close to acquisition gaps that neither primary or internal multiple reflections may reach. This additional illumination will potentially improve imaging and reduce acquisition efforts.

In chapters 3 and 4 we chose FWM as the imaging method assuming the acoustic case with angle-independent reflectivity. An extension of this research could consider designing an acquisition geometry that leads to a better estimation of other parameters, such as angle-dependent reflectivity and shear-wave velocity. The latter would require the implementation of an elastic version of FWM. The use of a different inversion algorithm such as Joint Migration-Inversion could enable optimizing the acquisition geometry for better imaging and velocity model building simultaneously.

5.3.4. EXTENSION TO THE SOURCE SIDE

The optimization of the receiver geometry is only one step towards acquisition design. The source geometry also needs to be considered and could be included within the same framework, possibly by alternating between receiver and source geometry updates. In this way the overall illumination and detection properties of the survey could be improved. Moreover, the receiver and source geometries should not be considered independently. In practice acquisition geometries are often not stationary and the receiver spread may change for different shot points.

5.3.5. COST ESTIMATION

In practice, a seismic survey needs to be adapted for the characterization of the objective under consideration while being constrained by the budget available for this purpose. The total cost of the survey is not only determined by the amount and type of sources and receivers but also by the cost of the logistics and manpower required for their deployment and operation for the duration of the survey. Therefore, it is necessary to create a cost model that relates the survey quality in terms of image quality and the total cost of the survey. This could ultimately dictate the final choices for the acquisition geometry.

ACKNOWLEDGEMENTS

This thesis contains some results of my PhD research. However, it is only a part of the process towards completing my doctorate. During this journey of more than 4 years, I am very fortunate to have received the support of many people whom I would like to thank in this chapter.

First, I would like to thank my supervisor Gerrit Blacquière. Gerrit, I have enormously enjoyed from your supervision. From the moment I started my PhD you always gave me the freedom and confidence to research in the directions I found more interesting. Many ideas that shaped this thesis came out of our weekly meetings and your work together other colleagues. Apart from the academic side, you were also concerned about my wellness during the pandemic and were always open for a conversation. Thank you for dedicating a good amount of time to my supervision, even after your well deserved retirement. I hope you enjoy it and sail to many new places.

My PhD project was done within the Delphi Consortium thanks to the financial support by its sponsors. I would like to thank Eric Verschuur, the consortium's director for welcoming me to Delphi and being my promotor. Eric, I had the privilege to build upon your research and that of other Delphi Alumni. Thank you for your support as promotor through fruitful discussions, ideas and feedback. It was always a pleasure to count on your supervision and enjoy from nice dinners and carefully selected wines at the Delphi sponsor meetings and conferences.

I developed my research within the Applied Geophysics and Petrophysics (AGP) section at TU Delft. I was first welcomed to the section by Prof. Kees Wapenaar during my master studies and later for my PhD as my promotor. Dear Prof. Wapenaar, thank you for your support as promotor and feedback that allowed me to improve my thesis. I would also like to thank you for the support to the student chapter in our section through the initiatives for many academic and social events. I wish you a peaceful retirement full of new fruitful ideas.

In the AGP section, I would like to thank Prof. Evert Slob for his efforts to make the university a better place not only academically, but also more enjoyable. I would like to extend my gratitude to the staff members of the section for the valuable academic interaction and good working environment. I specially thank Jan Thorbecke for his high-performance computing courses and his kind support whenever necessary. Dear Jan, your open source material and advice were very useful in my research and a key to make a successful MPI implementation of the code used for many of the examples in this thesis.

The Delphi sponsor meetings were always a good opportunity to share my research with colleagues and sponsors. Also to share many good moments and dinners with my colleagues. Thank you Delphi colleagues: Ali, Andrea, Apostolos, Apparajitah, Auyush, Azin, Camille, Diether, Dong, Junhai, Matteo, Nick, Siddarth, Shan, Sixue, Siamak, Sverre and Tiexing, for making my time at Delphi very enjoyable. Special thanks to Leo, who was

always interested in discussing about my research and brainstorming many ideas. Jan-Willem, who assisted me in many ways at the beginning of my PhD and made my start smoother. Shotaro, your research was a great inspiration for me and I greatly appreciate the invitation for the acquisition workshop in Dubai. Gerrie, thank you for your support during the Delphi meetings and the critical beer advice. I was introduced to Delphi by the alumnus Peter Haffinger, who took some time out of his busy agenda during the EAGE 2018 annual meeting in Copenhagen to have a chat with me and talk about his company and his perspectives about the industry and academia. Thank you Peter for putting me in contact with Eric, this ultimately resulted in me joining Delphi.

My time at the university was made very enjoyable because of friends and colleagues in the AGP section. I want to specially thank to Max Holicki. Our conversations always saved me a great lot of time by finding solutions that otherwise would have taken hours to find. Chris, it has always been a pleasure to enjoy a beer together. Florencia, Johno and Aydin, who started their PhD in the same year and shared many ups and downs through the journey. Joeri, thank you for your help in many occasions and good times in the DOGS board. Thanks to my colleagues and friends Aleks, Amin, Aukje, David, Eli, Entela, Evgeniia, Faezeh, Gil, Hamed, Ilshat, Jasper, Jianhuang, Jingming, Karim, Lisanne, Mahmoud, Maria, Martha, Menno, Milad, Musab, Myrna, Nazife, Nicolas, Parvin, Quentin, Ruben, Samantha, Santosh, Sarah, Tim, Yusuke, for good times in and outside university.

Outside university, I received the support from friends and family whose support was priceless. Thank you Johannes for your friendship and always being a great support in The Netherlands. Marjanne, thank you for coming into my life and positively transforming it. Your love and support have helped me tremendously to finish my PhD. Finally, I would like to thank my brother and parents for their endless love and unconditional support. This is for you.

CURRICULUM VITÆ

Billy Alejandro REVELO OBANDO

17-02-1993 Born in Pasto, Colombia.

EDUCATION

2010–2014 BSc. Electrical Engineering
Universidad de los Andes
Bogotá, Colombia

2011–2015 BSc. Geosciences
Universidad de los Andes
Bogotá, Colombia

2016–2018 MSc. Applied Geophysics
Technische Universiteit Delft, The Netherlands
Eidgenössische Technische Hochschule (ETH) Zürich, Switzerland
Rheinisch-Westfälische Technische Hogeschool (RWTH) Aachen, Germany

2018–2024 PhD. Applied Geophysics
Technische Universiteit Delft, The Netherlands

LIST OF PUBLICATIONS

5. **B. Revelo-Obando and G. Blacquière**, *Target-oriented acquisition geometry design based on Full-Wavefield Migration*, Geophysics **89**, 3 (2024).

4. **B. Revelo-Obando and G. Blacquière**, *Seismic acquisition design based on full-wavefield migration*, Geophysics **88**, P37-P49 (2023).

3. **B. Revelo-Obando and G. Blacquière**, *Acquisition geometry design based on full-wavefield migration*, SEG Technical Program Expanded Abstracts : 6-10.

2. **B. Revelo-Obando and G. Blacquière**, *Acquisition geometry analysis with point-spread functions*, Geophysical Prospecting, Volume 69, Issue 8-9, Oct 2021, p. 1606 - 1624.

1. **B. Revelo-Obando and G. Blacquière**, *Acquisition Geometry Analysis when using Multiples for Imaging*, 82nd EAGE Annual Conference & Exhibition, Oct 2021, Volume 2021, p.1 - 5.